DISSERTATION

CAVITY RING DOWN SPECTROSCOPY: A METHOD TO MEASURE SPUTTER EROSION FOR ELECTRIC PROPULSION APPLICATIONS

Submitted by

Vijay K. Surla

Department of Mechanical Engineering

In partial fulfillment of the requirements

for the Degree of Doctor of Philosophy

Colorado State University

Fort Collins, Colorado

Spring 2007

COLORADO STATE UNIVERSITY

April 3 2007

WE HEREBY RECOMMEND THAT THE DISSERTATION PREPARED UNDER OUR SUPERVISION BY VIJAY K. SURLA ENTITLED CAVITY RING DOWN SPECTROSCOPY: A METHOD TO MEASURE SPUTTER EROSION FOR ELECTRIC PROPULSION APPLICATIONS BE ACCEPTED AS FULFILLING IN PART REQUIREMENTS FOR THE DEGREE OF DOCTOR OF PHILOSOPHY.

Committee on Graduate Work

Committee Member

Committee Member

Committee Member

Advisor

Department Head

ABSTRACT OF DISSERTATION

CAVITY RING DOWN SPECTROSCOPY: A METHOD TO MEASURE SPUTTER EROSION FOR ELECTRIC PROPULSION APPLICATIONS

Sputter erosion is a critical process in many electric propulsion (EP) devices from the point of view of both lifetime and contamination assessment. The present research develops cavity ring-down spectroscopy (CRDS) as a diagnostic tool to quantify sputter erosion. Measurements of sputtered particle number density and velocity are presented for a variety of target materials. The number density measurements are validated by comparison with a simple sputter model. The CRDS velocity measurements are obtained by a Doppler shift method and are validated by comparison with sputter simulations and Laser Induced Fluorescence (LIF) measurements. A method to obtain differential sputter yield measurements (angular information) is developed and presented. The approach is to scan the optical-axis relative to the source of sputtered particles and to use modeling to relate the resulting spatial profile to the differential sputter yield profile from the spatial profile. Demonstrative measurements are presented and validated by comparison with Quartz Crystal Microbalance (QCM) measurements.

Species-specific measurements of sputtering from multi-components material presented and show that the sputtering characteristics change relative to sputtering of pure samples. Finally, experiments investigating the excited state distributions of sputtered particle, and state-specific velocity distributions, are reported.

Vijay K. Surla
Department of Mechanical Engineering
Colorado State University
Fort Collins, Colorado 80523
Spring 2007

ACKNOWLEDGEMENTS

There are several people whom I would like to thank for their contributions. This research would not have been possible without support of the following people.

First and foremost, I would like to thank my graduate advisor Dr.Azer Yalin for his constant guidance and timely support throughout my graduate school career. I consider myself very lucky to have an advisor like him. He has always been a constant support not only to pursue my academic goals but also on a personal front. He provided me with an exciting project that greatly enriched my skills in experimental research and theoretical modeling. And I do not forget his financial support throughout. I very much appreciate the knowledge and time he shared with me throughout my graduate years at Colorado State University.

I would like to thank Dr.John Williams and Dr.Paul Wilbur for being my committee members and for their invaluable help in making me knowledgeable about the equipment used. I appreciate their time in the useful discussions I had with them. I especially thank John for allowing me to use Plasma Engineering facilities (QCM apparatus) and equipment. I also thank Dr. George Collins for having agreed to be a member of my graduate committee. I thank him for those times when I worked in his lab on slot plasma device.

I would also like to thank research group members Mark Buttweiler, Casey farnell, Kirk Zoerb, and Steen Veechi for extending their support whenever needed with my research.

I would also like to thank the fort collins chess group and its members for letting me play chess and improve my game.

On personal side, there are so many people I would like to thank for their never ending support. Firstly, I would like to thank my parents and my dearest sisters who have been a constant source of inspiration and without whose support I would not have been able to fulfil my academic aspirations. I would also like to thank my best friends Kiran, Bhasker and Pavan for their moral support as well as financial support. I also appreciate all my other friends who stood beside me in all the difficult times I have been through.

I would also like to thank all my roommates over these five years who have made my stay in fort collins a memorable one. I also thank all the members of the Fort Collins family group (Sudhir, Shanky, Sundeep, Uday kiran, Shweta, and Mohana) and my other friends in Fort Collins especially Vinod and Shilpika for their support. Last but not least, I thank Sowmya, Nithya, and Sudha for their constant support and ever lasting love.

CONTENTS

LIST OF FIGURES

LIST OF TABLES

Chapter 1

Sputtering in Electric Propulsion Systems

1.1 Introduction

This chapter provides the motivation and background for work presented in this dissertation. A brief introduction to Electric Propulsion (EP) systems and sputtering is presented. Background on Cavity Ring-Down Spectroscopy (CRDS), a laser based diagnostic which is developed to measure sputter erosion is also presented in this chapter.

1.2 Overview of Electric Propulsion

The theoretical basis for all propulsion systems stems from the conservation of total momentum applied to a spacecraft and its exhaust stream:

$$\vec{F} = m\dot{\vec{v}} = \dot{m}\vec{v_p} \tag{1.1}$$

where m is the time dependent mass of the spacecraft, $\dot{\vec{v}}$ is the acceleration vector of the spacecraft, $\vec{v_p}$ is the velocity vector of the exhaust jet relative to the spacecraft,

and $\dot{m}$ is the rate of change of spacecraft mass due to propellant mass expulsion. The term $\dot{m}\vec{v_p}$ is termed the thrust of the rocket, T, and its integral over time gives the impulse, I. When a distribution of propellant velocities are necessary to characterize a thrust plume, $\vec{v_p}$ can be characterized by an effective propellant velocity $|\vec{v_p}| = V_{eff}$. It is clear from equation 1.1 that higher exhaust velocities can create the same force for lower mass flow rates, which suggests the importance of high exhaust velocities for reducing the propellant mass for a given mission.

The amount of propellant required by the rocket engine to impart the necessary change in velocity, ΔV, to a payload is determined by the rocket or Tsiolkovski equation [1]:

$$\frac{M_i}{M_f} = \exp(\frac{\Delta V}{V_{eff}}) \tag{1.2}$$

where M_i is the initial mass of the spacecraft including fuel and M_f is the final mass of the spacecraft after the fuel has been spent. ΔV is a useful parameter to characterize the propulsion requirements for different missions. The ΔV requirement for targets such as planets are found from orbit trajectory calculations, and are influenced by the time required to reach the destination and the distance. As ΔV increases (for a fixed exhaust velocity), the amount of fuel required increases exponentially. Clearly, for missions of large ΔV, the burden of thrust generation must shift from high rates of ejection of propellant mass to high relative exhaust velocities. Unfortunately, conventional chemical rockets, whether liquid or solid, monopropellant or bipropellant, are fundamentally limited by their available combustion reaction energies and heat transfer tolerances to exhaust speeds of a few thousand meters per second. Many attractive space missions require ΔV at least an order of magnitude higher, which are conveniently generated using Electric propulsion.

Unlike chemical systems, electric propulsion systems require very little mass to accelerate a spacecraft. The propellant is ejected up to twenty times faster than from a classical thruster and therefore the overall system is many times more mass efficient. Based on their physical method of operation, EP systems are classified according to three main categories:[2]

- Electrothermal (resistojets, arcjets, etc.)

- Electrostatic (gridded ion engines, Hall-effect thrusters, field-emission thrusters, etc.)

- Electromagnetic (magnetoplasmadynamic thrusters, pulsed plasma thrusters, etc.)

Depending on the specific field of application, thrusters falling into one of these three categories can be more or less attractive, depending on their particular thrust capabilities, electrical power consumptions and other propulsion performance characteristics. The current domains of application for EP systems, are [3]:

• Geostationary Earth Orbit (GEO) telecommunications

- station-keeping

- orbit transfer

• Low Earth Orbit (LEO) telecommunications constellations

- orbit transfer

- drag compensation

- orbit and attitude control

• Interplanetary missions

• Scientific and Earth observation missions

- ultra-fine pointing

- orbit and attitude control

- drag compensation (including drag-free spacecraft)

So far, the largest commercial driver for EP application has been GEO telecommunications, where EP technology is already in operational use in Europe, Russia and in the USA. Following this lead, the use of EP for other application domains is now attracting great interest. In particular, the most important constellations of telecommunication satellites in LEO are currently being designed to use electric thrusters to perform the transfer to the operational orbit and other functions. Owing to the mass savings provided by electric propulsion, fewer launchers are needed to place the constellations in orbit, thereby allowing a major cost reduction.

The Deep Space 1 (DS1) mission has successfully validated the use of ion propulsion technology for interplanetary spacecraft. Gridded ion sources are also under consideration as a clear choice for potential near term Nuclear Electric Propulsion (NEP) missions [4]. While major advances are required to achieve these NEP missions, a critical challenge is achieving thruster lifetime. Extensive testing has been carried out on ion engines, and their development and failure modes have been reported in the literature [5]. All such failure modes could be divided into three categories depending on whether they are mainly due to accelerator grid erosion, screen grid erosion, or cathode erosion. In summary, the thruster lifetime is largely limited by sputter erosion of grids, electrodes, insulators, guard rings, and other related components. While more details of sputtering are presented in next section, briefly sputtering is the process in which an energetic bombarding particle, usually an ion accelerated by an electric field, is incident on a material and causes the ejection of atoms, ions, and/or molecules from a surface. Sputtering also plays a key role in spacecraft contamination as the sputtered particles can redeposit on other spacecraft surfaces.

1.3 Role of Sputtering in Electric Propulsion

Sputtering [6, 7] is the erosion of solid surfaces due to particle bombardment as shown in Figure 1.1. Sputtering is caused by collisions between incident bombarding particles with the atoms near the surface of the solid. The phenomenon was first observed in gas discharges in the middle of nineteenth century when cathode material from the discharge was deposited onto the glass walls of the discharge tube. Many types of massive particles (atoms, ions, neutrons etc.) can erode many types of material surfaces, though with very different efficiencies; and even lighter particles such as electrons can cause severe erosion effects on certain materials [8]. Sputtering processes are classified into three qualitative regimes [9]:

- Knock-on regime
- Linear cascade regime
- Spike regime

These regimes are distinguished by the behavior of the displaced atoms, which is a function of the energy transferred to them. while more details on these regimes are given in ref [7], the sputtering experiments of current work are mostly in the linear cascade regime. In this regime, the process can be thought of as atomic billiards, with the incident ion (cue ball) striking a large cluster of close-packed atoms (billiard balls). Lattice atoms that are displaced by the ion are called primary knock-on atoms or PKAs [9]. The PKAs displace other lattice atoms, which may in turn displace more lattice atoms, and subsequent collisions between the atoms can result in some of the atoms ejected near the surface [7].

In general, and certainly in the areas of interest of the current work, the sputtering is predominantly due to incident ions accelerated by electric fields. Erosion rates are generally characterized by the total sputtering yield Y, which is defined as the mean number of atoms removed from the surface of a solid per incident particle

(atoms/ion). The sputtering yield depends on the type of target material, the characteristics of the incident particle, and the experimental geometry (angle at which the incident particle strike the target). For the range of ion energy in thrusters, sputtering yield rapidly increases with increasing ion energy. The sputtering yield in general has its maximum value when the incident particle energy is somewhere between 5 to 50 keV [7]. At higher energies, the particle penetrates deeper into the target and fewer surface atoms are removed, lowering the sputtering yield [7]. When the ion mass equals the target mass, sputtering yield is maximized.

The current work is primarily interested in sputtering due to the significant role it plays in electric propulsion (EP) devices where the ions (propellant) parasitically sputter surfaces and components. The lifetime of state-of-the-art ion and plasma thrusters is largely limited by sputter erosion [10] and the sputtered particles can pose serious problems due to their deposition and subsequent contamination effects. For example, deposited particles can cause degradation of satellite radiators or solar panels (due to changes in surface). Figure 1.2 shows an eroded accelerator grid of NASA Solar Electric Propulsion Technology Application Readiness (NSTAR) Extended life test (ELT) thruster after several hours of operation and one can see its erosion pattern. Calculation (modeling) of the total amount of sputtering (for lifetime concerns) generally requires knowledge of the total sputter yield, Y. However, the total sputter yield does not provide information on the trajectories of the sputtered particles, which is necessary for modeling of the deposition and contamination effects. The angular trajectories are described by the differential sputter yield, y (α), i.e. the number of sputtered particles per incident ion per steradian. (Integration of the differential sputter yield over solid angle gives the total sputter yield.) In many cases differential sputter yields have not been measured, and in the absence of measurement, most numerical codes assume diffuse (cosine) sputter yields. However, such

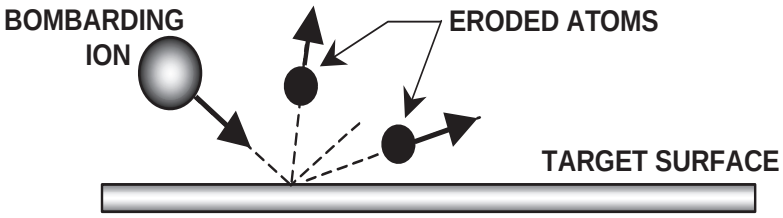

Figure 1.1: Schematic diagram of sputter erosion process. Ions bombard a target surface, and their impact causes atoms (and other particles) to be ejected due to sputtering.

an approach is ill founded since measurements show that in many cases, especially for the low ion energies relevant to EP, the actual profiles are non-diffuse in character. Knowledge of differential sputter yields is also very relevant to many technological (manufacturing) processes employing ion sputtering, such as manufacture of optical films and magnetic coatings, where trajectories of sputtered particles are also critical. In many glow discharge plasmas, sputtering contributes to electrode (cathode) erosion. Sputter erosion is also of major concern (and interest) for development of nuclear magnetic fusion [11, 12].

On the other hand, it should be noted that in certain applications sputtering is a very useful tool. For example, currently sputtering is used in applications including surface cleaning and etching, thin film deposition, and surface layer analysis, which comprises multibillion dollar industries. This dissertation focuses on the characterization of sputtering for EP applications; however, the same technique may have great use in the aforementioned areas.

In principle, both contamination and lifetime studies could be addressed by real-time tests; however, in practice, such approaches are prohibitive. Direct-duration life testing is no longer feasible for many reasons. First, the required time duration (in some cases five years or more) is long and the cost ($\sim$1M dollars per year or more) is high. Second, the long duration tests do not yield information on the causes of wear or

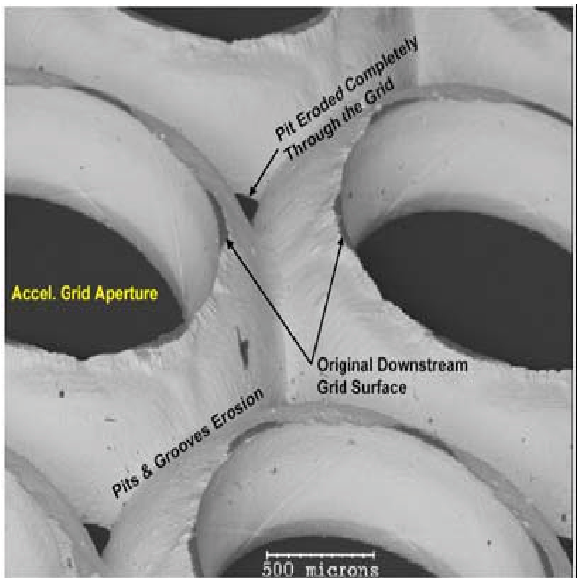

Figure 1.2: Accelerator grid from the NSTAR ELT thruster showing significant sputter erosion. In addition to limiting lifetime, the sputtered material can be re-deposited onto sensitive spacecraft surfaces causing contamination

about techniques to extend life. Further, such tests typically employ a restricted range of operating parameters, so that it is very difficult to determine how engine life depends on parameter settings. The long duration of tests required for qualification also limits the technology insertion schedule. The limitations in contamination studies are essentially analogous. Thus, in the absence of direct experimental testing, numerical modeling is typically employed to assess lifetime and contamination issues. However, such models require fundamental sputtering data, which is often not available. A list of some of the available techniques to measure sputter erosion is presented in the next section. However, due to the limitations of existing measurement techniques, there is a need for improved diagnostics both to obtain fundamental sputtering data and for insitu(real-time) studies. This is the motivation behind the present work in which result Cavity Ring-Down Spectroscopy is developed and implemented as a diagnostic to measure sputter erosion.

1.4 Existing Techniques for Sputter Measurement

There are four main categories of techniques to measure sputtering [5],[9]:

1. Changes in target mass
2. Changes in target Thickness
3. Collection of sputtered particles
4. Detection of sputtered particles in the gas phase

A variety of methods (based on the four categories) are currently used for sputtering measurements as reported in the literature [5] and a few of them are summarized here.

1.4.1 Mass Change Measurements

In principle, the most straightforward means of quantifying sputtering is to measure the amount of material removed from a target by sputtering, the ion current, and the sputtering time. The removed material generally leaves a crater in the target material. The number of ions that strike the target is simply dependent on the ion current and sputtering time.

The most common and direct way to quantify the removed material is to measure the mass change of the target due to sputtering. The approach is based on measuring the weight of the target sample before and after sputtering. While the technique is advantageous due to its directness and simplicity, it has practical disadvantages. Firstly, to obtain accurate measurement of sputter yield, large amounts of material should be removed, which is often time consuming. Another shortcoming of this approach is its inability to discriminate between the removed material and implanted ions, which can result in biased or incorrect results. Another disadvantage of the

weight loss approach is that the mass measurements generally take place outside of the vacuum [7] and thus can be error prone due to adsorbed gases and handling.

Most mass measurements are performed on torsional microbalances, which have a sensitivity on the order of 1 μg [13]. Also popularly used for such measurements is the Quartz Crystal Microbalance (QCM), a more sensitive device [7, 5]. To use a QCM, the target material must be deposited as a thin layer, on the order of a few μm thick, onto a quartz crystal. Sputter deposition is one way to coat the crystal in the target material as done in Ref.[5]. The QCM provides target mass changes due to the changes in the crystal resonant frequency.

The main advantages of the QCM mass change technique are that the QCM can detect changes in mass on the order of a few nanograms [7], and that the measurement is insitu within the vacuum chamber. A disadvantage of the QCM technique is that the target properties are restricted by the fact that the target must be thin film. Crystal orientation and surface topography may differ from bulk material. Error in the QCM technique can be introduced through the crystal frequency sensitivity to temperature variations.

The best available means to measure erosion rates is generally accepted to be the Surface Layer Activation (SLA) technique, in which some of the eroding surface is made radioactive [14]. The level of radioactivity remaining after hours of testing is monitored and thus erosion rates can directly be monitored. Approximately 50 hours of thruster time are required to obtain each successive data point. The overhead associated with pumping facilities and making the radioactivity measurements means that only one or two data points per week can be measured. While the technique is sensitive and accurate, it is time consuming to explore a range of thruster operating points. Note that this technique does not fit in any of the four categories listed and is mentioned here as appropriate.

1.4.2 Thickness Change Measurements

Thickness change measurements have also been done to characterize the crater volume and thereby measure the sputter yield. The thickness change may be measured in several ways [8]: as a change in the area density of number of atoms of the target, as a change in the geometrical thickness of the target or as a change given by total removal of a premeasured thickness of material. Optical profilometry is also used to measure the crater depth as in Ref. [15]. For area density change experiments, Rutherford Backscattering Spectrometry (RBS) is often used to detect changes in area density of a thin film target. In geometrical thickness experiments a certain area of the target is sputtered while the rest of the target is shielded by a mask. The volume of the sputtered crater is measured by a scanning electron microscope or a microstylus. Also for thin metal wires or foils thickness changes can be estimated by changes in electrical resistance. To use the geometrical thickness change technique, the target surface must be highly polished so that the sputtered depth is much larger than the surface roughness. A disadvantage with geometrical thickness measurements is that thickness changes may not necessarily be from sputtering, but from irradiation damage below the surface [7]. Another large source of error for this technique is that one dimensional depth profiles must be used to calculate a volume loss. The sputtered crater will not be perfectly symmetric or uniform. Therefore many surface profiles along different paths are taken to improve the calculation of the volume of the sputtered void. An example of thickness change sputtering experiments is those performed by Blandino et al. [16]. A 3 cm Kaufman ion source was used to sputter targets and a microstylus was used to make surface profiles measurements in order to calculate the volume of the sputtered cavity in the target. The volume left by the sputtered atoms was used to find the sputtering yield. These conventional techniques based on characterizing the crater volume using microscopic measurements of the

target crater by scanning electron microscope or field ion microscopes generally suffer from systematic errors, and are time consuming.

1.4.3 Accumulation of Sputtered Materials

It is also possible to collect the sputtered material and analyze it using surface analytical techniques. These methods are particularly useful for studying the behavior of differential sputter yield versus sputtering angle. However, it also suffers from systematic errors primarily owing to various sticking probabilities. One of these methods which is being developed at Colorado State University uses a Quartz Crystal Microbalance (QCM) [17, 18], to measure the weight of the sputtered material. In the QCM approach, the incident beam hits the target and sputtered particles in a given direction are deposited on to a QCM. The deposited target material changes the resonant frequency of the QCM's oscillator crystal. The change of resonant frequency yields the mass of deposited material, which can be mapped to get the sputter yield. However, there are several potential systematic errors with the QCM approach including differentiating the change in resonance frequency due to sputtering versus heating effects, deposition of reflected ions, and uncertainties due to sticking probabilities.

Several other choices of techniques to measure the collected material are available [9]. One method is to collect the sputtered atoms on a glass substrate and then use of optical transmission to measure the thickness of the film. Another option is to use a moveable QCM to measure differential sputtering yields in-situ at various angular locations. RBS analysis can also be used to measure the area density of the collected material on a substrate.

1.4.4 Detection of Sputtered Particles in the Gas Phase

Owing to the limitations, optical techniques are being explored to obtain absolute sputter yield measurements through detection of sputtered particles in the gas phase.

One of the methods is to use optical emission spectroscopy technique for measurement of relative sputtering yields [19, 20]. Data from these experiments must be calibrated against absolute sputtering yield measurements from other experimental categories to provide a quantitative sputtering yield value. optical spectroscopy method was used to find sputtering yields for several ion-target combinations at low energies [21]. Sputtered atoms from the target were ejected in an unexcited neutral state. The sputtered atoms became excited in the plasma and their emission spectrum signal was filtered out by a monochromator and a photomultiplier was used to measure its intensity. The intensity of the spectral line was proportional to the density of sputtered atoms and therefore also proportional to the sputtering yield. The spectral line intensity versus ion energy data was converted to a sputtering yield curve by matching the data at higher energies with absolute sputtering yield values found using a mass-loss technique. Doerner et al. [20] also used similar optical spectroscopy experiments, calibrating with mass-loss data. The main advantages of detecting sputtered atoms in the gas phase are that the optical spectroscopic techniques involved are highly sensitive and measurements can be made insitu. The disadvantage is that it is useful only to provide relative sputter yield measurements and some kind of external calibration is often required to convert relative measurements to absolute measurements.

Other methods include using a Secondary Neutral Mass Spectrometry (SNMS) technique to find sputtering yields [22]. Sputtered neutral atoms were collected by a spectrometer and a fraction of them were ionized by electron impact. A quadrapole mass filter was used to find the intensity of the detected species in the spectrum. The intensity of sputtered material was calibrated against absolute sputtering yield data obtained using an RBS technique [23] to find a value for sputtering yield.

Several research groups have performed sputter measurements using Laser Induced Florescence (LIF) [11] [12] [24] [25] [26] [27] [28] [29] [30]. LIF is a highly

sensitive diagnostic that potentially offers highly spatially resolved real time measurements. In 1992, Gaeta et. al. used LIF as an erosion rate diagnostic [31]. Several groups (for example [32], [33]) used LIF for different engineering applications like sputtering and electric propulsion. Briefly, in LIF a laser is tuned to an optical transition of the target (sputtered) species. The light excites the sputtered atoms or molecules, and the subsequent fluorescence of the excited state is detected. Ideally, a quantitative two-dimensional map of the sputtered particles is obtained. The challenge is to properly quantify LIF data to yield particle number densities. As has been thoroughly explored in combustion diagnostics, the influence of quenching, predissociation, and lineshape integrals generally makes quantitative interpretation of LIF number density data difficult. On the other hand, LIF is well suited to measure the velocity of the ejected target (sputtered) species. By scanning a laser across a known transition, the wavelength distribution of the fluorescence intensity is shifted and broadened based up on the species velocity distribution along the path of the laser. The approach has been used to measure velocities of sputtered tungsten and titanium.

Another possible optical method is to employ multi-photon ionization coupled to a time of flight mass spectrometer [34], [35], [36].

Owing to the disadvantages of existing techniques, the current work uses Cavity Ring-down Spectroscopy (CRDS) as a means to measure the concentration of sputtered particles in real time [37]. More details of the technique are presented in the following section.

1.5 Cavity Ring Down Spectrocopy

Cavity ring-down spectroscopy is a high sensitivity laser-based absorption method allowing measurement of concentrations of trace species. Detailed reviews of the technique may be found in references [38, 39]. As shown in Fig.1.3, the absorbing sample

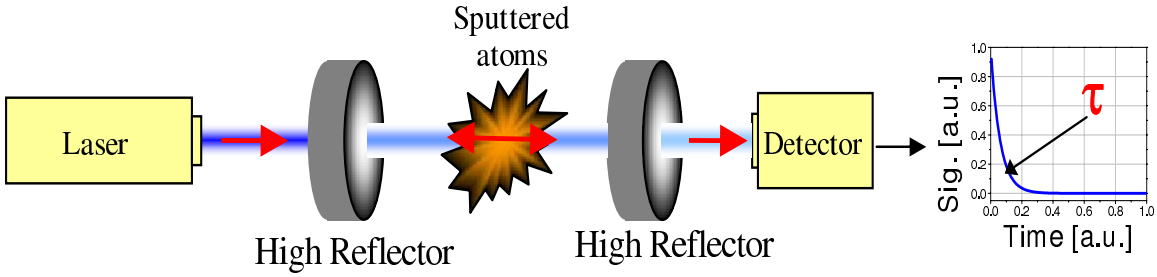

Figure 1.3: Schematic diagram of cavity ring-down spectroscopy (CRDS) setup. Laser light is coupled into a high reflectivity cavity where it bounces back and forth many times. A detector behind the cavity measures the decay of the light intensity inside the cavity, which may be related to absorber concentration.

is contained within a high-finesse optical cavity typically formed from two (or three) high-reflectivity (R) mirrors with R ∼0.9999. As the laser beam is coupled into the cavity, the light bounces back-and-forth many times within the cavity. Upon each reflection at the rear cavity-mirror, a small fraction of the cavity light leaks out to a photodetector which measures the decay of light intensity within the optical cavity. The decay is characterized by the 1/e time of decay termed the ring-down time, τ. The light decays primarily due to mirror reflective loss when there is no absorber present, and decays faster when resonant with sample absorption. The change in ring-down times can be related to the sample's absorbance (concentration). The technique provides high sensitivity owing to a combination of long effective path length and insensitivity to laser energy fluctuations.

Under appropriate conditions, the ring-down signal $S(t,\nu)$ decays (single-) exponentially versus time as [40, 41]:

$$S(t,\nu) = S_0 exp[-t/\tau(\nu)]$$
$$\frac{1}{\tau(\nu)} = \frac{c}{l}[\int k_{Eff}(x,\nu)dx + (1-R)]; k_{Eff}(\nu) = \int L(\nu^{'}-\nu)k(\nu^{'})d\nu^{'} \qquad (1.3)$$

where τ is the 1/e time of the decay (termed the ring-down time), c is the speed of light, l is the cavity length, $k_{Eff}(\nu)$ is the effective absorption coefficient, ν is the laser

frequency, 1-R is the effective mirror loss (including scattering and all cavity losses), and $L(\nu)$ is the laser lineshape function. As in conventional absorption, the effective absorption coefficient accounts for line broadening arising from the laser lineshape. In practice, the measured ring-down signal is fitted with an exponential, and the ring-down time τ is extracted. Combining τ with the "empty cavity ring-down time", τ_0 (which in practice is measured by detuning the laser) allows determination of the (effective) sample absorbance, Abs_{Eff}, and the path-integrated (effective) absorption coefficient, k_{Eff} :

$$Abs_{Eff}(\nu) = \int k_{Eff}(\nu, x)dx = \frac{l}{c}(\frac{1}{\tau(\nu)} - \frac{1}{\tau_0}) \tag{1.4}$$

As in conventional absorption, both the laser and absorber lineshapes are needed to determine the actual absorbance (and number density) if the effective absorbance is measured at a single wavelength. A more practical approach is to scan the laser frequency across the absorption line and to measure the frequency-integrated spectrum (i.e. the line area). Because the area of the effective absorbance spectrum is equivalent to the area of the (actual) absorbance spectrum, this method removes lineshape dependencies. More details are presented in subsequent chapters.

In terms of sensitivity, accuracy and measurement time, the CRDS technique has the potential to be superior to the existing measurement approaches mentioned above. In comparison to LIF, CRDS has the critical advantage of being more quantifiable, as it requires no external calibration and is unaffected by quenching interferences and lineshape overlap integrals. In comparison to the SLA technique, CRDS does not require nuclear radioactivity or modification of thruster devices and measurement times may be significantly shorter. Additionally, CRDS is a relatively simple technique to implement and is amenable to device testing. In a few cases, CRDS has been used to

measure sputtering. Using CRDS, Schwabedissen et al [42] investigated the sputtering of silicon from quartz (reference) while Booth et al [43] studied the AlF molecule in a CF_4 plasma . The number density measurements of molybdenum and titanium were earlier reported using CRDS [37] and in contrary to the past work, the technique is extended to obtain the binding energy and differential sputter yield profiles of the sputtered particles. Also, CRDS is used to obtain species specific information in multi component materials and state-specific information in complex materials.

Chapter 2

Number Density Measurements

Number density measurements of molybdenum and titanium were reported in earlier work [37] [44]. Here, the measurements are extended to study the sputtering of additional species, e.g. iron, and aluminum due to bombardment by argon ions. Briefly, an absorbance model [37] is used to identify the absorption lines, for which the experiment is configured using suitable high reflectivity mirrors at that particular wavelength. The experimental setup is described in Section 2.1 which includes the sputtering apparatus along with the CRDS set up. In Section 2.2, the detection schemes and energy level diagrams as well as characteristic spectra for each species are presented. In Section 2.3, validation measurements are presented that include comparison of the results with a sputter model. In Section 2.4, the state specific populations of sputtered particles are examined. In Section 2.5, the number density detection limits are presented and finally the work in this chapter is summarized in Section 2.6.

2.1 Experimental

The primary components of the CRDS sputter measurement system are a sputtering apparatus coupled to a CRDS optical detection system.

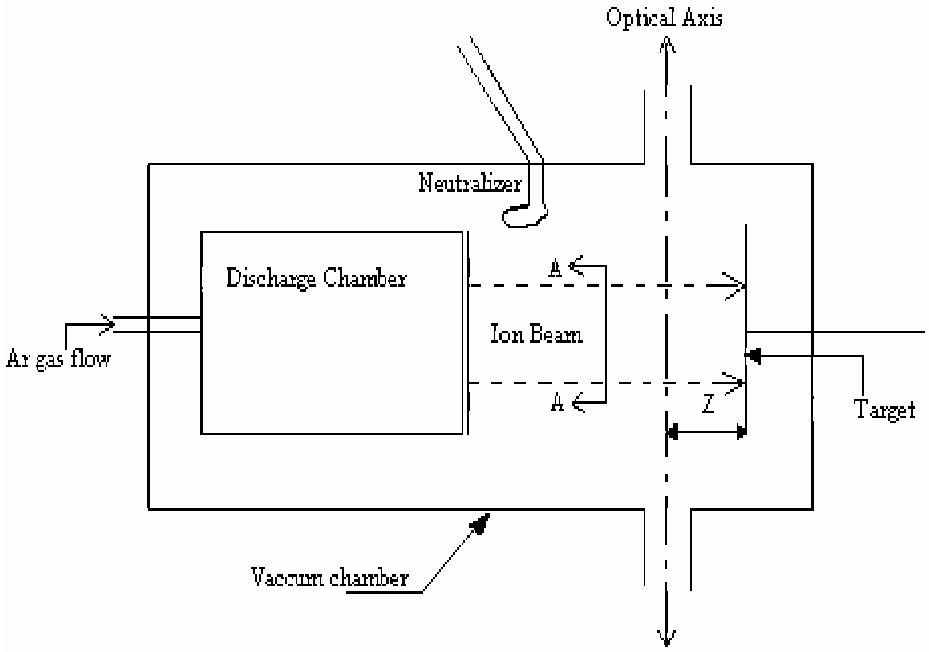

Figure 2.1: Schematic diagram of sputtering apparatus. The ion beam is incident upon target and optical axis is located Z cm upstream of the target.

2.1.1 Sputtering Apparatus

As shown in Figure 2.1, the key components of the sputtering apparatus are a gridded ion source and target, housed within a vacuum facility.

2.1.1.1 Gridded Ion source

A schematic diagram of the gridded ion source used in this work is shown in Fig. 2.2. Here, a brief explanation of the ion source is provided. When gases such as argon or xenon are introduced in to the discharge chamber, the energetic electrons from the cathode strike the atoms or molecules of the working gas with in the discharge chamber resulting in formation of ions. Some of the ions thus produced by these collisions reach various surfaces within the discharge chamber where they recombine with electrons and form neutrals; most of which are returned to the discharge chamber. Other ions will leak into a plasma sheath just upstream of the positively

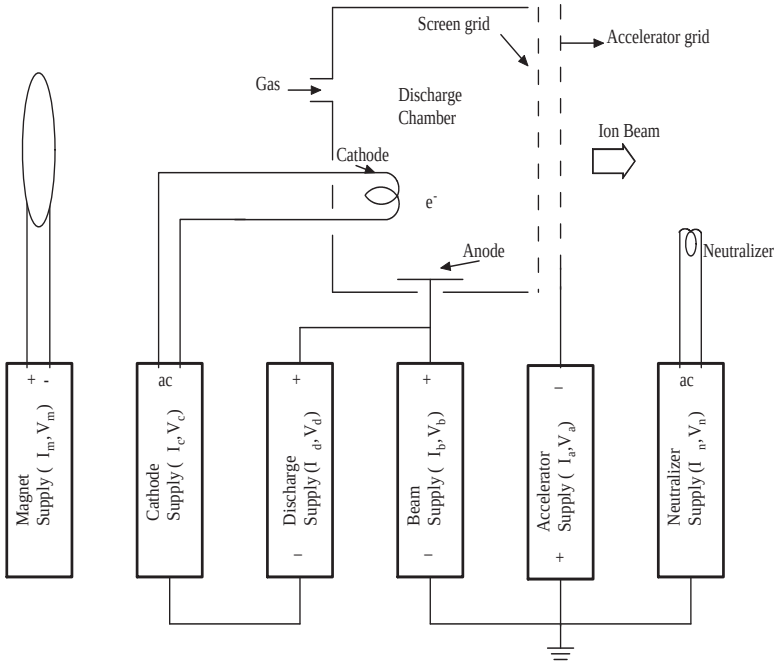

Figure 2.2: Schematic diagram of the gridded ion source with power supplies.

charged grid (screen grid). Once ions enter the sheath they are in the region of positive (screen) and negative (accelerator) grids at the exit of the chamber. The ions are electrostatically accelerated away from the positive grid and towards the negative one. The positive grid is at a much higher potential than the negative grid, thus the negative grid pulls on the positive ions. As the ions approach the negative grid they are electrostatically focused through the apertures of the negative grid and out into space at a high speed to form an ion beam. The electrons from the neutralizer cathode neutralize the ion beam resulting in a neutralized beam having equal densities of electrons and ions within the beam volume. Neutralizing is needed to prevent the ion source from gaining a net negative charge.

The energetic electrons, ions and low-energy background electrons in the discharge chamber volume constitute an electrically conductive gas, or plasma. This plasma is uniform in potential and is only several volts higher than the anode potential. The anode is therefore the electrode that most closely approximates the origin

potential for the ions. The potential of the target (being sputtered) is close to vacuum chamber ground and so the ion energy at the target corresponds to the beam supply potential, V_b. The neutralizer is also approximately at the ground potential, so that the accelerator grid must be negative of ground to prevent neutralizing electrons from flowing back in to the discharge chamber.

In the experiment, the ion beam is extracted from an 8-cm diameter structurally integrated thruster obtained from NASA [45]. It is modified to operate on an inert gas and to use refractory metal filaments for both the main and neutralizer cathodes in place of hollow cathodes used in the original design. The thruster operates with an IonTech power supply (MPS 3000), with typical beam currents and voltages of about 20-100 mA, and 400-1000 V respectively.

The pressure with in the discharge chamber is normally low enough that the mean path length between collisions for a gas atom is larger than the discharge chamber dimensions. To increase the probability of ionization by an energetic electron from the cathode before it escapes to anode, a magnetic field is placed between the cathode and anode. Although the magnetic field is designed to be effective in containing energetic electrons, the low energy background electrons can diffuse across the magnetic field relatively easily. Low energy electrons reaching the anode therefore complete the electric current between cathode and anode.

2.1.1.2 Target

The target is the material of interest to be studied. The present work reports measurements on targets including molybdenum, titanium, aluminum, iron, tantalum, dysprosium, Fe-Mn and Inconel 718 alloy. In the majority of the experiments, rectangular shaped targets are used. In each experiment, the target is mounted on a target holder as shown in Fig. 2.1. The target is affixed to two translational stages (not shown in Fig. 2.1) for movement of the sputtering target with a precision of 1

mm. One stage moves the target in the Z-direction towards or away from the ion source (and optical axis), while the second moves the target in the Y-direction which is the direction perpendicular to both the optical axis and the ion beam direction. The Y-stage is used to obtain spatial profiles for the differential sputter yield measurements at fixed Z (presented in Chapter 4). The extracted ion beam is incident upon the target thereby causing sputtering of the target material.

A roughing and turbo-pump (Turbo-V550) are used to bring the pressure to approximately 10^{-6} torr under no-flow conditions. A small argon flow (1 sccm) is used to feed the system. In order to accommodate the full optical axis of the CRDS system, two extender arms (diameter 2", length 8.25") are used to house the mirrors.

2.1.2 CRDS setup

The CRDS set-up, schematically shown in Figure 3.2, uses a broadly tunable optical parametric oscillator (OPO) laser system (doubled idler) as the light source to probe optical transitions in the 380-400 nm region (repetition rate = 10 Hz, pulse width $\sim$ 7 ns, pulse energy $\simeq$ 3 mJ, linewidth $\simeq$0.002 nm). For the present sputtering experiments, the laser linewidth is sufficiently narrow to preclude laser bandwidth complications (reference). In order to prevent possible saturation effects, the laser energy is reduced with an attenuator prior to the cavity (energies incident on the entrance mirror are $\sim 100\ \mu$J/pulse). Verification was done to ensure that experiments are in a regime where the number density measurements are unaffected by laser energy. The output from the OPO is roughly matched to the cavity using a series of irises. The cavity must be properly aligned to obtain ring-down times with maximum signal-noise ratio.

The cavity alignment procedure may be summarized as follows. Basically, the position and angles of the mirrors relative to the beam must be correctly fixed. The

center and diameter of end of the extended arm are marked on a card, which is used for cavity alignment. Using these alignment cards, the laser light is directed in such a way that it passes through the center of both arms. This can be achieved by adjusting the mirrors, M_1 and M_2 using adjustment knobs present on the mirror holders. First, the rear (downstream) reflective mirror is placed on its arm. The retro-reflected light (back reflection) from the rear high reflective mirror must be retro-reflected on top of the incident beam. This may be achieved by adjusting the three setscrews that hold each mirror tightly against the O-ring and by monitoring the position of the retro-reflection so that it is overlapped with incident beam. The second high reflective mirror is then placed on the front end (entrance) of the cavity. Its back reflection is also made to retro-reflect by adjusting the setscrews on its mount. In order to reduce the amount of sputtered material that reaches and deposits on the high-reflectivity mirrors, and to limit the exposure of the mirrors to light from plasma (which may reduce reflectivity), baffles (irises) are used in each extender arm. Each baffle has a hole of diameter about $\sim$ 10 mm that is centered on the optical axis. The ring-down signal is collected behind the output mirror with a fast photomultiplier tube, PMT (Hamamatsu R3896), which is filtered against the pump laser and other luminosity with narrow-band interference filters. The PMT signals are passed to a digitizing oscilloscope (HP54510A, 250MHz analog bandwidth, eight-bit vertical resolution) and are read to computer using custom data acquisition software (LabView) that fits the traces with exponentials in order to give the ring-down times. In order to improve signal to noise in the ring-down times, multiple traces are averaged together (typically 8 or 16 at each wavelength position). Note that the high reflectivity mirrors (typically with R 0.9998) and interference filters are chosen based on the experiment (wavelength of the absorption line).

Using the mechanical and turbo pumps, the whole setup is brought under vacuum. In vacuum, the ring-down times increase primarily due to the absence of Raleigh

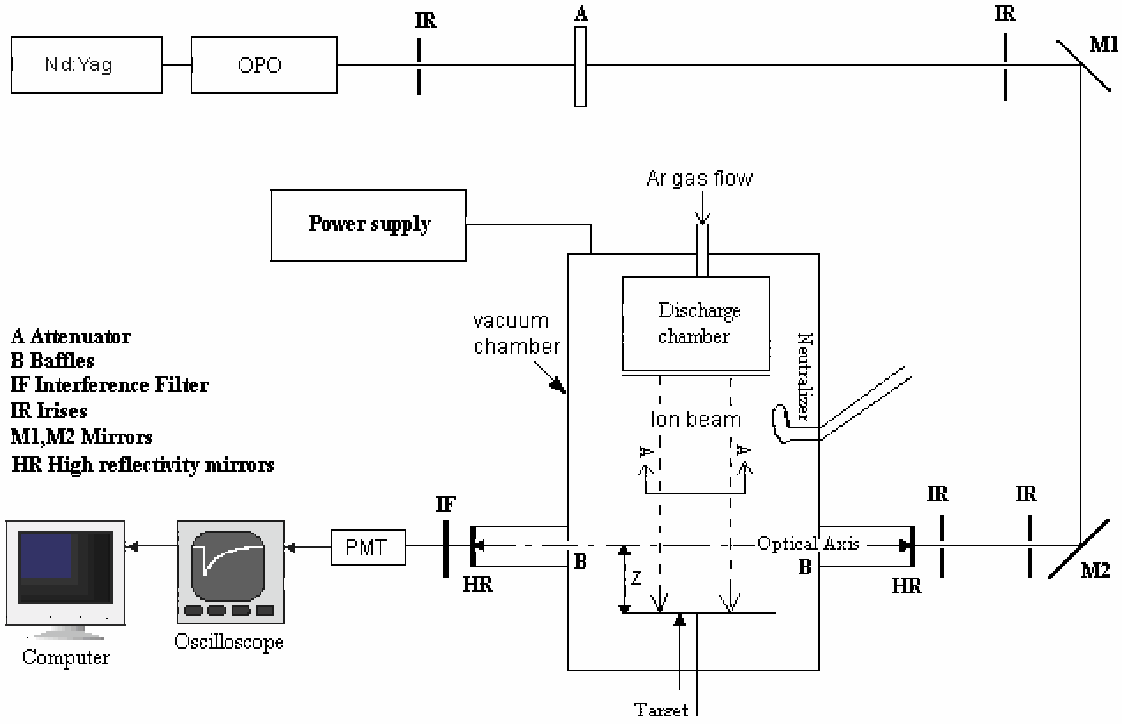

Figure 2.3: Experimental setup of the sputter measurement system.

scattering loss. After pulling vacuum, the cavity alignment is optimized by slight adjustments of the setscrews. As shown in Figure 2.3, the optical axis of the CRDS system is integrated with the chamber and positioned so that the axis is at height Z cm above the target surface (to which it is parallel) and the sputtered particles are roughly equidistant between the mirrors.

Past research shows that sputter yields from metallic species (as well as the velocities of the sputtered particles) can be effected by oxygen and other impurities (e.g. reference [12]). Because the experiments are normally operated at relatively high current densities (approximately 1 mA/cm^2), the flux of ions to the target is computed to be at least an order of magnitude higher than the flux of impurity particles, so that poisoning effects could be negligible. This conclusion is verified experimentally by

varying the chamber pressure (and impurity level) during sputtering measurements, and finding no appreciable effect on the sputtering data.

2.2 Characteristic Spectra

Each atomic species of interest is associated with a unique spectral signature composed of multiple absorption lines (electronic transitions) that can be probed to obtain the concentration. An absorbance model was developed to model the absorbance spectrum associated with each species of interest. The needed parameters (energy configurations, terms, J values, and wavelength) are taken from a NIST atomic spectra database [46]. Details on the absorbance model are presented in the earlier work [37]. Here, the model is used to identify the absorption lines that have strong optical signals while being optically accessible by the laser system and availability of HR mirrors for the experiment. For each of the species studied in this work, the spectral features are in the region of 375-400 nm. A partial energy level diagram for each species of interest is presented as appropriate in the following sections. For all energy level diagrams in this work, all energy levels below 1 eV are included, wavelengths are given as vacuum, and all parameters are from the aforementioned NIST database [46]. For all experiments reported here, sputtering is by normally incident argon ions. CRDS is an absorption technique so that in order to have a measurable signal the lower state of the transition being probed must be sufficiently populated. As will be further discussed in Section 2.4, it is generally true that the sputtered particles predominantly populate low-lying energy levels, though the assumption of a Boltzmann distribution is tenuous. The energy level spacing for the species of interest is such that a high fraction of the population is expected to be in the electronic ground state, which in some cases is split into a fine structure multiplet (e.g. iron). The absorption lines originating from the ground state (fine-structure) sub-levels are

measured using CRDS, and Equation 2.1 is used to determine the (path-integrated) number densities of the corresponding states. Generally, all levels within the mulitplet are probed and measured to find the overall multiplet population. (In the case of iron, optically accessible lines from the higher states within the multiplet are too weak, so we probe several lower levels and infer the overall multiplet population by assuming a Boltzmann distribution of the multiplet levels.) Finally, a small correction (by assuming that all the energy states for the species follow the Boltzmann distribution) is made to convert the ground state multiplet number density to the overall species number density. As will be further discussed, greater than 95-99 % of the overall population typically resides in the ground state multiplet, so that this final correction is small (<5 %).

The measured CRDS absorbance spectrum results in a lineshape, i.e. dependence of absorbance on wavelength. More general discussion of CRDS lineshapes is reported in earlier work [37] and here a general comment is made on the measured lineshapes which is applicable to all species and spectra presented in this work. The gas within the sputtering chamber is at low pressure ($\sim 10^{-5} - 10^{-6}$ torr) with Knudsen number $<< 1$. Therefore, the gas is in a free molecular (collisionless) flow regime. Thus, velocities of the sputtered particles do not follow a Maxwell-Boltzmann distribution. Velocity profiles of sputtered particles have been studied extensively, and it has been found that they follow Thompson distributions (see Chapter 3). At these conditions the absorption lineshape is predominantly determined by Doppler shifts due to the thompson distribution, though not corresponding to the standard Gaussian expression (which assumes a Maxwell-Boltzmann velocity distribution). More details on the lineshape are presented in Chapter 3, and here the focus is on obtaining the number densities of sputtered particles. Assuming the absorption line parameters are known, the measured area $\int Abs_{Eff}(\nu)d\nu$ of a transition from lower state i to upper state k

can be readily converted to the path-integrated concentration of the lower state n_i as:

$$\int n_i dx = 8\pi \frac{g_i}{g_k} \frac{{\nu_{ki}}^2}{A_{ki} c^2} (\int Abs_{Eff}(\nu) d\nu) \tag{2.1}$$

where g_i,g_k are the level degeneracies, ν is the transition frequency, and A_{ki} is the transition Einstein A coefficient. Note that n_i is not the total path-integrated concentration rather it is the path-integrated concentrartion of level E_i. Therefore, to obtain total path-integrated concentration, one has to probe all the energy levels within the ground state multiplet (and then apply the correction described earlier). Actual concentration can be determined from the path-integrated concentration by assuming a uniform concentration profile over a known column length (l_{abs}) as reported in reference [37], or by using modeled spatial profile shapes.

2.2.1 Iron

Figure 2.4 shows a partial energy level diagram for iron. The electronic ground state multiplet $3d^6 4s^2\ ^5D$ is split into five levels (J=4, 3, .., 0). Figure 2.5 shows a representative absorbance spectrum measured by CRDS including four spectral lines. The absorption lines measured in the spectrum are shown with broken lines in the energy level diagram. The conditions for the argon ion beam are: a beam current of 20 mA and beam voltage of 750 V. For all absorbance spectra given in this work, the points are experimental measurements while the solid line is a series (sum) of Voigt profiles fitted to the peaks (with a single Voigt used for each absorption feature). In practice, the Peakfit software is used to fit the Voigt profiles for the experimental data so as to calculate the area under the absorbance spectrum and other parameters related to the peak. The measured lines in the absorbance spectrum originate from the three lowest energy levels (J=4, 3, 2), and the fitted Voigt areas may be used to

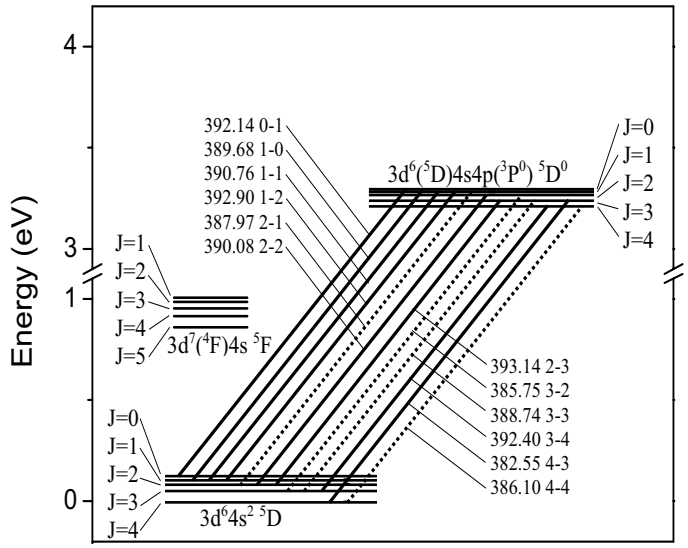

Figure 2.4: Partial energy level diagram for iron.

determine the path-integrated number densities of these levels (Equation 2.1). The characterization of excitation temperature (Section 2.4) suggests that >93 percent of the overall iron population is in these measured states (and greater than 99 percent of the iron is in the ground state multiplet). Therefore, scaling the (sum of the) population of the three measured states to infer the overall iron population can be done with relatively high fidelity. For the conditions of the displayed spectrum, a path-integrated number density of iron atoms of $2.3 \pm 0.2 \times 10^{10}$ cm^{-2} is obtained. Comparison with the sputter model is presented in Section 2.3. The uncertainty is due to uncertainty in the Voigt fitted areas, population fractions, and Einstein A coefficients.

2.2.2 Aluminum

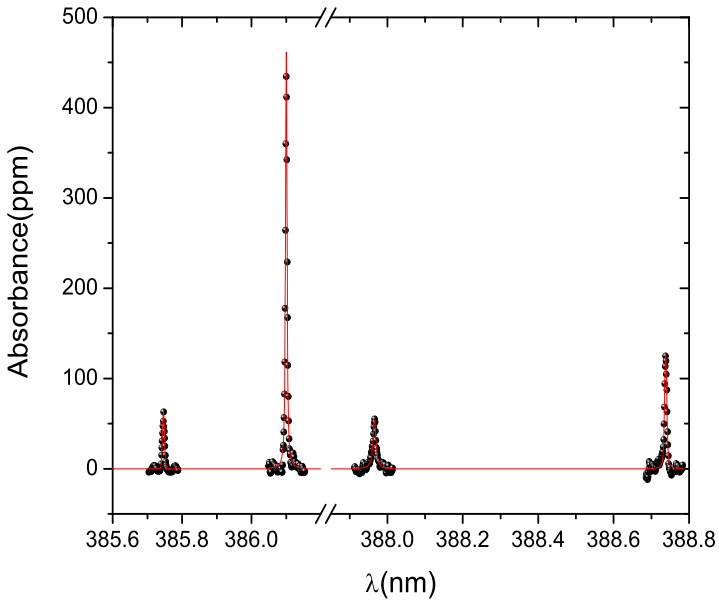

Figure 2.5: Iron absorbance spectrum recorded by CRDS.

Figure 2.6 shows a partial energy level diagram for aluminum, while Figure 2.7 shows a CRDS absorbance spectrum (argon beam voltage of 750 V and beam current of 18 mA). For aluminum, the ground state multiplet has two fine structure levels (J=1/2, 3/2), and the absorbance spectrum is based on probing one line from each state. The next lowest energy level is above 1 eV and our Boltzmann analysis (section 2.3) suggests that greater than 99 % of the population is in the measured ground state multiplet. Thus, the areas of the two lines can be used to determine the overall Al population. For these conditions, a path-integrated number density $6.8 \pm 0.6 \times 10^9$ cm^{-2} is found (comparison with model is given in Section 2.3).

2.2.3 Titanium

Detection of sputtered titanium from the electronic ground state multiplet $3d^2 4s^2$ ^3F was previously reported [37]. The three lines previously measured were at 395.98,

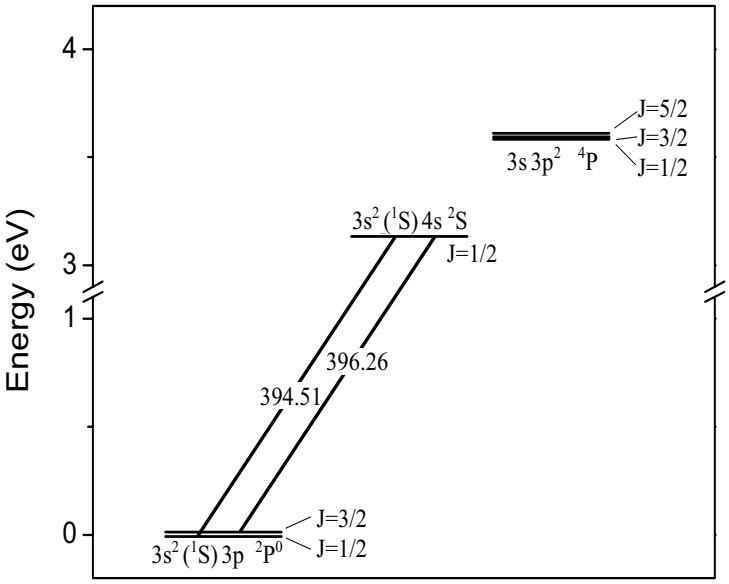

Figure 2.6: Partial energy level diagram for aluminum.

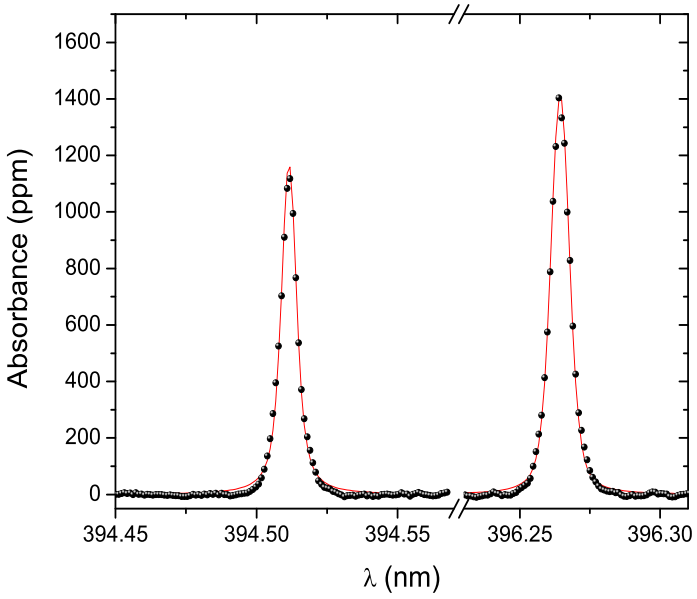

Figure 2.7: Aluminum absorbance spectrum recorded by CRDS.

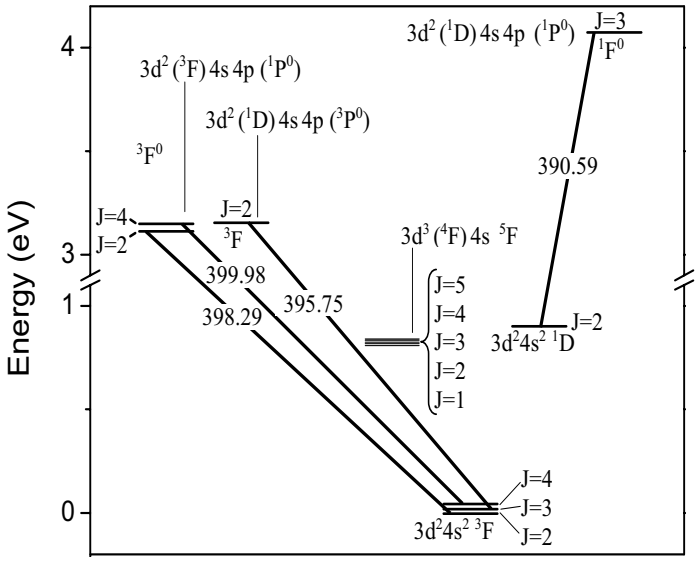

Figure 2.8: Partial energy level diagram for titanium.

395.75, 395.93 nm (originating from the multiplet sub-levels J=2, 3, 4 respectively). Here, results from different lines at 398.29, 399.98, and 395.75 nm (originating from J=2, 3, 4 respectively) are presented. This newer selection of lines is preferable for quantitative detection owing to the lower uncertainty in their Einstein A coefficients.

The (new) set of lines are shown in Figure 2.8, while Figure 2.9 shows a representative CRD spectrum of 2 of the lines (argon beam voltage of 750 V and beam current of 18 mA). Again, at these conditions, a large fraction of the overall titanium population is assumed to be in the ground state multiplet. This assumption is based on taking a Boltzmann distribution of states, with characteristic temperature found from the measured lines, see Section 2.4. In this way, the ground state multiplet population must be multiplied by 1.02 to find the overall species population. (The correction is less than our experimental uncertainty.) In order to verify that the populations of higher energy levels are minimal, an attempt was made to measure the

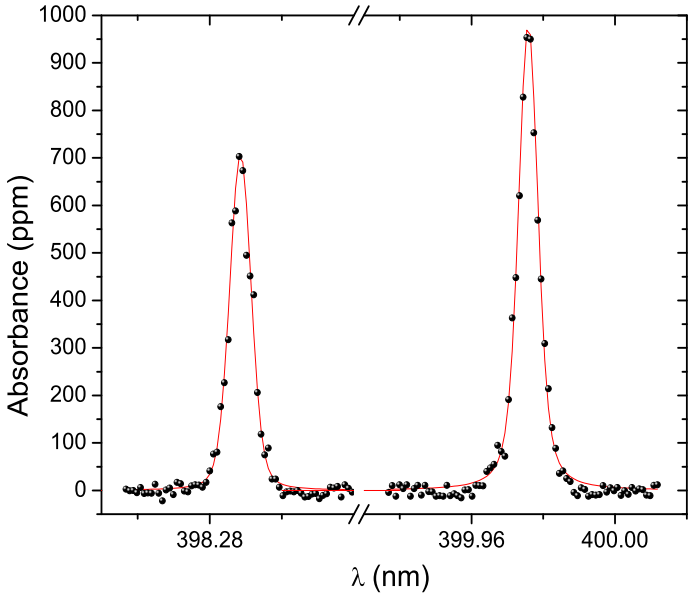

Figure 2.9: Titanium absorbance spectrum recorded by CRDS.

absorption line at 390.59 nm (see Fig. 2.8). This transition has a comparable Einstein A coefficient, yet it is undetectable for our signal to noise levels. This confirms the assumption that only the ground state multiplet has significant population. For the conditions of the displayed spectrum, the path-integrated number density of titanium atoms is found to be $5.1 \pm 0.5 \times 10^9\ cm^{-2}$. Comparison with the sputter model are presented in Section 2.3

2.2.4 Molybdenum

The molybdenum ground state has no fine structure, and the CRDS detection scheme is based on probing lines (379.93 nm and 386.52 nm) originating from the (same) ground state energy level. Spectra and a partial energy level diagram for molybdenum may be found in earlier work [37] but is included in the next section on validation.

2.3 Measurement Validation

Several validations of the CRDS measurements have been performed. First, measurements of the number density as a function of beam current have been performed. Figure 2.10 shows a plot of variation of number density versus beam current for all the four species. In the plot, a uniform number density over a path length of 8 cm is assumed in order to convert the measured path-integrated number density into an average value of number density, though really it is the shape of the dependence that is of interest here. As the beam current is varied (at constant ion energy) the sputter yields are not altered; however, the current density increases. Thus, as expected, one observes a linear dependence (through the origin) of sputtered particle number density on beam current. The same expected linear behavior is found for all the species studied.

While the beam current variation data is useful for trend validation it does not provide absolute validation. As another means of validation a simple sputter model was developed to numerically predict path-integrated number densities as a function of experimental conditions. More details about the sputter model are presented in past work [37] and here it is only summarized. The sputtering model uses the following to calculate the path-integrated concentrations of sputtered particles:

- Experimental current density profile (see Chapter 4)
- CRDS measured velocity distributions (see Chapter 3)
- Differential sputter yield profiles

  -measured profiles(see Chapter 4) or

  -assumes a cosine distribution for the non-measured profiles
- Total sputter yields taken from the literature [47]
- Target/optical-axis geometry

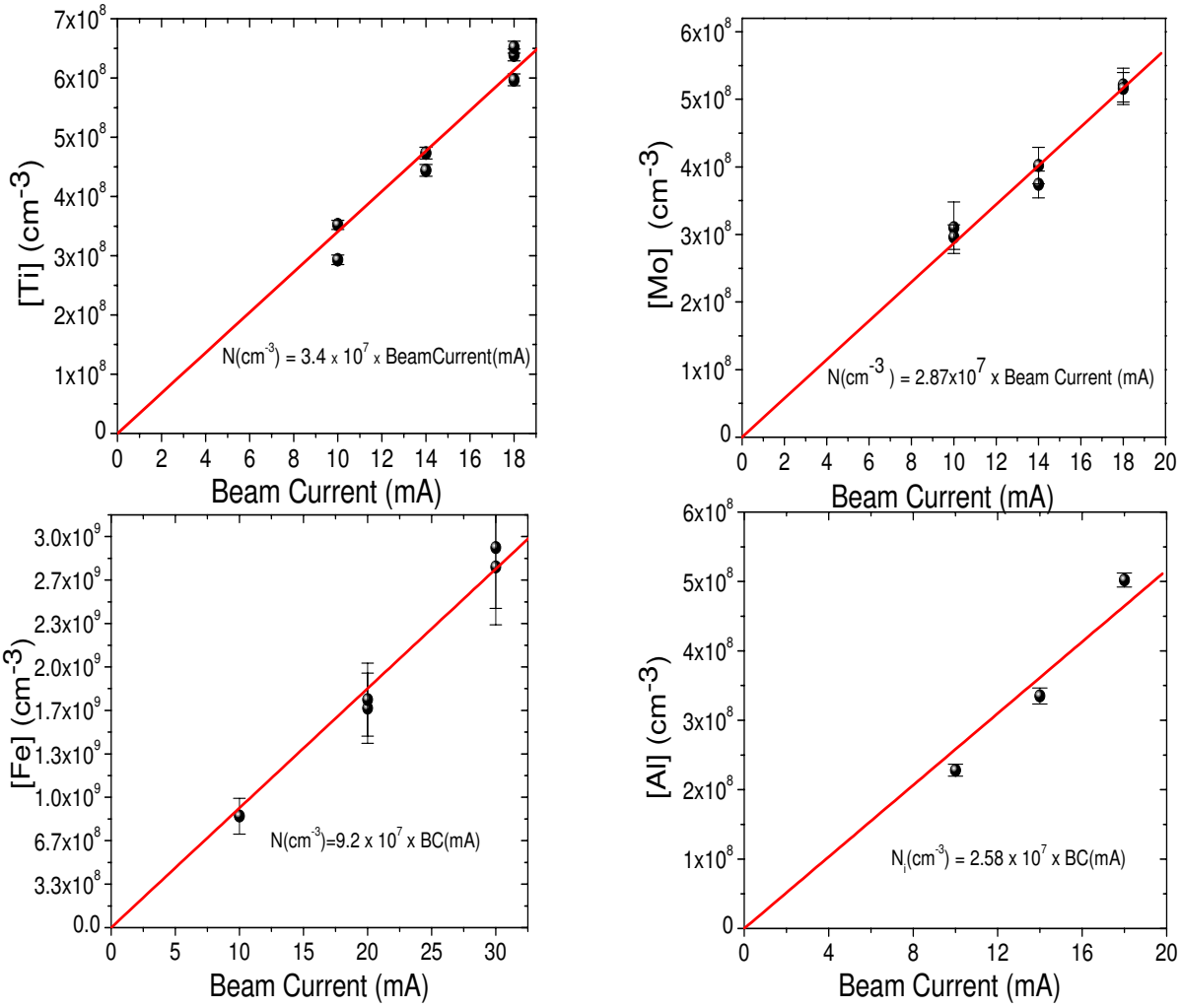

Figure 2.10: Dependence of number density on beam current.

The model uses a finite element approach for both the target and optical axis, and computes the contribution of sputtered particles from each target element to each element along the optical axis. Summing the number densities along the extent of the optical axis then yields the path-integrated number density. The results are insensitive to the grid size. For 750 eV ions, the current work uses a total sputter yield of 0.7 ± 0.2 for titanium, 0.9 ± 0.3 for molybdenum, 1.1 ± 0.1 for aluminum, and 1.1 ± 0.1 for iron [47]. The current work implicitly assumes that the velocity distributions apply to all energy levels probed, an assumption verified with CRDS measurements in Chapter 3 and also consistent with LIF measurements of velocity fields (see Reference [48]). For beam currents of 18 mA (20 mA for Fe), the path-integrated number densities found from the sputter code as well as from the CRDS are given in Table 2.1.

Table 2.1: Comparison of path-integrated number densities found from CRDS and sputter model

Line density by:	Ti	Mo	Fe	Al
CRDS (cm^{-2})	$5.1\pm\ 0.5 \times 10^9$	$4.1\pm\ 0.4 \times 10^9$	$1.4\pm\ 0.2 \times 10^{10}$	$7.2\pm\ 0.7 \times 10^9$
Model (cm^{-2})	$4.8\pm\ 0.9 \times 10^9$	$4.2\pm\ 1.2 \times 10^9$	$1.4\pm\ 1.0 \times 10^{10}$	$7.4\pm\ 1.2 \times 10^9$

For titanium, molybdenum, iron, and aluminum, there is favorable agreement (within error bars) between the model and experiment. The slight discrepancy could be due to the assumption on the differential sputter yield profiles or an incorrect value of sputter yield taken from the literature. Note that there is lot of disagreement in the reported values of sputter yields (found in the literature) that might introduce an error in the modeled values. Later, in Chapter 4, the sputter model is used in a way that the total sputter yield (Y), V_b and n (for velocity distribution), and 'a' (for differential sputter yield profiles) are set as free parameters. The model then uses a least squared analysis routine to find the aforementioned parameters(Y,V_b,n,a). This

is done by best fitting the measured path-integrated concentration with a series of modeled path-integrated concentrations. The agreement between the experimental and modeled results in Table 2.1 is considered as a validation of the CRDS results.

A general comment is made here on the effect of isotopes on the current measurements. Aluminium has a single naturally occurring isotope (^{27}Al), while iron has three isotopes (91.7% ^{56}Fe, 5.8% ^{54}Fe, and 2.1% ^{56}Fe), titanium has five isotopes (73.7% ^{48}Ti, 8.2% ^{46}Ti, 7.4% ^{47}Ti, 5.4% ^{49}Ti,and 5.1% ^{50}Ti) and molybdenum has seven isotopes (24.1% ^{98}Mo, 16.6% ^{96}Mo,14.8% ^{92}Mo, 15.9% ^{95}Mo, 9.6% ^{100}Mo, 9.5% ^{97}Mo, and 9.25% ^{94}Mo). Typical isotope shifts are ¡0.01-0.1 nm and therefore do not cause separate peaks, but rather may broaden measured peaks. Although, such effects should be further investigated, they have not been experimentally observed and are not believed to effect the present measurements. (Because the line area is used and all isotopes fall into a single peak in the current measurements, their contributions are all accounted for). Considerations for hyperfine structure are analogous.

2.4 Population Distributions

The energy level populations of sputtered particles are both of theoretical interest (to model and understand the physical sputtering process) and of practical interest (to enable the conversion of measured populations from a subset of energy levels to the overall species population). A number of LIF experiments have examined these populations for a variety of target species and ions (references 6,26,28 and references therein). These LIF studies generally found that although there is little physical basis to consider the sputtered particles as being in thermodynamic equilibrium, the populations of the sub-levels of a given multiplet can generally be described with a single Boltzmann temperature (at least as a means of characterization). It was found that these Boltzmann temperatures were typically in the range 300-2000 K, and

that the distributions within different mutliplets (of the same species and sputtered at the same conditions) tend to follow different Boltzmann temperatures [24] [48]. Further, past data suggests that for a given multiplet, the Boltzmann temperature varies only weakly with ion energy and ion mass [11] [25][26]. However, such studies require quantitative determination of (at least relative) level populations, and for the reasons provided previously, LIF is often not well suited for such analyses (see, e.g, the uncertainties of Table IV of reference [11]). (On the other hand, LIF has provided very precise results on the velocity profiles of ejected particles; for example, demonstrating that the velocity profiles from different sub-levels of the ground state show no variation with one another [48]. More details of this work (and related ideas) are presented in Chapter 6 and here the focus is only on the distribution of sputtered particles within the ground state multiplet.

The more directly quantitative nature of CRDS makes it amenable to studying the populations of different sub-levels of sputtered particles. For several species, the populations of the fine structure sub-levels of the electronic ground state multiplet are examined. As a means to describe the measured populations within the multiplet, the notion of a Boltzmann temperature is used as a means to characterize the data. For titanium, the populations of the three ground state fine structure levels ($3d^2 4s^2$ ^3F : J=2, 0 eV; J=3, 0.021 eV; J=4, 0.048 eV) are considered; for aluminum, the populations of the two ground state fine structure levels ($3s^2(1S)$ ^3p $^2P^0$: J=1/2, 0 eV; J=3/2, 0.0139 eV) are considered; and for iron, only the fine structure levels ($3d^6 4s^2$ a ^5D : J=4, 0 eV; J=3, 0.0516 eV) are considered as signals from the higher levels J=2,1,0 have poor signal to noise (especially at low beam energies where the sputter yield is reduced). Molybdenum is not studied as it has no fine structure. As a means of illustration, Fig. 2.11 shows a Boltzmann plot for titanium (beam current of 30 mA, beam voltage of 450 eV) which yields a Boltzmann temperature of 1250 $\pm$

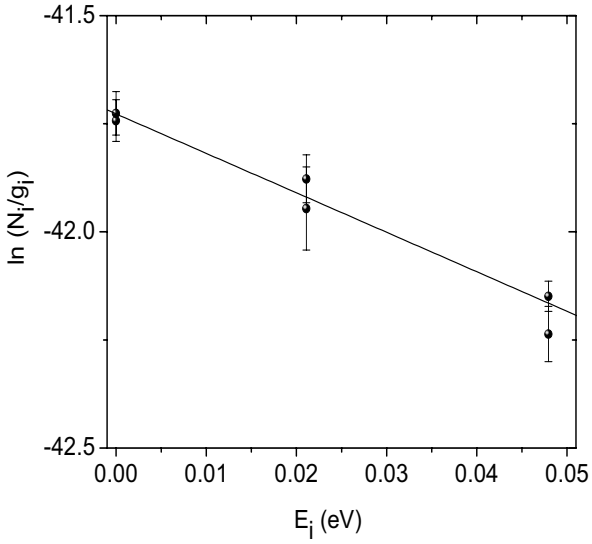

Figure 2.11: Boltzmann Analysis of sputtered titanium.

120 K. The Boltzmann fit uses the uncertainties of the individual data points which are due to uncertainties in fitted absorption areas and Einstein A coefficients.

For the three species studied, the dependence of Boltzmann temperature (of the energy levels specified above) on both beam current and beam energy (voltage) is studied. Within our error bars the dependence on beam current is negligible (implying that the sputtering at an individual site is independent of the number of ions in the beam). Figure 2.12 shows the dependence of Boltzmann temperature on argon ion energy for titanium, aluminum, and iron. Error bars are from the Boltzmann fits and data repeatability. To our knowledge, these are the first CRDS studies of this type. The inferred Boltzmann temperatures are relatively consistent with those from past LIF studies (which have reported in the range 300-2000 K for a range of metal targets and ions). For aluminum the Boltzmann temperatures are relatively constant, while for titanium and iron there is a weak increase with ion energy. Such trends have not been detected in earlier LIF studies, however those studies looked at different species

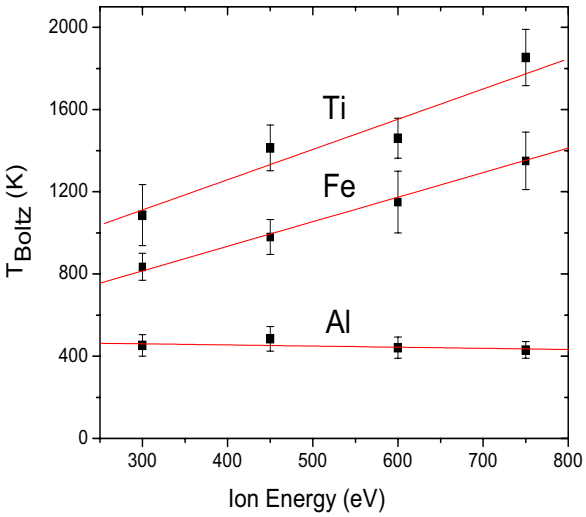

Figure 2.12: Dependence of Boltzmann temperature on ion energy.Linear fits added as guides.

and had relative large uncertainties. Discrepancies with past LIF work may also be related to the sample temperature, preparation details and impurity levels.

We have considered whether the apparent increases in Boltzmann temperature for titanium and iron could be artifacts of laser bandwidth effects [40] [41]; however, the present work do not believe this to be the case since: 1) The current work finds that (as expected) the Boltzmann temperature is independent of current (and such measurements would also suffer from analogous laser bandwidth effects owing to varying absorption signals with changes in current); and 2) numerical estimation of lineshape effects for our experimental conditions (lineshape ratio and peak absorbance to cavity loss ratio) suggests their role will be minimal [41].

One conclusion from these measurements (and consistent with past work) is that the details of the ground state multiplet excitation are not generally critical to determining the overall species population, since over a relatively broad range of

(Boltzmann) state distributions a high fraction of the total population resides in the ground state multiplet. For example, for all species studied here, greater than 95 % of the total population is in the ground state for an assumed Boltzmann temperature as high as 2,500 K. Even in the experiments that detected unexpectedly high number densities of energetic silver metastables, the population of those excited states was estimated as only $\sim 1\%$ of the total. Thus, from the point of view of characterizing sputter erosion and wear, measuring the population of the ground state multiplet will allow accurate determination of the overall species population. The agreement of the sputter model with experimental data further corroborates this conclusion.

2.5 Detection Limits

Estimates of minimum detectable (path-integrated) number density can be found from the noise in the CRDS detection system. For most of the measurements, the noise in the absorbance baseline is $\sim$2 ppm (for measurement times of about 30 seconds). The noise is primarily due to the relatively poor and unstable spatial mode of the OPO probe laser beam (the doubled-idler), which cause fluctuations in the ring-down signals. Pulsed CRDS experiments using dye lasers (with higher quality beam profiles) can have absorbance noise of $\sim$0.1 ppm. Table 2.2 gives experimental detection limits for path-integrated number density for noise levels (in absorbance) of 2 and 0.1 ppm. In the present experiments the path length is approximately 8 cm, so that corresponding number densities can be found accordingly. The quoted detection limits are somewhat condition (experiment) specific, and will vary with changes in energy level distributions and linewidths. The detection limits of Table 2.2 (even for 2 ppm noise) are very adequate for many applications and the conditions are representative of those frequently found in electric propulsion studies. From the point of view of electric propulsion studies, typical number densities of sputtered

particles (from eroded components) are $\sim 10^8$ cm^{-3} [10] and path lengths are order 10 cm, so that typical path-integrated number densities are $\sim 10^9$ cm^{-2}.

Table 2.2: Minimum detectable path-integrated number densities by CRDS

Noise Level	Ti(cm^{-2})	Mo(cm^{-2})	Fe(cm^{-2})	Al(cm^{-2})
2 ppm	$\sim 7 \times 10^7$	$\sim 6 \times 10^6$	$\sim 6 \times 10^7$	$\sim 6 \times 10^6$
0.1 ppm	$\sim 4 \times 10^6$	$\sim 3 \times 10^5$	$\sim 3 \times 10^6$	$\sim 3 \times 10^5$

2.6 Summary

In this chapter, the quantitative detection of several sputtered metal species using CRDS has been discussed and results presented. For each measured species, measurement validation is performed against a sputter model. Also, the excitation of sub-levels of the ground state multiplet for aluminum, iron, and titanium are studied. From these studies, one can conclude that the overall species population can be found from the population of the ground state multiplet to within several percent. The detection limits of the CRDS measurement system are also presented and are found to be very adequate for electric propulsion studies.

Chapter 3

Velocity Measurements

3.1 Introduction

The flux of sputtered particles is required for the computation of the erosion rates and sputter yields. In order to determine the flux of sputtered particles, one needs to measure not just the number density of sputtered particles but also their velocity (distributions). Chapter 2 discussed number density measurements using CRDS. A wide variety of laser and optical techniques may be employed for non-intrusive velocity measurements in the gas phase. Techniques such as filtered Rayleigh Scattering (FRS), Laser Induced Fluorescence (LIF), and laser absorption probe individual atoms (or molecules) within the flow field, and velocity information is found from Doppler shifts associated with the motion of the atoms under investigation using Equation 3.1.

$$\Delta\nu/\nu_0 = V_0/c (= V\cos\theta/c) \tag{3.1}$$

where V_0 is the velocity component of $\vec{V}$ parallel to the optical (X) axis, $V = |\vec{V}|$, and θ is the angle between $\vec{V}$ and the optical axis. In these techniques, an external frequency reference measurement (e.g. from a stationary scatterer or absorber) is generally required to precisely determine the Doppler shift and velocity.

In this chapter, CRDS-based velocity measurements of gas phase sputtered particles are presented. Velocity information is inferred from Doppler shift contributions to the absorption lineshape. Because, in CRDS, the laser beam propagates back-and-forth within the optical cavity, a measured absorption feature is both up- and down-shifted, i.e. it is split, by the velocity component parallel to the optical axis. The splitting of the absorption features allows direct velocity measurements without requiring an external frequency reference. In this chapter, the CRDS velocity measurement approach is demonstrated for atoms of different species in a low-pressure (collisionless) environment. In addition, Laser induced Fluorescence (LIF) is used to make velocity measurements of sputtered Fe atoms, and these measurements are used to validate those by CRDS.

3.2 Approach

As mentioned earlier, CRDS is widely used for measuring number densities (absorbances) of trace species or weakly absorbing species. Because of its path integrated nature (not a point measurement technique), CRDS is typically not used to make velocity measurements. However, in principle, because of its absorptive nature CRDS can be used to measure bulk velocity from Doppler shifts associated with the velocity component(s) parallel to the optical axis. Furthermore, because the laser beam propagates back-and-forth within the optical cavity, the light absorption for a moving particle is Doppler shifted both up- and down- in frequency as shown in Fig.3.1. (For example, an atom that is moving towards the "left-going" beam is simultaneously moving away from the "right-going" beam.) If the associated Doppler shift is large compared to the absorption (and laser) linewidth, then the measured absorption feature is split into two peaks, and the peak separation (split) provides a direct velocity

measurement using Eq. 3.1. This is analagous to velocimetry by conventional absorption, where the Doppler shift from the external reference provides the velocity information.

Note that in conventional absorption approach (as well as LIF and FRS), the relative laser frequency i.e. frequency separation of the measured and reference peaks must be known; however, with CRDS the seperation of the two measured peaks directly gives the velocity. Thus, in addition to being able to study weak absorptions, application of CRDS velocimetry also has the practical advantage of not requiring a precise frequency (offset) reference measurement. As will be shown, in cases with multiple velocity groups or relatively broad absorption transitions, the CRDS lineshape profile can still be analyzed to extract velocity information. As with all absorption approaches, the spatial resolution of CRDS is limited by its path-integrated nature.

3.3 Mathematical Formalism

Velocity measurements using CRDS presented in this work are limited to use with linear cavities in cases where the cavity's spectral transmission profile (i.e. etaloning) does not have any effect on measured absorption lineshapes [41]. Such an analysis applies to the case of time-averaged, pulsed laser measurements using free-running ring-down cavities (as in the current work), as well as to certain implementations of continuous-wave CRDS, cavity enhanced absorption spectroscopy, and integrated cavity output spectroscopy. The current work is also limited to the common case of single-exponential ring-down signals, where the measured lineshapes correspond to an effective lineshape found by convoluting the laser lineshape with the absorption lineshape [41].

Under these assumptions, expressions for the Doppler shifted lineshape $S(\nu)$ for an optical transition with line-center frequency are derived. The development is

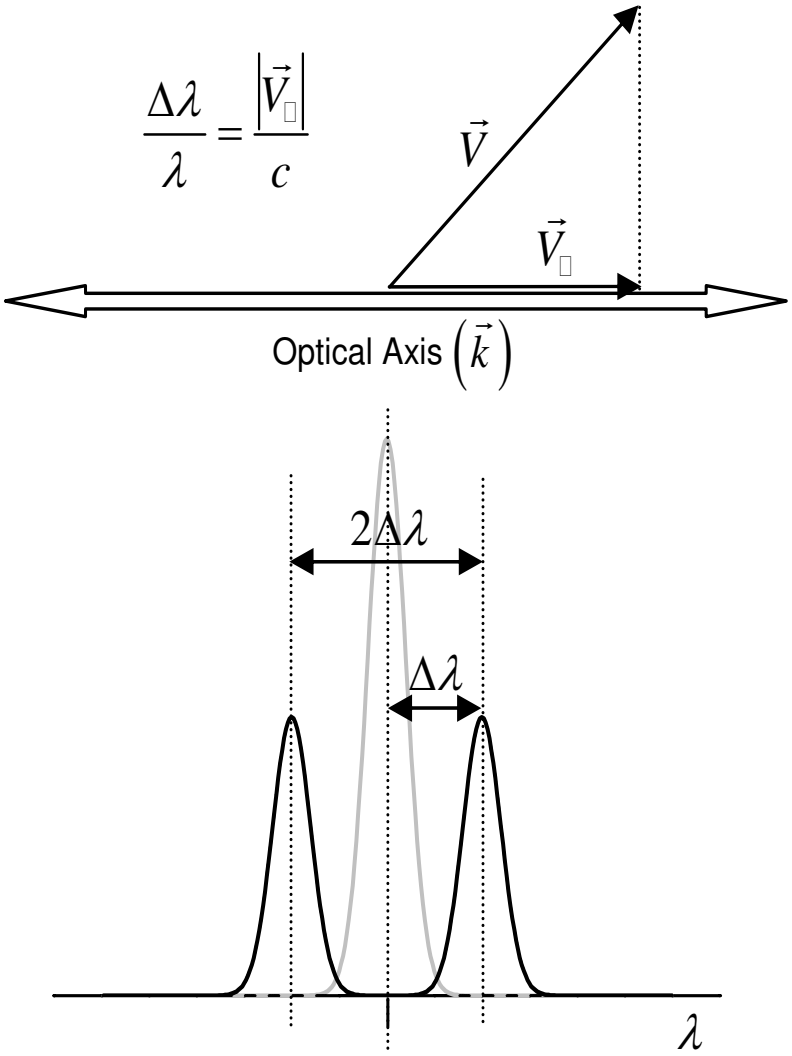

Figure 3.1: Top:Schematic of velocity vector ($\vec{V}$), CRDS optical axis ($\vec{k}$ vector points both directions), and velocity vector parallel to optical axis ($\vec{V}$). Bottom : Measured CRDS lineshape (black) has both up- and down- shifted peaks. The separation of the shifted peaks, $2\Delta\lambda$, gives the parallel velocity component $|\vec{V}_0|$. The unshifted lineshape is shown in gray.

analogous to the common Doppler broadened lineshape associated with the Maxwell-Boltzmann (MB) distribution, but here a generalized spatially-dependent velocity (number density) distribution $n(\overrightarrow{V})$ is considered. At a given location, the number density of particles with velocity$(\overrightarrow{V}, \overrightarrow{V} + d\overrightarrow{V})$ is equal to $n(\overrightarrow{V}|d\overrightarrow{V}|)$. (Note that one can also define a flux density distribution $f(\overrightarrow{V})$, where $(n(\overrightarrow{V}) = f(\overrightarrow{V})/\overrightarrow{V}$.) The lineshape contribution $S_{\overrightarrow{V},x}(\nu)$ from a single velocity group $(\overrightarrow{V}, \overrightarrow{V} + d\overrightarrow{V})$ at a given position $(x, x + dx)$along the optical axis is:

$$S_{\vec{V},x}(\nu) = c_1 n(\vec{V})(\delta(\nu - \nu_0 - \Delta\nu) + \delta(\nu - \nu_0 + \Delta\nu)) \tag{3.2}$$

where c_1 is a normalization constant and the delta functions correspond to up- and down- Doppler shifted peaks. For non-relativistic speeds, the frequency-shift $\Delta\nu$ associated with $\overrightarrow{V}$ is given by Eq. 3.1

Assuming a distribution of velocities is present, the lineshape contribution $S_x(\nu)$ at position $(x, x + dx)$ is found by integrating over the velocity distribution, yielding a series (distribution) of peaks corresponding to the velocities present in the distribution:

$$\begin{aligned} S_x(\nu) &= \int S_{\vec{V},x}(\nu) d\vec{V} \\ &= c_1 \int n(\vec{V})(\delta(\nu - \nu_0 - \Delta\nu) + \delta(\nu - \nu_0 + \Delta\nu)) d\vec{V} \end{aligned} \tag{3.3}$$

Equivalently, if $n(\overrightarrow{V})$ is expressed as a distribution of the form $n(V_0)$ (by integrating over V_y and V_z) then $S_x(\nu)$ simplifies to:

$$S_x(\nu) \propto [n(V_0) + n(-V_0)](\propto \frac{1}{\nu - \nu_0}[f(V_0) + f(-V_0)]) \tag{3.4}$$

where V_0 is associated with ν through equation 3.1, i.e. $V_0 = c(\nu - \nu_0)/\nu_0$. Equation 3.4 is analogous to that used in LIF analyses [35], except that in LIF the

probe beam in unidirectional, so each velocity group gives a single shifted peak (not a pair of split peaks). The resultant Doppler shifted lineshape $S(\nu)$ is found by integrating Equation 3.3 or 3.4 over the extent of the beam:

$$S(\nu) = \int S_x(\nu) dx \tag{3.5}$$

where spatial dependences of $n(\overrightarrow{V})$ or $n(V_0, \theta)$ and should be included in the integration. In an experiment, the overall measured lineshape, $S'(\nu)$ is found by convolution with the absorption lineshape $A(\nu)$, where $A(\nu)$ has the standard contributions from laser (instrumental), thermal, pressure, natural and other broadening mechanisms.

3.4 Experimental

To directly demonstrate the splitting of the absorption lines discussed above, it would be desired to set up an experiment where one has mono-energetic (single velocity) and mono-directional particles (at an angle θ from the optical axis). However, in reality, sputtering is a complex process where the sputtered atoms are ejected in all directions and with a velocity distribution (non mono-energetic). As a result, all the associated Doppler shifts (for each value of velocity and angle θ) superimpose on each other to form a single broadened lineshape and the splitting will not be directly apparent. For initial demonstration of the measurement technique, several attempts were made at producing the scenario of mono-energetic particles and mono-directional particles.One such scenario is presented here.

The chamber shown in Fig. 3.2 is used to demonstrate the Doppler measurement technique. Initial attempt was to use a collimated ion beam so that there is a single velocity group and a well defined shift in the measured CRD spectrum. In order to have a relatively strong absorbance signal in these initial tests it is preferable to probe

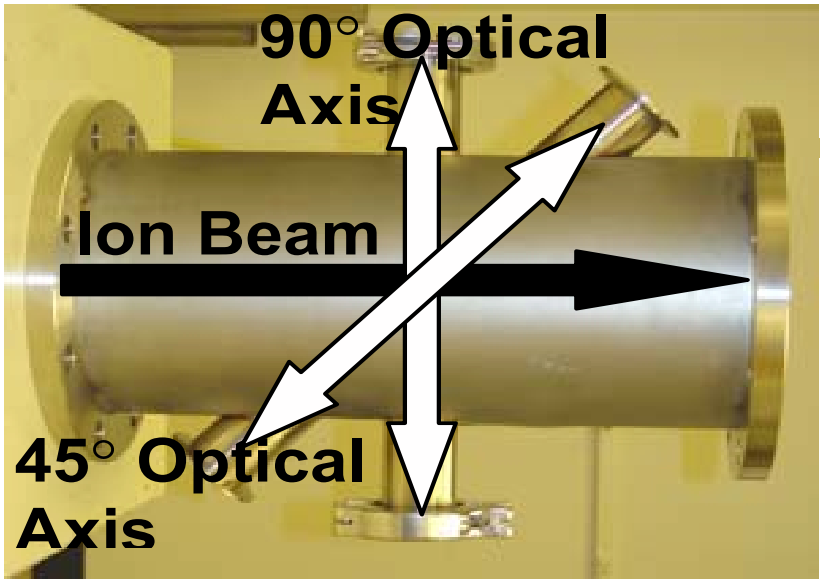

Figure 3.2: Vacuum chamber with arms for 2 optical axes with different angles.

an atomic ion. However, there are a limited number of atomic ions with absorption lines that are optically accessible by CRDS (since CRDS can not be used in the far-UV and VUV owing to poor mirror reflectivity at short wavelengths). A configuration to run Dysprosium ions (Dy^+) in our ion beam was investigated. Dysprosium was selected owing to its relatively strong and optically accessible transitions. Since Dy is a solid with relatively low vapor pressure our intent was to introduce a Dy target surface within the ion beam source which will operate (initially) on argon. Argon ions will impact the Dy surface thereby sputtering neutral Dy atoms into the discharge, some of which should be ionized and accelerated with the ion beam. The simulations show that if an ion beam current of Dy^+ of roughly 1 mA can be generated, it should be readily measurable with our CRDS system. Figure 3.3 shows simulated absorbance spectra for Dy^+ for both the 90° orientation (no ion velocity component along optical axis and no shifting) and for the 45° orientation (with ion velocity component along optical axis and shifting). However, attempts at producing such a metallic ion source failed and are not discussed further.

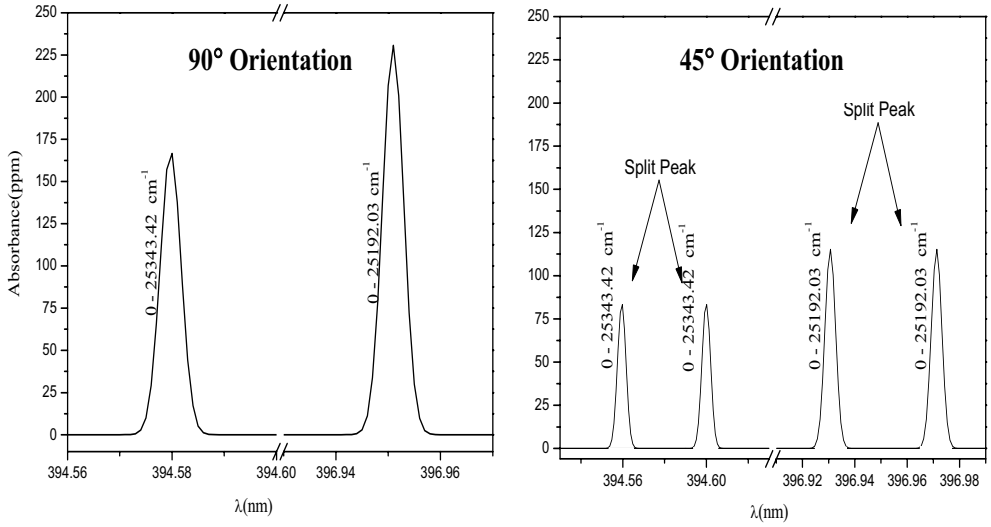

Figure 3.3: Simulated CRSD absorbance spectrum for Dy^+. Left spectrum is for the 90° orientation (of Fig.3.2) and has no Doppler shifts; the right spectrum is for the 45° orientation (of Fig.3.2) for which there is an ion velocity component parallel to the optical axis causing Doppler shifts (splitting) of the absorbance peaks. The simulations assume a dysprosium ion beam current of 1mA, a beam voltage 400V, a path length of 8 cm, and a temperature of 600 K. The modeled signals are well above our CRDS detection limit of 3 ppm.

Figure 3.4: Photograph of HCS

Given the above, a mono-directional velocity distribution (without the requirement of mono-energetic particles) was considered. Experimentally, this was achieved by fixing a honeycomb-like structure (HCS) normally onto the target. A photograph of the HCS is shown in Figure 3.4.

The HCS acts as a directional filter allowing only particles ejected normal to the target ($\sim 20°$) to be transmitted through the HCS to the measurement volume. The optical axis is oriented at 45° to the surface normal direction, so that the normally ejected particles have a non-zero velocity component (Doppler shift) on the optical-axis. Experimentally, a new chamber as shown in figure that has optical axis at 45° was designed so that it would integrate with the old chamber. As mentioned earlier, if the velocity distribution were sharply peaked, then $S(\nu)$ would be composed of two sharp peaks (one up-shifted and the other down-shifted). However, the velocities of the sputtered atoms follow a distribution which tends to smear the peaks (since different velocity amplitudes have different shifts). We assume a Thompson distribution of the form [11] [29]:

$$n(V) = \frac{V^2}{(V^2 + V_b^2)^{n+1}}; V_b = \sqrt{\frac{2E_b}{M}} \tag{3.6}$$

where E_b is the binding energy, M is the molar mass of sputtered atoms, and the exponent n is taken as any value from 1.5-2 (if n is 2, the distribution is peaked at $V = V_b$). Unless stated otherwise, the current work assumes n=2 [48]. The velocities predicted by Eq. 3.6 compare favorably with those predicted by TRIM simulations [49], which is considered as a validation of the assumed distribution.

The CRDS velocity approach is demonstrated using the similar experimental setup presented in Chapter 2 with the addition of new chamber in Figure 3.2. The doubled idler beam of a Nd:YAG pumped OPO laser system is used to measure weak absorption features of sputtered atoms in the vicinity of 375-400 nm. The laser lineshape is experimentally found to be well fit by a Lorentzian with FWHM=0.002 nm. An ion beam is normally incident on the target, and the optical axis of the CRDS system probes the cloud of sputtered particles ejected from the target (8 cm above the target). As discussed in Chapter 2, the chamber pressure is $\sim 10^{-5} - 10^{-6}$ torr, so that the sputtered atoms are in a collisionless free-molecular regime (Knudsen number $<< 1$) and pressure broadening is negligible. The velocities of the sputtered particles follow Thompson distributions (not MB) as predicted by linear-cascade theory. At these conditions, the only significant contributions to the measured lineshape $S'(\nu)$ are the Doppler shifted lineshape $S(\nu)$, and the laser lineshape $L(\nu)$ (i.e. $A(\nu) \approx L(\nu)$).

Hyperfine splitting and isotopic spectral shifts have not been included in the current model, but in principle should be considered. Such splits would result in line broadening making actual lines effectively wider than what is modeled in the current analysis. Such splittings are generally less than several GHz, which would correspond to a velocity error of $\sim$100 m/s (comparable to the error bar in the current measurement). For example, for Mo, the worst case scenario is that these contributions are

$\sim$0.005 nm, found from the width of the individual splitting contributions of Fig. 3.5, in which case the resulting error in velocity would be $\sim \pm$ 300 m/s (10%). However, these contributions are expected to be considerably smaller since the experimental data is well matched with the model (as you will see in the following sections) that contains broadening due to the velocity distributions.

3.5 Results

The velocity measurements for different species are presented and compared to theoretical predictions. First, the results obtained for mono-directional particles are presented followed by the velocity measurements for the more complex field of sputtered particles.

3.5.1 Mono-directional sputtered particles

3.5.1.1 Molybdenum

Figure 3.5 shows experimental data showing split peaks for an ion beam current of 60 mA and ion beam voltage of 900 V. The data is fit using the formalism given above (Section 3.3) and assuming a Thompson distribution (Equation 3.6) with V_b as a free (fit) parameter. The best fit is obtained for V_b=3500 m/s (uncertainty 10%), which is in good agreement with a calculated value of V_b=3700 m/s based on (tabulated) E_b=6.82 eV [47]. Uncertainty in the fit is primarily due to noise in the data (owing to low absorbance levels of $\sim$20 ppm in this configuration). The effect of the laser convolution (which further smears the peaks) is included in the fit. If a similar experiment were performed with absorption or LIF, a single peak would be detected. These measurements are the first demonstration of CRDS velocimetry performed in this way [50].

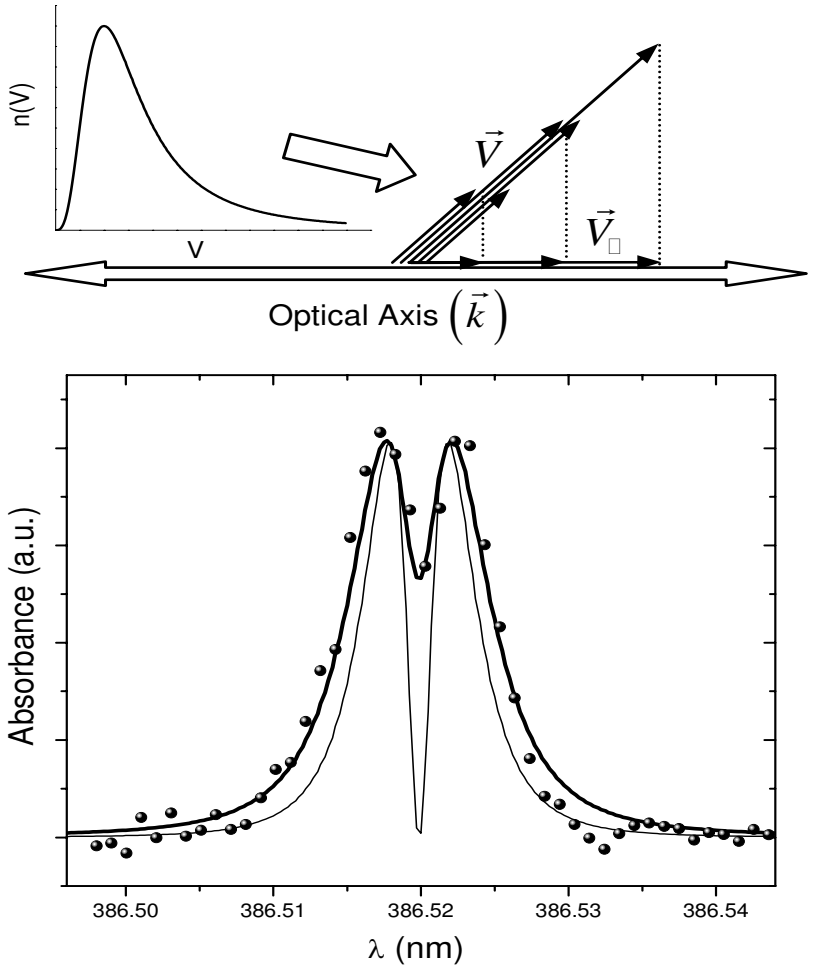

Figure 3.5: Schematic representation of CRDS optical axis with multiple unidirectional velocity vectors ($\vec{V}$) oriented at 45° , and projections on optical axis ($\vec{V}$). Inset shows velocity distribution $n(V)$. Bottom: Symbols - measured lineshape; Thick line - modeled fit with V_b=3500 m/s; Thin line - modeled fit without laser convolution (shown for reference with arbitrary vertical scale).

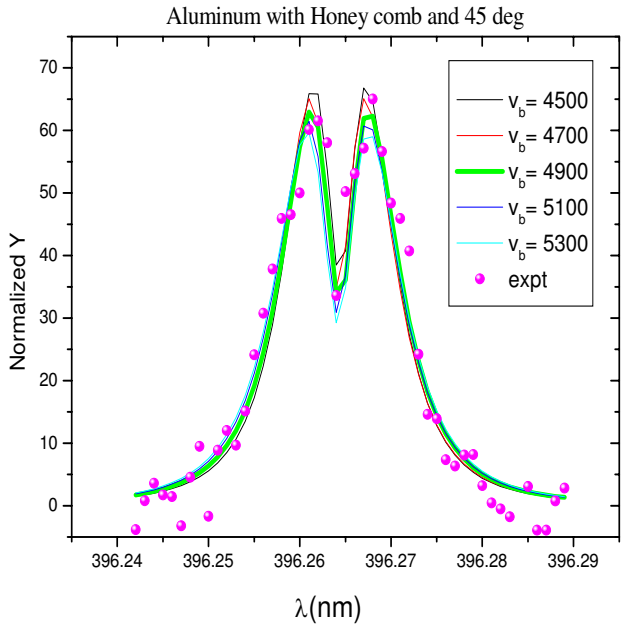

Figure 3.6: Al velocity measurements:Symbols - measured lineshape; Thick lines - modeled fit with V_b ranging from 4500 m/s to 5300 m/s

3.5.1.2 Aluminum

In a similar way, velocity measurements using an Aluminum target were performed. Figure 3.6 shows experimental data showing split peaks for an ion beam current of 60 mA and ion beam voltage of 900 V. We fit the data using the formalism given above (Section 3.3) and assuming a Thompson distribution (Eq.3.6) with V_b as a free (fit) parameter. We find the best fit for V_b=4900 m/s (uncertainty ∼10 %), which is in good agreement with a calculated value of V_b=4900 m/s based on (tabulated) E_b=2.96 eV ([47]) for Al.

3.5.2 Complex velocity field

Considering the agreement between the CRDS velocity measurements for unidirectional particles and the theoretical predictions as validation for the mathematical framework laid out in Section 3.3, the approach is extended to show results for a more complex velocity field obtained without the honeycomb filter. In this case, sputtered particles are ejected from the target in all directions (like in a regular sputtering experiment), and the optical-axis is oriented perpendicular to the surface normal (parallel to the target). The Doppler lineshape is formed from a continuum of peaks associated with the different directions and velocities of sputtered particles crossing the beam, and takes the form of a single broadened peak, similar but not the same as for a MB distribution. Note that the lineshapes presented here are analogous to the ones presented in chapter 2, meaning that the same lineshape allows determination of both number density and velocity of the sputtered particles.

In this case also, the data is fit using the formalism given above (Section 3.3) and assuming a Thompson distribution (Eq.3.6) with V_b as a free (fit) parameter. Computationally, the sputtering target is treated as a series of finite elements. The directionality of the sputtering from each site is assumed to follow a differential sputter

yield $y(\alpha)$ with a diffuse shape, i.e. $y(\alpha) \propto \cos(\alpha)$ where α is the ejection angle relative to the surface normal. The velocity distribution n(V) is assumed to be independent of α .

3.5.2.1 Molybdenum

Figure 3.7 shows experimental data for sputtered Mo for a beam current of 18 mA and beam voltage of 750 eV. Again,the experimental data are fit using V_b as a free parameter yielding best fit for V_b=3500 $\pm$ 200 m/s.The agreement with the expected values of 3700 m/s is reasonable, and the discrepancy is thought to be primarily due to effects of a non-diffuse differential sputter yield ("over-cosine" or "under-cosine" behavior), and/or velocity profiles having slight variation with the ejection angle α [35] . Even in the case of a relatively complex velocity field the velocity information is inferred from the Doppler shifted lineshape. These measurements are the first demonstration of CRDS velocimetry performed in this way [50].

Additional measurements of molybdenum are presented in Chapter 4. The sputter model used in Chapter 4 takes in to account the measured differential sputter yield, $y(\alpha)$ and experimentally measured current density of the ion beam. Note that the $y(\alpha)$ measurement does not depend on magnitude of velocity and should be done "first". In that case, the experimental data is fitted and the best fit is found for a characteristic velocity of V_b=3700 $\pm$ 100 m/s with n= 1.54, which is in good agreement with the expected value of 3700 m/s (based on the binding energy of 6.82 eV for Mo). This suggests that using the measured differential sputter yield will enable measurements of velocity with better accuracy.

3.5.2.2 Aluminum

The velocity of sputtered aluminum is inferred in similar way. The lineshapes presented in Chapter 2 are are fitted with V_b as free parameter using the sputter model.

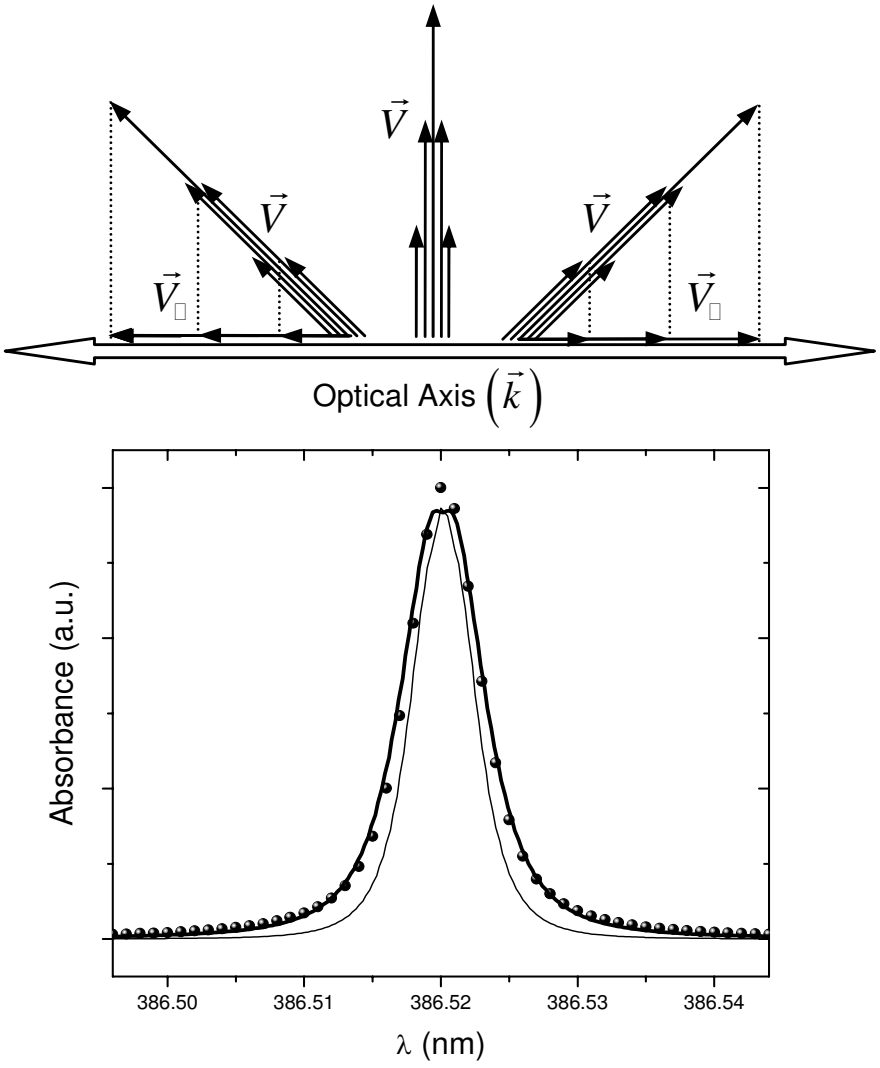

Figure 3.7: Schematic representation of CRDS optical with multiple velocity vectors ($\vec{V}$) of differing directions and magnitudes, and their projections $\vec{V}$. Bottom: Symbols - measured lineshape; Thick line - modeled fit with V_b=3500 m/s; Thin line - modeled fit without laser convolution (shown for reference with arbitrary vertical scale).

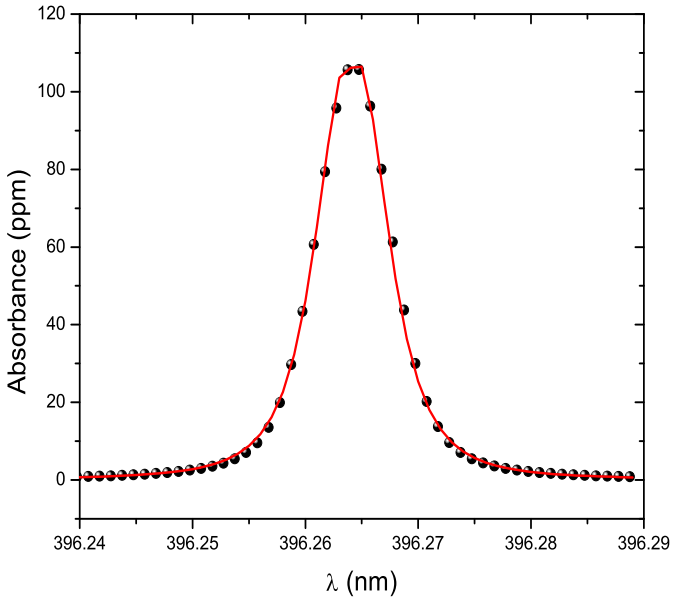

Figure 3.8: Al absorbance lineshape: Symbols - measured lineshape; Thick line - modeled fits with V_b=4900 m/s;

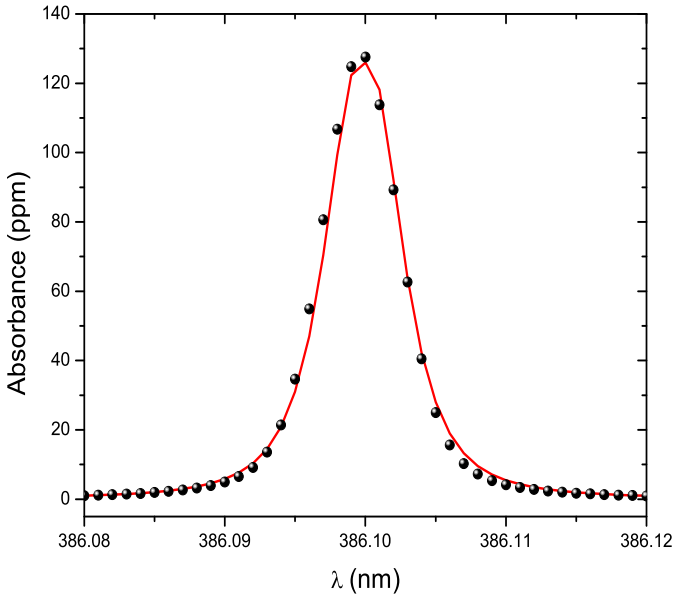

Figure 3.9: Fe absorbance lineshape: Symbols - measured lineshape; Thick line - modeled fits with V_b=2900 m/s;

The best fit is found at V_b=4900 ± 200 m/s as shown in Figure 3.8, in reasonable agreement with the expected value of 4900 m/s. Note that Al partial energy level diagram (given in Chapter 2) has two fine structure levels within the ground state mulitplet and both the lines were presented. Analyzing both the lineshapes with the same formalism yielded same velocity of 4900 m/s within the error bar indicating that velocity of sputtered particles is same from all the levels within the multiplet. This is consistent with the LIF measurements reported in the literature [48], [27].

3.5.2.3 Iron

Similarly, iron is used as the target material and the velocity of sputtered iron particles is obtained. Again,the experimental data are fit using V_b as a free parameter yielding the best fit for V_b=2900 ± 150 m/s while the predicted value is 3900 m/s as shown in Fig. 3.9. This discrepancy is due to the value of n in the Thompson

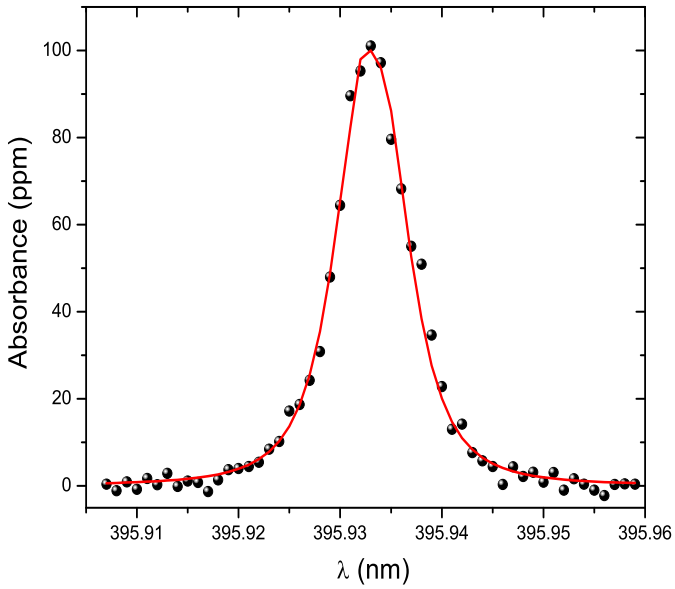

Figure 3.10: Ti absorbance lineshape: Symbols - measured lineshape; Thick line - modeled fits with V_b=4200 m/s;

distribution, and further discussion is deferred to Section 3.6. Velocity measurements are similarly made for all the measured lineshapes within the multiplet and within the experimental error, the V_b values are same, which are consistent once again with references [48], [27].

3.5.2.4 Titanium

Similar measurements were performed with titanium as target. For Ti, the best fit is obtained for V_b=4200 $\pm$ 200 m/s while the predicted value is 4400 m/s as shown in Fig. 3.10.

3.6 Validation

3.6.1 Laser Induced Fluorescence

3.6.1.1 Introduction

LIF is a highly sensitive diagnostic that may be used to measure erosion rates in real-time. In LIF, a laser is tuned to a transition in the target species. The light excites the target neutrals or ions, and the subsequent fluorescence of the excited state is detected. If the excited state of the target species is saturated and the plasma induced fluorescence (PIF) is much less than LIF, then the intensity of fluorescence is directly proportional to the density of the original (pre-excited) state. When the overwhelming majority of atoms or ions are in the ground state, and the ground state is excited by a laser, the fluorescence intensity is proportional to the species density.

LIF can also be used to measure the velocity of target species. By scanning a laser near a known transition, the wavelength distribution of the fluorescence intensity is broadened based up on the species velocity distribution along the path of the laser. Consequently, LIF may be used either to directly detect the density of erosion products or, where those products are too sparse, to measure the ionic species density and velocity distribution to calculate erosion.

3.6.1.2 Theory

As shown in Figure 3.11, consider a two level model with N_1 and N_2 being population of atoms in the ground state and excited state respectively. If one neglects collisional excitation of atoms to the upper state, the only means of exciting the atoms to the upper state is by absorption of incident light of frequency,ν. The atoms in the upper state are depopulated by stimulated emission (W_{21}), Spontaneous emission (A_{21}), and collisional de-excitation (Q_{21}). In LIF, one measures the spontaneous emission and the measured fluorescence signal is proportional to the number density of atoms in the upper state. The fluorescence intensity, S_f, measured (in W/m^3) is given by,

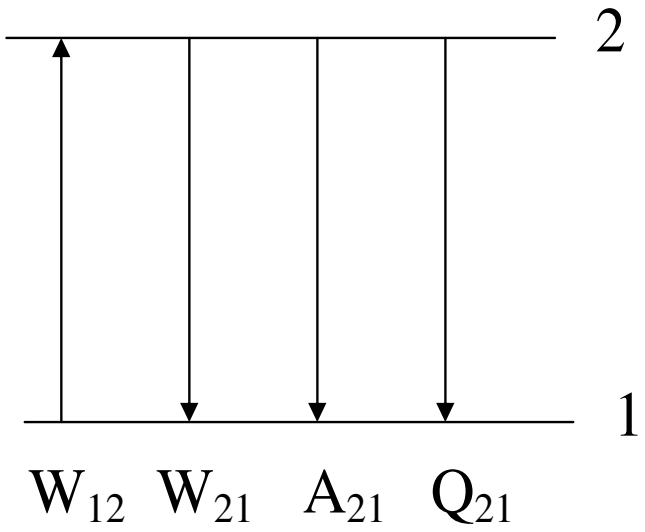

Figure 3.11: Two level model with N_1 and N_2 being population of atoms in the ground state and excited state respectively. More details are presented in the text.

$$S_f = \eta_d \frac{\Omega}{4\pi} A_{21} h\nu_{21} N_2 \tag{3.7}$$

where η_d is the detector efficiency, A_{21} is the Einstein A coefficient, and Ω is the solid angle collected in measuring the signal.

LIF is normally performed in two regimes: Linear regime and saturated regime. Briefly, In linear regime, the measured lineshape signal is directly proportional to the number density which is good. And using Doppler shifts, one could capture the velocity information from the lineshape analysis that will be presented later. However, one has to calibrate the instrument to get absolute number density signals as quenching is an unknown quantity and often varies from experiment to experiment. But in experiments where you do not care about absolute measurements, this will be of great use. In saturated regime, all the information associated with the lineshape is lost in as the measured signal has no dependence on the measured LIF lineshape ($u(\nu)$). So velocity measurements can not be made in this regime.

3.6.1.3 Lineshape Contributions

The measured LIF lineshape, $u(\nu)$, in unsaturated case, is the convolution of two functions. The first contribution is due to natural broadening,$L(\nu)$ which is Lorentzian, while the second contribution is from the combined Doppler shift and broadening. The Doppler shift for a particle moving with velocity V is given by equation 3.1. Now if one considers a group of particles with a normalized velocity distribution $f(V)$, they all will see the Doppler effect and so the resultant lineshape will be shifted by the bulk velocity and broadened by thermal width of the distribution. Hyperfine splitting is assumed to be negligible here. If the splitting structure is well known it can also be included in the model, i.e. the measured lineshape needs to be deconvoluted with the known information [51]. Another type of broadening that can be observed, if not careful with saturation, is saturation broadening. This is difficult to model and so one has to always check and make sure they are not saturating.

3.6.1.4 LIF Experimental Setup

The experimental setup is as shown in Figure 3.12 and primarily consists of a sputtering apparatus and LIF setup housed in a vacuum facility. The sputtering apparatus is as used for CRDS measurements (Chapter 2). The LIF setup uses a broadly tunable optical parametric oscillator (OPO) laser system (doubled idler) pumped by a Nd-YAG laser as the light source to probe the optical transitions of interest. The laser energy is reduced with an attenuator prior to entering the window of the chamber in order to be free from saturation effects. A wave meter is used to determine the accurate spectral position of the laser that corresponds to zero-velocity. This will serve the purpose of the external reference from which the Doppler shift can be calculated. Two windows are present in the chamber, one to allow the incident

light and the other to collect the fluorescence signal. The target is equipped with a long slit, through which the laser beam can be adjusted. The scattering volume is positioned at $\sim$ 40 mm in front of the bombarded target area. The fluorescence light is collected by a large aperture lens system and detected using a PMT connected to a data acquisition system. (Data acquisition system consists of an amplifier, a boxcar integrator, an oscilloscope and a computer with appropriate power supplies and cables.)

3.6.2 LIF results

Laser Induced Fluorescence is used to study the velocity of sputtered Fe atoms with 750 eV Ar+ ion beam bombarding an iron target. The Fe atoms are excited at 302.152 nm and the fluorescent light is collected at 382.043 nm. The collected spectrum is converted to velocity and shown in figure 3.13. The LIF data is then best fit using Thompson velocity distribution (Eq. 3.6). There are two parameters, namely V_b and n, that can be varied to obtain the best fit for the data. In Chapter 4, both V_b and n are set as free parameters. Here, the best fit for the data is first obtained by fixing n=2 and setting V_b as free parameter, yielding V_b=2900 m/s (as found with CRDS in Section 3.5.2.3). Alternatively, the data is best fit with V_b fixed at 3900 m/s (the predicted value) and using n as free parameter, yielding n=2.6. The later approach is used here and note that, within the experimental error, the raw profile can be analyzed either ways without losing much information . Later, TRIM [49] is used to predict the velocity of sputtered Fe atoms. The obtained velocity distribution from TRIM is best fit setting n as free parameter (and fixing V_b) and find that n=2.33 is the best fit. Figure 3.13 also shows the raw data along with the best fit for the data (n=2.6) and TRIM predicted profile (n=2.33). This will allow the comparison of the velocity in simplified manner.

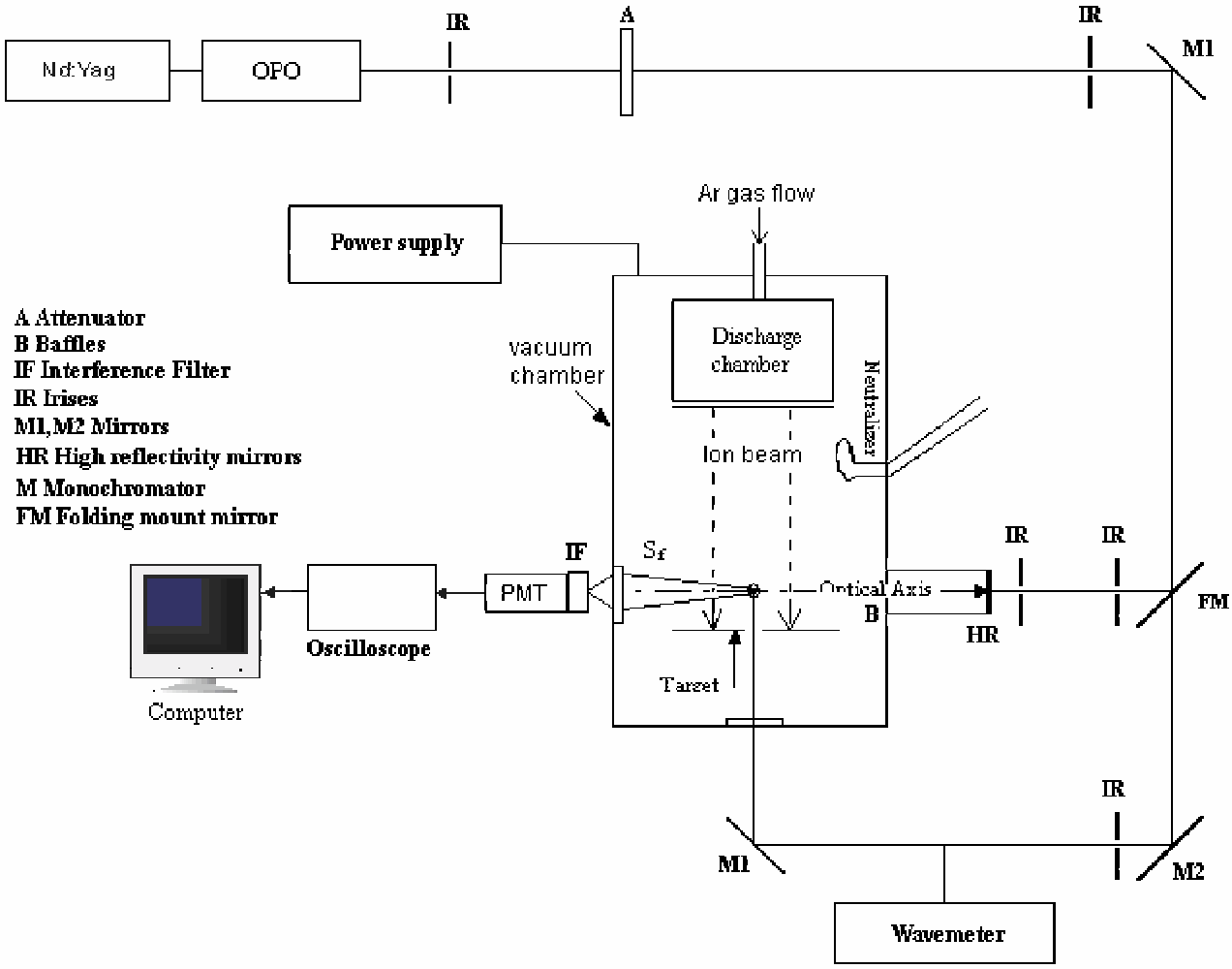

Figure 3.12: Schematic diagram of typical experimental setup for LIF sputter detection system.

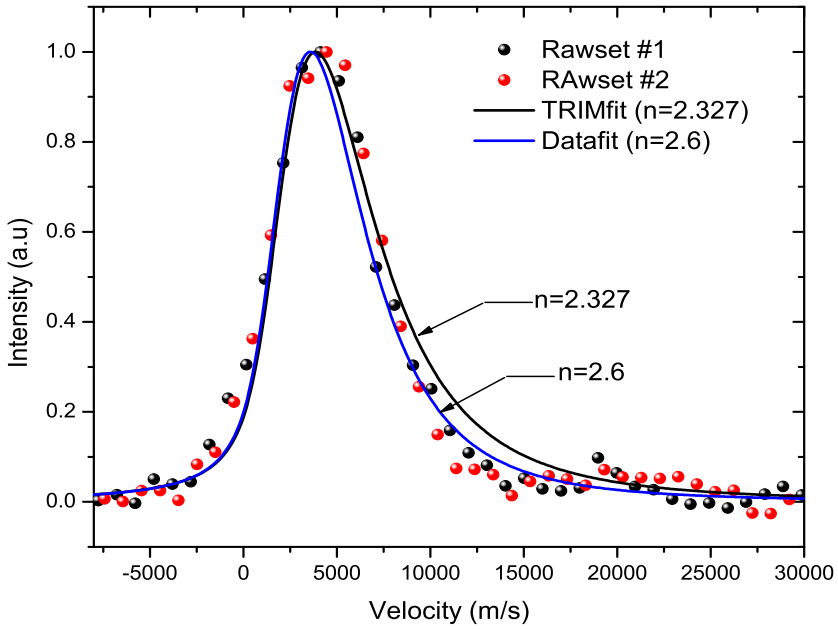

Figure 3.13: LIF measurements with X-axis converted to denote the velocity of sputtered particles. Symbols: Experimental points obtained using LIF. Solid lines: TRIM simulations (n=2.327), and Thompson distribution with V_b=2900 m/s and n=2.6

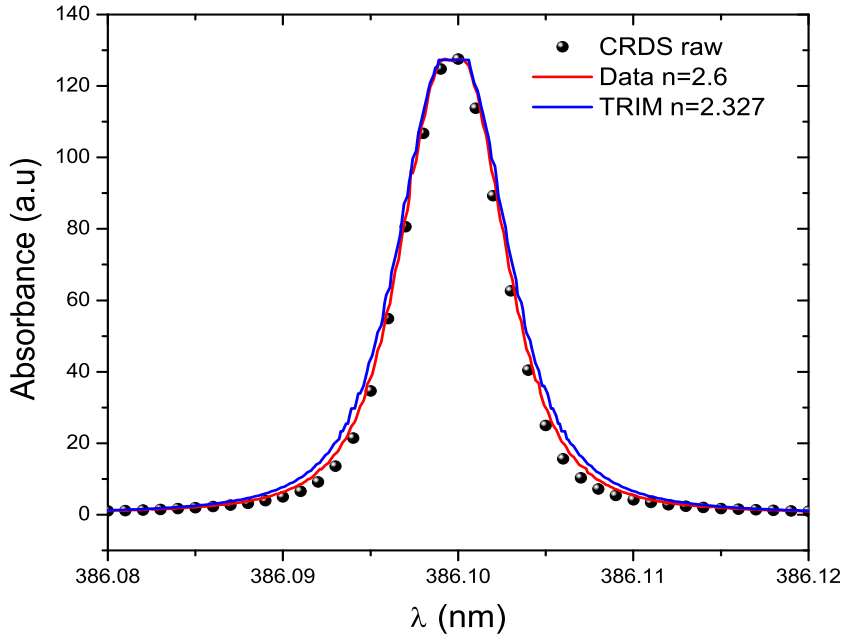

Figure 3.14: Comparison of CRDS measured lineshape with the sputter model predicted lineshape using LIF measured profile as the velocity distribution (instead of assuming the form of Eq.3.6)

3.6.3 Comparison with CRDS measurements

In Figure 3.14, the points represent the raw CRDS measured lineshape. The solid line is the CRDS lineshape modeled (with sputter model) using the measured LIF velocity distribution (best fit with n=2.6 if one uses the Thompson distribution of Eq.3.6). One can clearly see that the lineshapes from both the experiments correspond to the same velocity distribution. LIF is very widely accepted in the literature to measure velocity distributions and so this agreement is considered as a validation for the CRDS measurement and also for the sputter model that takes into account all the mathematical formalism in Section 3.3.

3.7 Summary

In summary, CRDS was used to make velocity measurements. The technique was first demonstrated for mono-directional particles for which good agreement was found with expected values. Then, the technique was extended to the more common condition where sputtered particles eject in all directions and also found very good agreement with expected values in this case. Finally, good agreement with LIF measurements was found which is taken as validation of the CRDS measurement and the sputter model. With this ability added, CRDS can be used for computing the flux of sputtered particles, from which one can also determine sputter yields and erosion rates. However, it should be noted that the hyperfine structure and isotopic splitting have not been incorporated into the existing model and should be considered in future work.

Note that the CRDS velocity measurement technique presented here is well suited to measurements in low-pressure collisionless environments since the overall lineshape is dominated by the Doppler shifts. Such measurements are useful for both fundamental studies of sputtering as well as for material characterization for electric propulsion, nuclear, and process monitoring applications. Typically, LIF has been used for such velocity measurements, and does have the advantage of superior spatial resolution. On the other hand, CRDS does not require external frequency reference and is more amenable to simultaneous number density measurement; so the two techniques can be viewed as complementary. Probing with a narrower linewidth laser would increase measurement accuracy, allowing determination of detailed velocity profiles, the study of slower particles, or measurements in cases where other lineshape contributions (e.g. pressure or thermal broadening) are larger.

Chapter 4

Differential Sputter Yield Measurements

4.1 Introduction

CRDS is used to measure the number density [52], [53] and velocity [50] of sputtered particles as presented in chapters 2 and 3. From these quantities one can calculate (model) the flux of sputtered particles. Under appropriate assumptions, the flux can in turn be used to determine the total sputter yield, Y. However, the total sputter yield does not provide information on the trajectories of the sputtered particles, as is necessary for modeling of deposition and associated contamination effects.The differential sputter yield describes the angular profile of sputtered particles (e.g., do the particles sputter predominantly "upwards" from the target in the direction of the surface normal, or do they sputter predominantly "sideways" along the plane of the surface etc.). For example, deposited particles can cause degradation of satellite radiators or solar panels (due to changes in surface properties). The distribution of angular trajectories is described by the differential sputter yield, $y(\alpha, \phi)$, i.e. the number of sputtered particles per incident ion per steradian. (Integration of the differential sputter yield over solid angle hemisphere gives the total sputter yield.) In many cases differential sputter yields have not been measured, and in the absence

of measurement, most numerical codes assume diffuse (cosine) sputter yields. However, such an approach is ill founded since measurements show that in many cases, especially for the low ion energies relevant to EP, the actual profiles are non-diffuse in character. Here, the motivation is to employ cavity ring-down spectroscopy (CRDS) as a means to make sensitive measurements of differential sputter yield. Knowledge of differential sputter yields is also very relevant to many technological (manufacturing) processes employing ion sputtering, such as manufacture of optical films and magnetic coatings, where trajectories of sputtered particles are also critical.

Common techniques for measurement of total sputter yield (e.g. weight loss,and surface layer activation(SLA)[14]) often can not give any information on the differential sputter yield. On the other hand, deposition measurements using Quartz Crystal Microbalances (QCM)[18], quadrupole mass spectrometer (QMS) method [54] and Rutherford backscattering (RBS) techniques [23] can be used to measure the differential sputter yield. Earlier chapters have presented sputter measurements by CRDS and this chapter describes the extension to measure differential sputter yields. For normally incident ions (on isotropic materials), the differential sputter yield is symmetric about the target's surface normal and is therefore a function of only the polar angle α, measured relative to the surface normal ($\alpha = 0^\circ$ is in the direction of the surface normal, $\alpha = 90^\circ$ is in the plane of the surface). In the current approach, differential sputter yields, are determined through a spatial-scanning approach in which the CRDS optical-axis is displaced relative to the source of sputtered particles. CRDS can be viewed as being complimentary to QCM and existing measurement techniques.

The general experimental setup, although similar to earlier setup, is presented in Section 4.2. In Section 4.3, the approach for differential sputter yield measurements is discussed. In Section 4.4, finite element modeling used for CRDS measurements of angular profiles is presented. In Section 4.5, the characteristic spectra and differen-

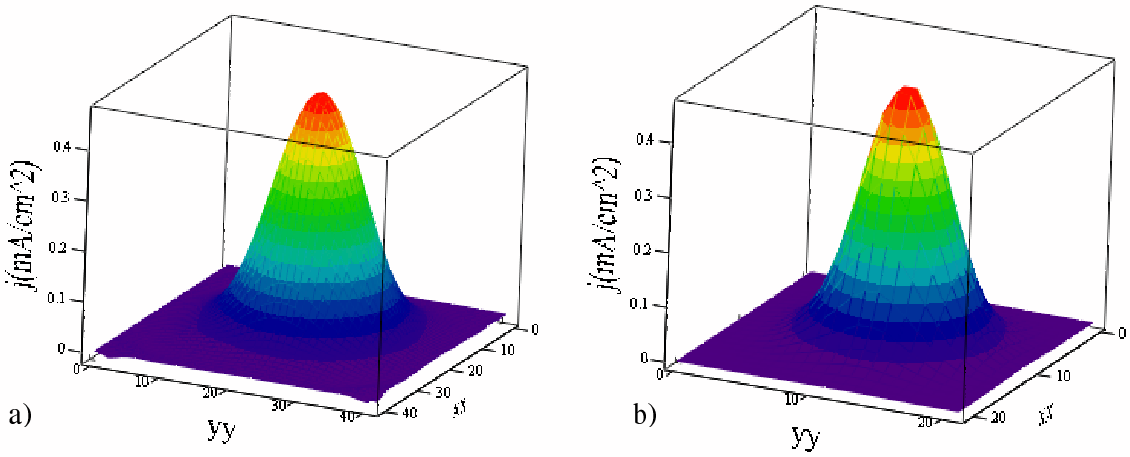

Figure 4.1: Current density profiles at Z=3 cm for beam current of 30 mA and beam voltage of 750 V. a) Measured profile. b) Polynomial fit to profile.

tial sputter yield measurements for argon ions on molybdenum are presented, while Section 4.6 gives summary and conclusions.

4.2 Experimental

The sputtering facility consists of an ion beam striking the target within a vacuum facility as presented in Chapter 2. The sputtering apparatus remains similar; however, in contrast to much of the earlier work (where 8 cm x 2.5 cm ion beam was used), the current work uses an 8 cm diameter beam. A characterization of the ion beam was conducted using a Faraday button probe to measure the current density profile [55], see Appendix A for more detail. The resulting profile of current density is shown in Fig.4.1 for a plane corresponding to 3 cm above the target. Total beam currents are generally ∼30 mA.

Also, for spatial measurements,the capability to move the target is added. Two translational stages are used for the movement of the sputtering target with a precision of ∼1 mm as shown in Figure 4.2. Note that in principle one could also move the optical axis relative to the target, but movement of the target is considerably simpler

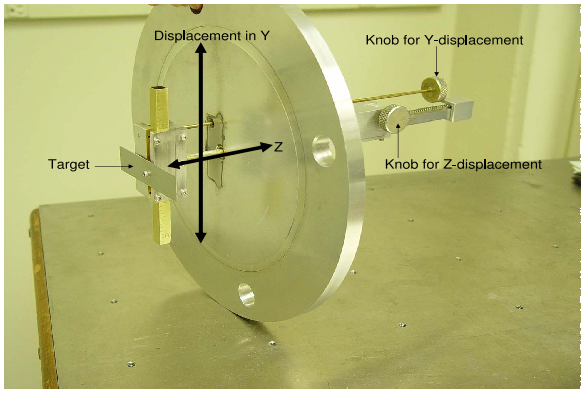

Figure 4.2: Photograph of the target mounting system.The target is in the X-Y plane and can be moved in the Y direction and in the Z-direction.

and does not affect cavity alignment. One stage moves the target in the Z-direction towards or away from the ion source (and optical axis), while the second moves the target in the Y-direction (see Fig.4.3) which is the direction perpendicular to both the optical axis and the ion beam direction. The Y-stage is used to obtain spatial profiles for the differential sputter yield measurements at fixed Z. We use Y_b to denote a given positioning of target (with Y_b=0 corresponding to the target being centered with respect to the optical axis).

4.3 Approach

The high-sensitivity of CRDS makes it attractive for measurement of sputtered particles, but its line-of-sight nature means that a single measurement gives only the path-integrated concentration and no direct measurement of the spatial variation and angular trajectories of the sputtered particles along the optical axis. Here, a means to measure the differential sputter yield is presented. For normally incident ions, $y(\alpha)$ is symmetric about the target's surface normal and is therefore a function of only the polar angle α, measured relative to the surface normal ($\alpha = 0°$ is in the direction of the surface normal, $\alpha = 90°$ is in the plane of the surface). For many materials

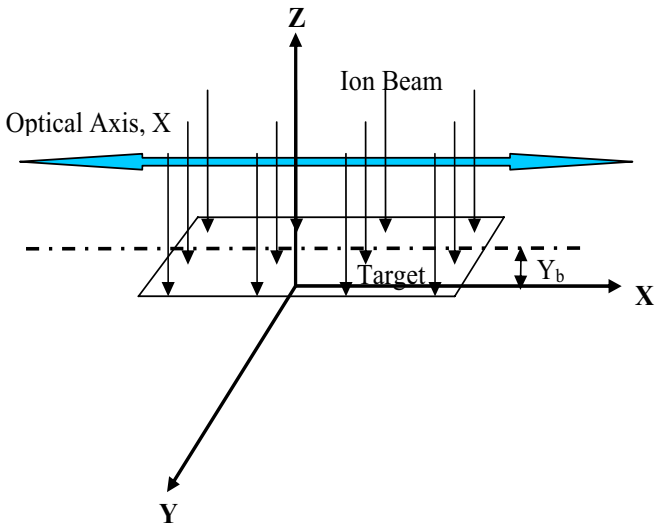

Figure 4.3: Definition of co-ordinate system used. The target is in the X-Y plane.The optical axis is at height Z above the target. The target can be moved in the Y direction and its position is denoted as Y_b.

(including Mo) extensive measurements of the differential sputter yield have not been performed (though the group at CSU is undertaking such measurements using a combination of CRDS and a quartz crystal microbalance system). In the absence of experimental measurements, numerical models tend to assume a "diffuse profile" in which $y(\alpha) = Ycos(\alpha)/\pi$, but measurement shows this tends not to be an accurate description of the true profile.

The approach to obtain the differential (angular) sputtering profile is as shown in Fig. 4.4 and is based upon displacing the optical axis relative to a planar target. A "strip" of target material is scanned laterally relative to the (fixed) optical axis. Y_b is defined as the position of the target centerline relative to the optical axis. At each lateral position Y_b, the CRDS detection system measures the path-integrated number density of sputtered particles along the optical axis. The scanning approach allows us to obtain a "Spatial Profile" which is the dependence of the CRDS signal (path-integrated number density) on the lateral position Y_b. Then, a numerical model

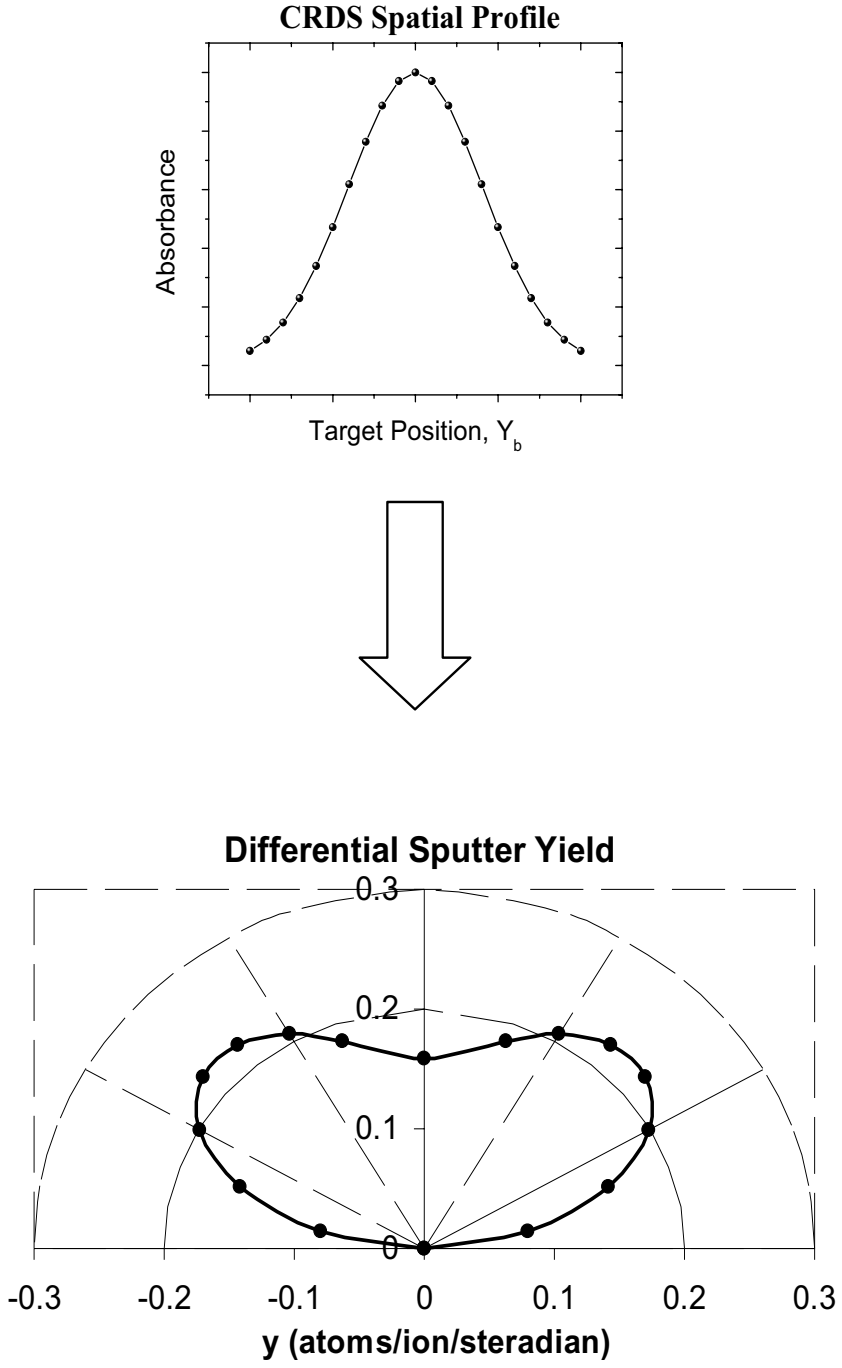

Figure 4.4: Left: The CRDS Spatial Profile is obtained by measuring the CRDS absorbance signal (Integral n dx) at a series of displacements Y_b, between the target and optical axis. Right: The differential sputter yield, $y(\alpha)$, is inferred from the CRDS Spatial Profile.

(using certain assumptions on the form of the differential sputter yield) is employed to infer the differential sputter yield, $y(\alpha)$, from the Spatial Profile. The scanning-inversion approach presented here can only be used for differential sputter yields with no azimuthal dependence (i.e. the only angular dependence is on the polar angle α), which limits its use to normally incident ions or energetic ions for non-normal incidence. Measurements for non-normal incidence could in principle be performed by incorporating appropriate forms of the differential sputter yield into the model [56]. Furthermore, theory allows inference of profiles for non-normal conditions from those at normal incidence [57]. The ion beam is nominally uniform over the full extent of target displacements, though we correct our data to account for non-uniformity of the ion beam current density (which was experimentally characterized as shown in Figure 4.1).

4.4 CRDS Finite Element Model

A finite element approach is used to model and analyze the CRDS sputtering signals (including inferring of differential sputter yield from experimental data). Figure 4.5 schematically illustrates the finite element discretization of the target and optical axis.All results presented here are insensitive to grid size.

CRDS, like other laser absorption methods, is inherently a path-integrated ("line of sight") technique. For a measurement at a given displacement Y_b (see Figure 3), the absorption line area (from CRDS) is proportional to the path-integrated number density. A finite element approach is used to calculate the path-integrated number-density by integrating (summing) the number densities along the optical axis (and finding the number density at a given point along the optical axis by integrating (summing) the sputtering contributions from each point on the target):

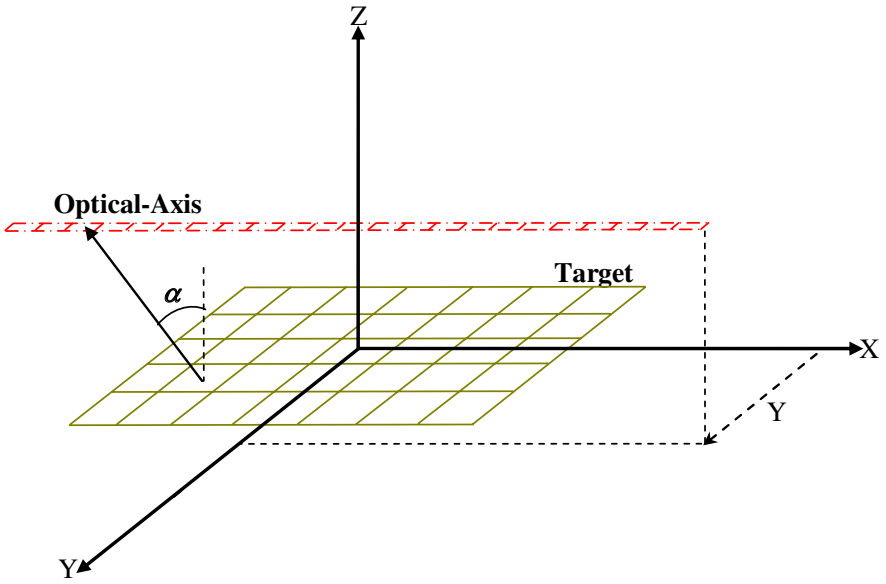

Figure 4.5: Schematic diagram of the finite element approach.

$$\int ndx \mid_{Y_b} = \int [\int \int n(r,\alpha) dA] dX \tag{4.1}$$

where α is polar angle measured from surface normal (at target element) and r is radial separation of target element to optical axis element. For the collisionless (free-molecular flow) conditions as in the current setup, the number density contribution, $n(r,\alpha)$, at a location along the beam due to sputtering from a target element is found from Equation 4.2 as shown in Fig. 4.6.

$$n(r,\alpha) = \frac{y(\alpha) I}{r^2} \langle \frac{1}{V(\alpha)} \rangle \tag{4.2}$$

Note that the number density at a location is required, not the total number of atoms in a volume. The number density contribution depends on the differential sputter yield in the given direction $y(\alpha)$, the radial separation r, the current (particles per unit time) incident on the target element i, and the inverse of the average ejection

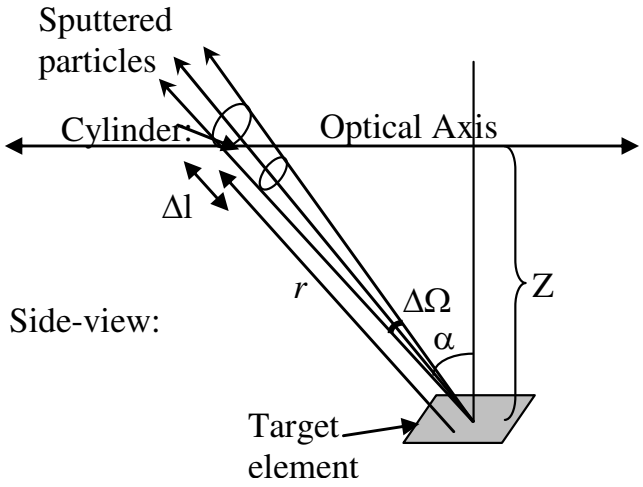

$$\frac{\#\text{atoms}}{\text{unit solid angle}\ \ \text{unit time}} = y(\alpha)I$$

$$\frac{\#\text{atoms}}{\text{unit solid angle}\ \ \text{unit length}} = y(\alpha)I\left\langle\frac{1}{V(\alpha)}\right\rangle$$

$$\#\text{atoms in "cylinder"} = y(\alpha)I\left\langle\frac{1}{V(\alpha)}\right\rangle\cdot\Delta l\cdot\Delta\Omega$$

$$\text{volume of "cylinder"} = \Delta l\cdot\Delta\Omega\cdot r^2$$

$$n(r,\alpha) = \#\text{atoms/volume in "cylinder"} = \frac{y(\alpha)I}{r^2}\left\langle\frac{1}{V(\alpha)}\right\rangle$$

Figure 4.6: Calculation of number density of sputtered particles, $n(r, \alpha)$.

velocity $< 1/V >$ (found from Thompson velocity distributions).The current on the target element is found from an experimentally measured current profile, while the other quantities are functions of the polar angle α and radius r (which are in turn computed from the relative locations of the target element and beam element).

The current incident on a (computational) target element is found from the product of the area of the target element (typically about 1 mm x 1 mm) and the current density incident at that location. To know the exact current density at each location (target site), the Faraday button probe was used as mentioned earlier. The model then uses a polynomial fit to the experimental profile as shown in Figure 4.1 b.

As in Chapter 3, an assumption that the (flux) distribution of the velocity profile of ejected particles, f(V), does not vary with polar angle is made and a Thompson distribution for the flux distribution of ejected velocities [11] is adopted as in Equation 3.6. From this distribution, one can compute the average value of inverse velocity, $< 1/V >$, required for the computation on Equation 4.2. Recent modeling shows

that there may be some dependence of the distributions on ejection angle [32], and investigation of these effects is part of the future work.

The model allows the user to compute the (path-integrated) CRDS signals, and their dependence on the target displacement position Y_b, for given differential sputter yield profiles. The approach is to infer the experimental angular sputtering profile, $y(\alpha)$, by comparing the measured spatial profile with a series of simulated profiles (and identifying the best agreement using least-squares analysis). Note that the total sputter yield is treated independently, and here the only concern is with the angular shape of the differential sputter yield. As mentioned, the case where the angular shape varies with only the polar angle (no azimuthal variation) is considered. To encompass the range of possible profiles, the current work parameterizes with a single parameter 'a' allowing a range of profile shapes between under-cosine (a>0) and over-cosine (a <0) [58]:

$$y(\alpha) = \frac{Y\cos(\alpha)}{\pi}(1 + a(1 - 2\cos^2(\alpha))) \tag{4.3}$$

Figure 4.7 shows examples of differential sputter (angular) profiles for several values of parameter a (for a total sputter yield Y=1). The assumed form (Eq.4.3) allows a range of shapes with a=0 giving a diffuse (cosine) profile, a <0 giving over-cosine profiles, and a >0 giving under-cosine profiles. Other assumed forms of the differential sputter yield profile using basis set of $cos(\alpha)^n$ with a larger number of free parameters (as opposed to the single parameter, a) are also examined and it is found that the assumed single parameter fit is adequate. (the assumed form can fit profiles measured with QCM to better than ∼5 percent standard deviation).

Figure 4.8 shows examples of simulations of CRDS spatial profiles for different differential sputter profiles. The simulations assume molybdenum target (E_b=6.82 eV) of 8 cm x 2 cm (with the 8 cm parallel to optical axis), and the optical axis at a

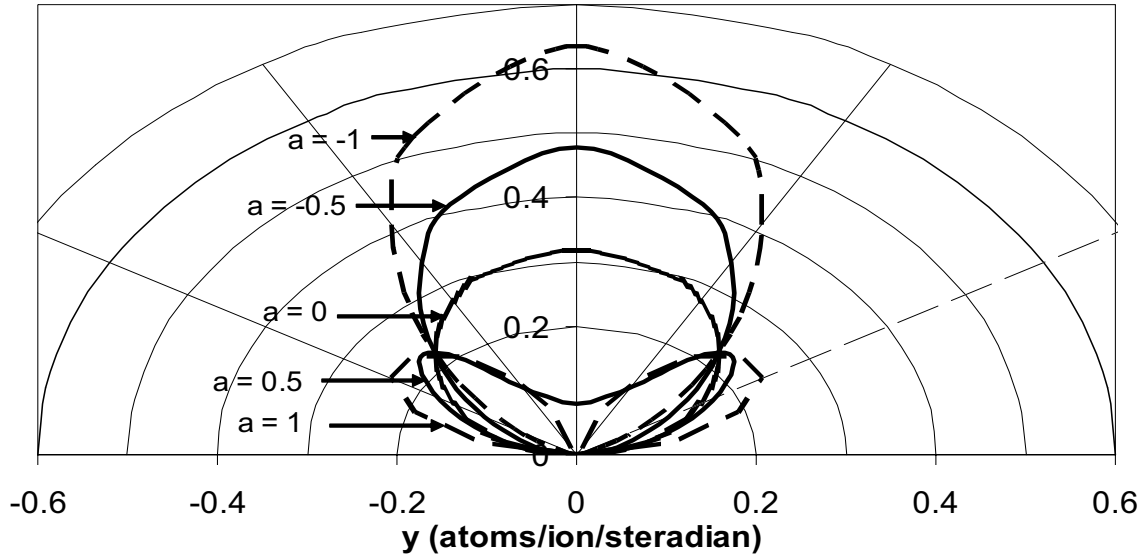

Figure 4.7: Differential sputter yield profile shapes for different values of parameter a.

height of Z=3 cm above the target plane. The peak of each profile is normalized to unity. As the a parameter increases, the sputtering profile is angularly broader, so that a larger proportion of the material is ejected away from surface normal and the spatial profiles broadens. The left/right asymmetry in the modeled curves is due to slight asymmetry in the current density profile of the ion beam.

4.5 Differential Sputter Yield Measurements

4.5.1 Molybdenum

CRDS measurements of Mo due to argon ion bombardment are obtained in the diagnostic test-bed described in Chapter 2. The CRDS scheme for detection of Mo is based on probing absorption line at 386.52 nm [44]. The experimentally measured current density profile of an 8 cm diameter beam is used. Also, the target sizes are different based on the experiment. A finite element model with dependence on $y(\alpha)$ is employed. Figure 4.9 shows the normalized absorbance spectrum of (sputtered) Mo at

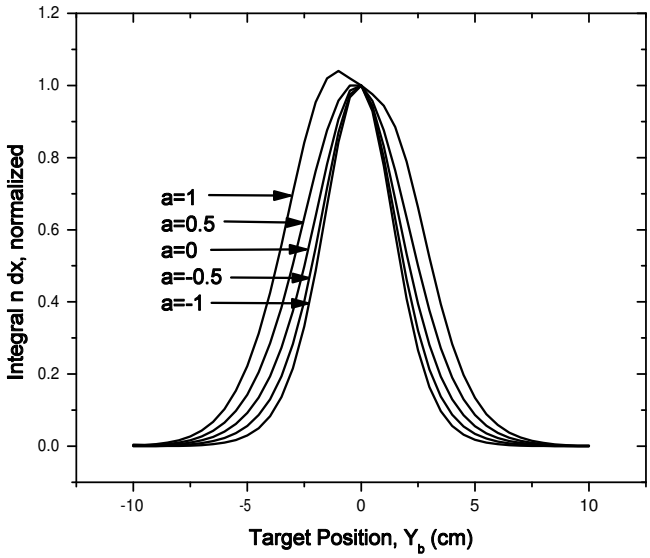

Figure 4.8: CRDS spatial profiles normalized to give unity at $Y_b = 0$

a height of Z=2 cm above the 8 cm x 4 cm target and (centered) target displacement of Y_b=0, for sputtering by a 750 eV argon ion beam.

The lineshape of the absorbance spectrum can be used to measure the velocity profile [50] as mentioned in Chapter 3 (Eq.3.6). Note that here, unlike in Chapter 3, both V_b and n are set as free parameters. Also, the model calculation requires the differential sputter yield, $y(\alpha)$, for which a=0.22 is used (see below in differential sputter yield measurements section). Note that the $y(\alpha)$ measurement does not depend on magnitude of velocity and should be done "first". The experimental data is fitted and the best fit is found for a characteristic velocity of V_b=3700$\pm$100 m/s with n= 1.54, which is in good agreement with the expected value (based on the binding energy of 6.82 eV for Mo). As a validation, the measurements on an 8 x 4 target at a height Z=3 cm are also performed, and find the same velocity. Figure 4.9 also shows the modeled lineshape corresponding to 3700 m/s.

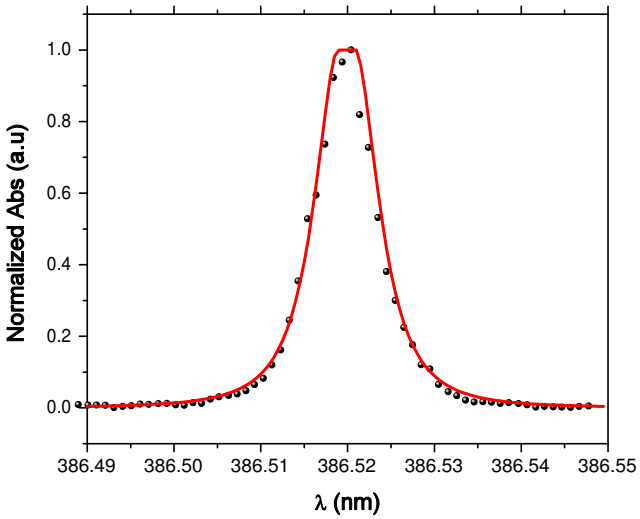

Figure 4.9: CRDS absorbance spectrum (symbols) of sputtered molybdenum at Y_b=0, and Z=2 cm. Curve shows modeled lineshape for (best-fit value of) V_b = 3700 m/s.

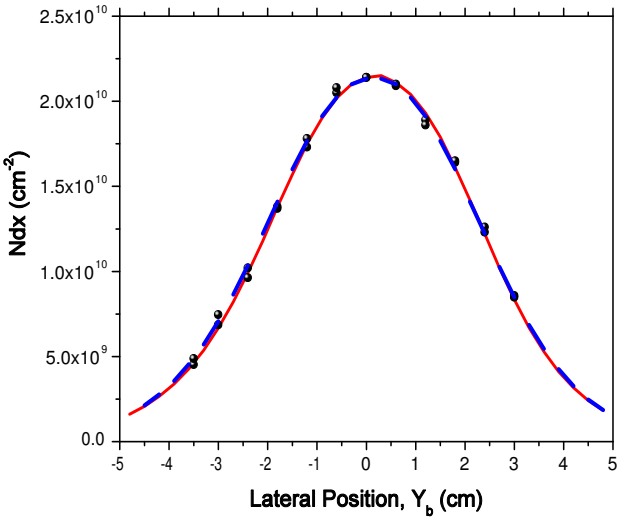

Figure 4.10: CRDS spatial profile of Mo: Symbols represent the experimentally measured points, solid line represents the best fit curve obtained from the model, and dashed line represents the curve obtained from the model using QCM coefficients.

Figure 4.10 shows the CRDS spatial profile for 750 eV argon ions on 8 cm x 4 cm Mo target at (height of optical axis above target) Z =2 cm. The spatial profile is obtained by displacing the target in the Y-direction and measuring the path-integrated concentration (CRDS line area) at each target position (Y_b). Using the sputtering model, the profile that best fits the measured spatial profile is found with $a = 0.2 \pm 0.1$ (error bar based on repeatability). The corresponding modeled profile is shown as solid line in Fig.4.10. For validation, the CRDS differential sputter yield measurements are compared with QCM measurements reported for Ar^+ ion on Mo [59]. The dashed line in Fig.4.10 represents a simulated spatial profile found from the finite element model using the QCM measured profile (expressed as a polynomial in form of $\cos^n(\alpha)$. The QCM profile is also fit with the assumed form of $y(\alpha)$ gives $a = 0.19$ which is in good agreement with the CRDS result. Similar measurements are performed at height Z=3 cm and in this case one finds $a = 0.25 \pm 0.1$, also in good agreement with the QCM measurements ($a = 0.19$). Figure 4.11 shows a polar plot of the differential sputter yield profile measured by CRDS. We average the Z=2 cm and Z=3 cm measurements (from CRDS) yielding $a = 0.22 \pm 0.07$. For comparison, a diffuse (cosine) profile is also shown, i.e. a=0, and the actual profile as measured by the QCM.

The slight discrepancy between the CRDS and QCM profiles is most likely due to: variation in the target surface condition in the CRDS and QCM tests, the assumption of angularly-independent ejection velocity in the finite element model, and/or the assumed (single parameter) form of the differential sputter yield. However, the best fit 'a' parameter of CRDS and QCM are within error of one another and both fits are qualitatively similar (slightly under-cosine) which is treated as good agreement and validation of the CRDS measurement.

Using the measured (shape of the) differential sputter yield and the absolute CRDS signals (from which the number density and velocity are measured), one can

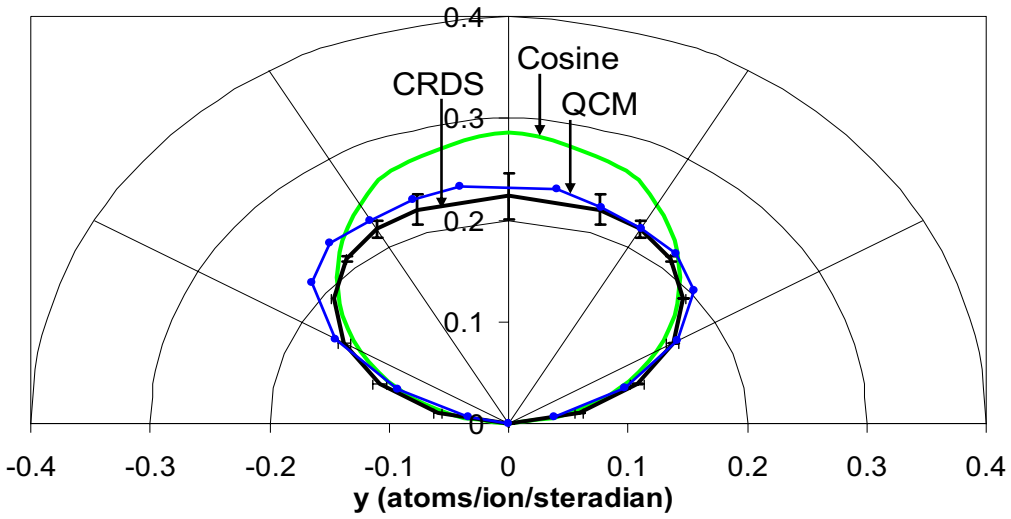

Figure 4.11: Comparison of differential yield profiles obtained at different Z's for molybdenum with that of a regular cosine distribution and the actual QCM measured profile. One can clearly see the under cosine behavior of Mo.

determine the total sputter yield. In this way, a sputter yield of 0.9±0.05 is found and in good agreement with the sputter yield of 0.9±0.3 published in Yamamura et al.[47].

4.5.2 Tantalum

CRDS measurements of Tantalum (Ta) due to argon ion bombardment are obtained in the same diagnostic test-bed described earlier. The CRDS scheme for detection of Ta is based on probing absorption line at 391.963 nm. The experimental conditions are similar to that of molybdenum. An 8 cm x 4 cm tantalum target is used. The distance between the optical axis and the target (Z) is fixed at 2 cm. A finite element model with dependence on $y(\alpha)$ is employed.

Figure 4.12 shows the CRDS spatial profile for 750 eV argon ions on 8 cm x 4 cm Ta target at (height of optical axis above target) Z =2 cm. Using the sputtering model, the profile that best fits the measured spatial profile is found with $a = 0.0 \pm 0.1$ (error

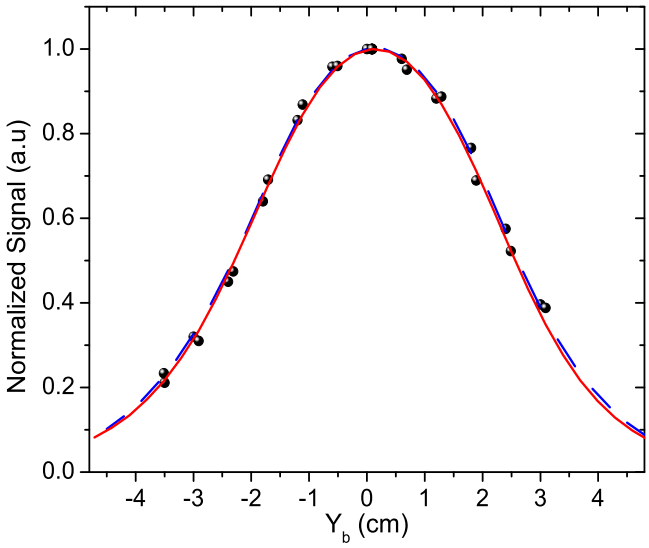

Figure 4.12: CRDS spatial profile of Ta: Symbols represent the experimentally measured points, solid line represents the best fit curve obtained from the model, and dashed line represents the curve obtained from the model using QCM coefficients.

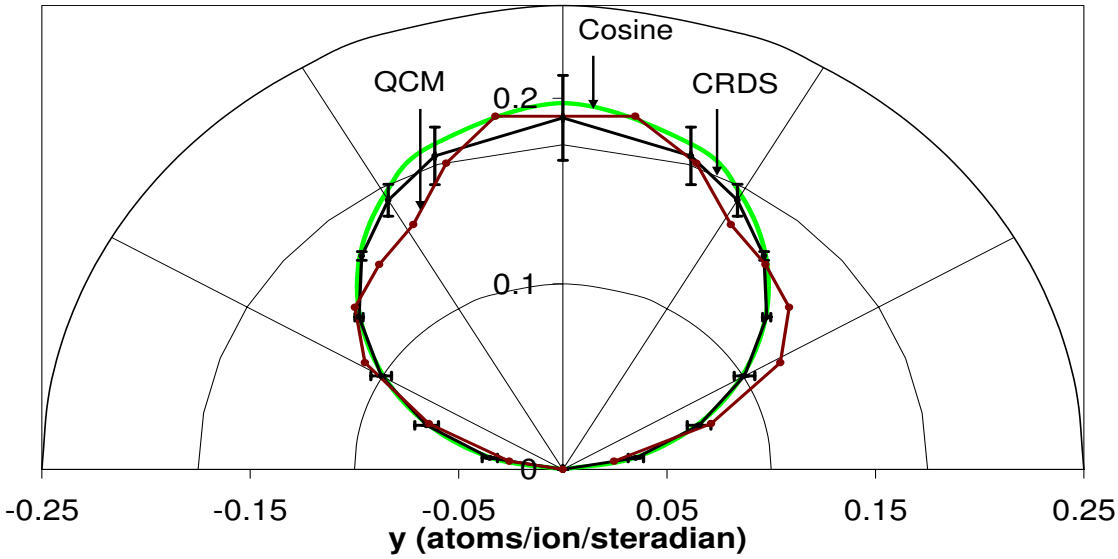

Figure 4.13: Comparison of differential yield profiles obtained for tantalum with that of a regular cosine distribution and the actual QCM measured profile. One can clearly see the nearly cosine behavior of Ta.

bar based on repeatability). The corresponding modeled profile is shown as solid line in Fig.4.12. For validation, the CRDS differential sputter yield measurements are compared with QCM measurements reported for Ar^+ ion on Ta [59]. The dashed line in Fig.4.12 represents a simulated spatial profile found from the finite element model using the QCM measured profile (expressed as a polynomial in form of $\cos^n(\alpha)$). The QCM profile is also fit with the assumed form of $y(\alpha)$ giving $a = 0.0$ which is in very good agreement with the CRDS result. Figure 4.13 shows a polar plot of the differential sputter yield profile measured by CRDS. For comparison, a diffuse (cosine) profile is also shown, i.e. a=0, and the actual profile as measured by the QCM.

Once again, the discrepancy between the CRDS and QCM profiles is most likely due to: variation in the target surface condition in the CRDS and QCM tests, the assumption of angularly-independent ejection velocity in the finite element model, and/or the assumed (single parameter) form of the differential sputter yield. However, the best fit 'a' parameter of CRDS and QCM are within error of one another and

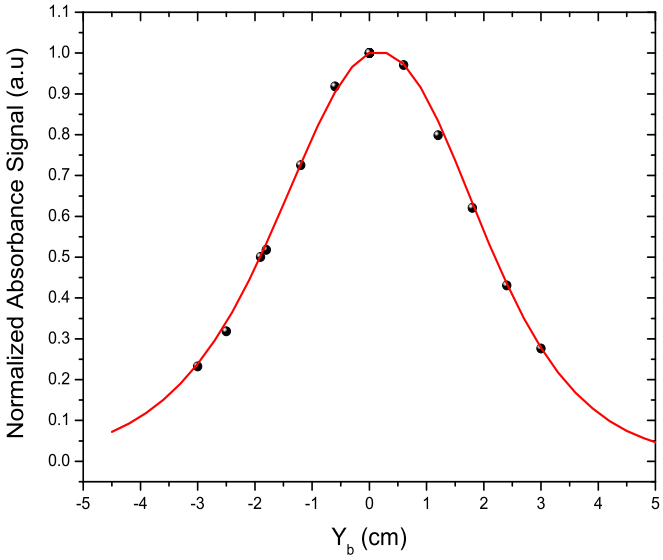

Figure 4.14: CRDS spatial profile of Ti at Z = 2 cm: Symbols represent the experimentally measured points, solid line represents the best fit curve obtained from the model.

both fits are qualitatively similar (nearly cosine) which is treated as good agreement and validation of the CRDS measurement.

4.5.3 Titanium

Considering that the differential sputter yield measurements presented earlier as validation, the measurement is extended to obtain differential sputter yield profiles for Titanium (Ti). CRDS measurements of Ti due to argon ion bombardment are obtained in the same diagnostic test-bed as described earlier [52]. The CRDS scheme for detection of Ti is based on probing absorption line at 395.933 nm. The experimental conditions are similar to that of molybdenum. An 8 cm x 2 cm titanium target is used. The differential sputter yield profiles are obtained at two cases: Z=2 cm and Z=3 cm.

Figure 4.14 shows the CRDS spatial profile for 750 eV argon ions on 8 cm x 2 cm Ti target at (height of optical axis above target) Z =2 cm. Using the sputtering model, the profile that best fits the measured spatial profile is found with $a = 0.25 \pm 0.05$ (error bar based on repeatability). The corresponding modeled profile is shown as solid line in Fig.4.14. Similary, spatial profile for Ti is obtained at Z= 3 cm. Using the sputtering model, the profile that best fits the measured spatial profile is found with $a = 0.2 \pm 0.05$ (error bar based on repeatability). Both cases yield the same profile for the differential sputter yield within the error bar as expected. The differential sputter yield profiles should not be effected by the height of the optical axis above the target(Z) and the repeatability with two different cases is treated as validation of the experimental technique.

At Z=2 cm, the CRDS path-integrated concentration is measured to be 5.5 $\times$ 10^9 cm^{-2} and velocity is 4400$\pm$100 m/s (with n=1.54). Using the sputter model to match the measured path-integrated concentration and velocity, one can determine the total sputter yield. In this way, a sputter yield of 0.75$\pm$0.1 is found in agreement within error bar with those reported in literature 0.7$\pm$0.2 [47].

4.6 Summary

CRDS usage is extended to measure differential sputter yield profiles for normally incident ions (azimuthally symmetric cases). In order to extract spatial information from line of sight CRDS measurements, inversion approaches are required. The lack of symmetry of the cloud of sputtered particles precludes the use of Abel inversion techniques. An approach that is tomographic in nature, i.e. to recover the spatially dependent differential sputter yields from spatial measurements (each of which cannot give the needed information on their own) is demonstrated. The required spatial

measurement is the profile of CRDS signal (path-integrated concentration) at a series of displacements relative to the target. Rather than using a direct inversion, modeling is used to generate simulated spatial profiles each corresponding to a different differential sputtering profile, and then seek the best agreement between the simulated profiles and measured profile. A similar approach could be used for CRDS measurements in other applications with related symmetries.

The approach has been validated for measurement of argon ions on molybdenum. The differential sputter yield profiles are characterized with a single parameter, a. For 750 eV Ar+ on Mo, the CRDS measurement yields $a = 0.22 \pm 0.07$ in good agreement with the past QCM measurements (best fit with a=0.19). Also, for 750 eV Ar+ on Ta, the CRDS measurement yields $a = 0.0 \pm 0.1$ in good agreement with the past QCM measurements (best fit with a=0.0). For Ti, the CRDS measurement yields $a = 0.25 \pm 0.05$. For a richer description of the profile shapes, or for other sputtering configurations, multiple parameters could be used to characterize the differential sputter yield. However, for such approaches to have high sensitivity, the spatial profiles must vary appreciably as the parameters are varied. In comparison with other sputter measurement techniques, CRDS has the advantages of high sensitivity (shorter measurement times), being amenable to in situ measurements (for example for device studies), and being capable of species-specific studies of multi-component materials (presented in Chapter 5).

Chapter 5

Sputtering Studies of Multi-Component Materials

5.1 Introduction

Sputter yields for many single-component materials are well known (at least for energies well above the threshold); however, the sputter yields for multi-component materials are in many cases not known. Examples of multi-component materials that are of interest to EP include boron nitride, quartz, inconel, kapton etc. These materials are used as insulators and thermal surfaces. Further, owing to the relative complexity of these materials and the sputtering processes, it is generally difficult to numerically predict their sputtering properties.

The majority of existing (non-optical) techniques do not give species specific information. On the other hand, CRDS can be used to obtain both total yields and differential sputter yields, and can be provide species specific measurements. The CRDS can in principle provide species specific differential sputter yields $y_i(\alpha, \phi)$ (i being the species for multi-component materials). In this chapter, the use of CRDS for species-specific measurements from multi-component materials is demonstrated.

The experimental setup is again similar to the earlier setup presented in previous chapters except the target species is changed to a multi-component material. The

target species used in this chapter are Inconel 718 alloy and a Fe-Mn target. Section 5.2 presents the CRDS measurements as a result of Ar^+ ion bombardment of Inconel 718 alloy. In Section 5.3, the sputtering of iron and manganese from a Fe-Mn target is presented.

5.2 Inconel 718

In this section, the CRDS measurements of inconel 718 are presented. [The major constituents of inconel 718 (by mass) as specified by the vendor are: Ni+Co $\sim 50-55\%$, Cr $\sim 15-21\%$, Fe $\sim 10-18\%$, Mo $\sim 3\%$, and Cb+Ta $\sim 5\%$. The majority of these components are optically accessible by CRDS. The present measurements include detection of molybdenum, iron and chromium.

For CRDS measurements in this section, experimental conditions are: 750 eV Ar^+ beam striking an inconel target of 8 cm (in the beam direction) by 4 cm, with the optical axis at a height Z=2 cm above the target. Prior to measurements, the target was sputter cleaned by Ar^+ ions of energy 750 eV for more than 30 minutes.

The results obtained for individual species are first presented. These results include differential sputter yield measurements, number density and velocity. Each species is treated independently and species specific values of the aforementioned parameters are obtained. As mentioned in Chapter 4, DSY measurements are performed first as these are independent of ejection velocity, V_b. The current work assumes that the ejection velocity V_b does not change with ejection angle [11] so that the species-dependent velocities have no effect in this case. Also assumed is n = 1.54 for all species for the Thompson distributions (Eq. 3.6). Finally, a comparison is made between the measured species parameters and those expected based on TRIM [49] modeling and the inconel composition.

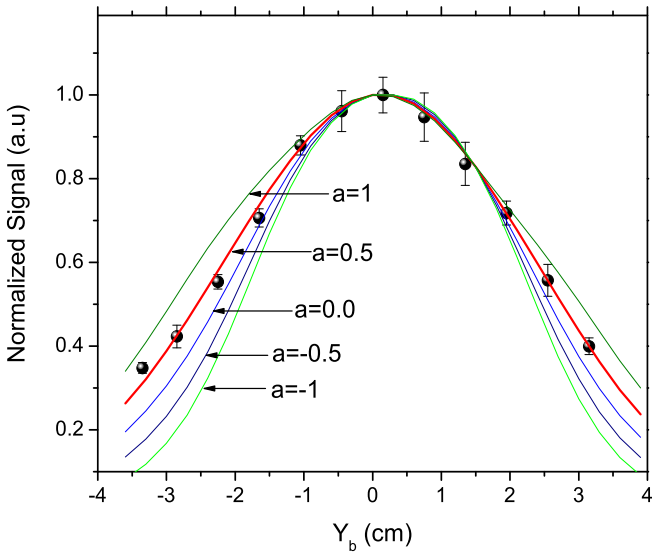

Figure 5.1: Spatial profile of sputtered Mo from Inconel. Symbols: CRDS measured spatial profile. Lines-Modeled spatial profiles using different 'a' parameter values.

5.2.1 Molybdenum sputtering from Inconel 718

The detection scheme used for Mo is based on probing the absorption line at 386.52 nm, similar to the one presented in Chapter 2. Figure 5.1 shows the measured CRDS spatial profile of sputtered molybdenum atoms from Inconel 718 sample. Also shown in the figure are simulated spatial profiles for different values of the 'a' parameter. For molybdenum, a best fit between experiment and the model is obtained for an 'a' parameter of a $= 0.5 \pm 0.2$, corresponding to an under-cosine profile shape. Note that for sputtering of molybdenum from a pure Mo sample, we found a $= 0.2 \pm 0.2$ (Chapter 4), indicating that the angular profile of the sputtering for Mo from inconel is broader (more under-cosine) as compared to the sputtering of Mo from a pure molybdenum sample. In the multi-component samples, the presence of other species influences the sputtering characteristics.

Additionally, the path integrated concentration and velocity of sputtered Mo can be obtained from the measured lineshape (as presented in Chapters 2 and 3). At the CRDS optical axis centerline (Y_b=0), the resulting Mo path-integrated concentration is $8.8 \pm 0.8 \times 10^8$ cm^{-2}. The velocity of the sputtered Mo particles (V_b) is found to be 4000± 200 m/s. The sputtered Mo atoms eject with a velocity that is slightly higher, but with error of Mo atoms from a pure target within error. A characteristic value of flux 4.4×10^{13} particles/(cm^{2}s) is found as the product of the (spatially-averaged) number density and the characteristic velocity. Really, the flux should be calculated using the number density and directional component of velocity. The measured path-integrated concentrations ($\int ndx$) and velocities (V_b) can be used in conjunction with the sputter model to predict the corresponding sputter yield, which is found to be Y_{Mo}=0.038 ± 0.005.

A comparison of sputter yields is made with TRIM simulations. TRIM is run for a multilayered target with range of compositions corresponding to the range specified by the vendor. The TRIM code also requires the binding energies (E_b) of the sputtered species as inputs, with the default values being the E_b values for pure target species (see Appendix B). If the CRDS measured V_b (corresponding E_b) is used as the input (instead of the default value), TRIM predicts Y_{Mo} to be 0.036 ± 0.01, which is in good agreement with the measured value.

5.2.2 Iron

As discussed in Section 2.2.1, iron has five fine-structure levels (J=0,1,2,3,4) within its ground electronic state. Here, only the population of the lowest-lying of these levels (J=4) is measured using the absorption line at 386.1005 nm. Following earlier work (and assuming the same population distribution (ref)) the population of this measured state is converted to the overall iron population. Figure 5.2 shows the

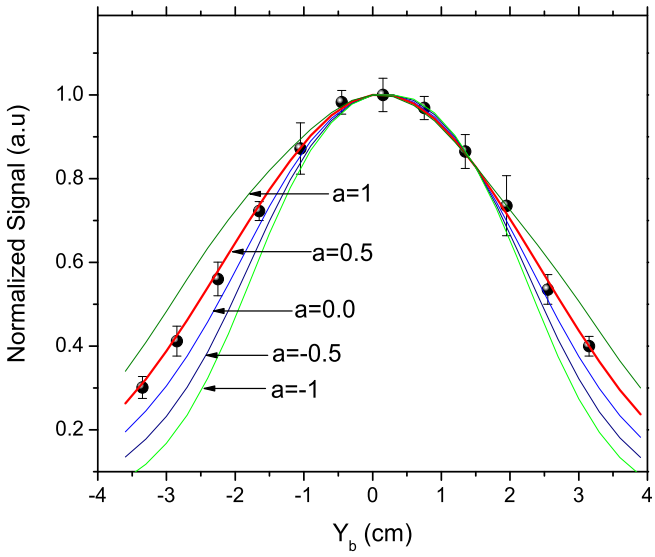

Figure 5.2: Spatial profile of sputtered Fe from Inconel. Symbols: CRDS measured spatial profile. Lines:Modeled spatial profiles using different 'a' parameter values.

normalized CRDS spatial profile of sputtered iron atoms from Inconel 718 sample. The figure also contains simulated spatial profiles for different values of 'a' parameter. For iron, a best fit between experiment and the model is obtained for a $= 0.5 \pm 0.2$, corresponding to under-cosine profiles.

The path integrated concentration and velocity of sputtered Fe are obtained from the measured CRDS lineshape. At the optical axis centerline, the resulting path-integrated concentration of Fe is $8.0 \pm 0.8 \times 10^9$ cm^{-2}. The characteristic velocity of the sputtered Fe particles (V_b) is found to be 2800±200 m/s giving a characteristic value of the flux of sputtered Fe as 2.8×10^{14} 1/(cm^{2}s). The measured path-integrated concentrations ($\int ndx$) and velocities (V_b) can be used in conjunction with the sputter model to predict the corresponding sputter yield, which is found to be Y_{Fe}=0.28 ± 0.03.

Again, a comparison of sputter yields is made with TRIM simulations. If the default value for binding energy of Fe is used, TRIM predicts sputter yield of Fe (Y_{Fe}) to be 0.19. If the CRDS measured E_b is used, TRIM predicts Y_{Fe} to be 0.32 $\pm$ 0.03, which is in good agreement with the measured value.

5.2.3 Chromium

Chromium (Cr) has only one energy level in the ground state (no fine structure) with its next lowest energy level at 0.94 eV. For typical population distributions of sputtered particles (e.g. T_B <2000 K), greater than 98 % of the overall population resides in the ground state (as assumed here) though a detailed study of these populations has not yet been made. The CRDS measurements are based on probing the absorption line at 360.635 nm. Figure 5.3 shows the measured CRDS spatial profile of sputtered chromium atoms from Inconel 718 sample. The figure also shows simulated spatial profiles for different values of 'a' parameter.For chromium, a best fit between experiment and the model is obtained for an 'a' parameter of a = -0.2 ± 0.2, corresponding to over-cosine profiles.

Again, the path integrated concentration and velocity of sputtered Cr are obtained from the CRDS measured lineshape . At the optical axis centerline, the measured path-integrated concentration of Cr is $7.41 \pm 0.7 \times 10^9$ cm^{-2}. The characteristic velocity of the sputtered Cr particles (V_b) is found to be 4400 $\pm$ 200 m/s, and the characteristic flux of sputtered Cr is computed to be 3.87×10^{14} particles/(cm^{2}s). The measured path-integrated concentrations ($\int ndx$) and velocities (V_b) can be used in conjunction with the sputter model to predict the corresponding sputter yield, which is found to be Y_{Cr}=0.31$\pm$0.03.

Again, a comparison of sputter yields is made with TRIM simulations. If the default value for binding energy of Cr is used, TRIM predicts sputter yield of Cr (Y_{Cr})

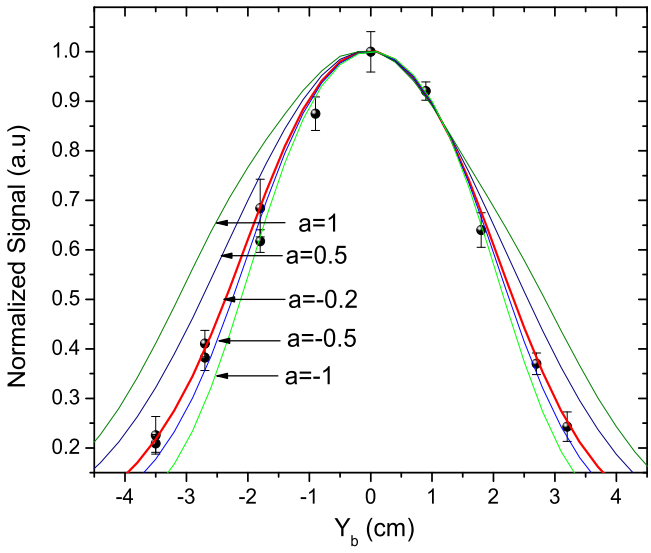

Figure 5.3: Spatial profile of sputtered Cr from Inconel. Symbols: CRDS measured spatial profile. Lines:Modeled spatial profiles using different 'a' parameter values.

to be 0.42. If the CRDS measured E_b is used, TRIM predicts Y_{Cr} to be 0.31±0.03, which is in good agreement with the measured value.

5.2.4 Summary of results for Inconel 718

Summarizing the aforementioned results, Figure 5.4 shows the normalized CRDS signals for Mo, Fe, and Cr (points), as well as modeled curves for different 'a' parameters (i.e. different shapes of the differential sputter yield profiles). One can see from the figure that the angular profiles of Mo and Fe are about the same within experimental error and both show under-cosine behavior, while the sputtering of Cr clearly shows narrower angular profile than the molybdenum and iron.

Table 5.1 summarizes results of measurements at the conditions given earlier in this section. The CRDS and TRIM sputter yields, and CRDS (characteristic) fluxes are found as described earlier. Good agreement is found between the measured and

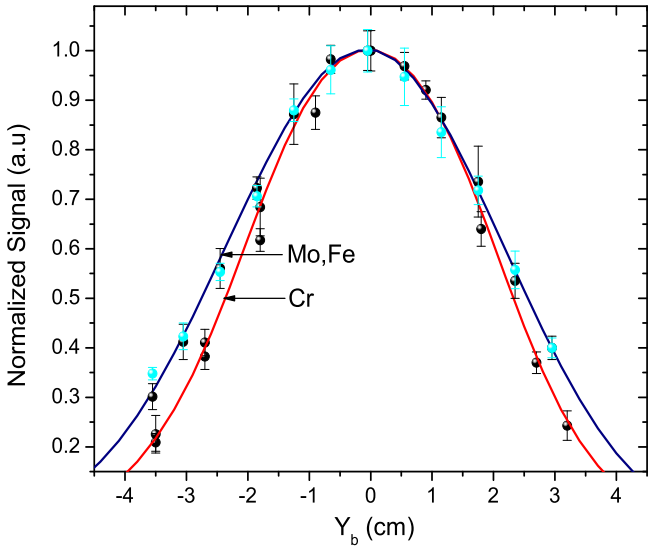

Figure 5.4: Spatial profile of sputtered Mo,Fe, and Cr from Inconel. Symbols: CRDS measured spatial profiles. Lines:Modeled spatial profiles using the corresponding 'a' parameter values.

TRIM sputter yield values. The accuracy of the TRIM results for multi-component samples in this energy range, and surface evolution effects, have not been fully explored. The fluxes of the different species being sputtered off the target are also examined and are presented in Table 5.1. At steady-state conditions, the flux of particles leaving the surface should mimic the target composition [6]. Indeed, in Table 5.1, the experimentally measured flux as well as the composition (both normalized by chromium) are presented, and agreement (within errorbars) is found between the sets of values. Note that in principle the full flux calculation should include the directionality of the sputter yields which is different for the three species, but these effects have been neglected in these situations.

Table 5.1: Summary of species specific sputter yields and fluxes for sputtering of Mo, Fe and Cr from inconel.

$Metal_i$	CRDS Y_i	TRIM Y_i	CRDS $Flux_i/CrFlux$	Composition$_i$/Cr composition
Mo	0.038±0.005	0.036±0.01	0.11 ± 0.02	0.08 ± 0.01
Fe	0.28±0.03	0.33±0.03	0.72 ± 0.14	0.88 ± 0.39
Cr	0.31±0.03	0.31±0.03	1.0 ± 0.2	1.01 ± 0.17

5.3 Fe-Mn target

In this section, initial CRDS measurements of Fe-Mn target are presented. The constituents of Fe-Mn (by mass) as specified by the vendor are: Fe $\sim$ 50 %, Mn $\sim$ 50 %. Both these components are optically accessible by CRDS and measurements include detection of both constituents. Detection of Fe is as described earlier. Detection schemes for manganese (Mn) are presented herein. Finally, the sputtering measurements of Fe and Mn from Fe-Mn are presented.

For all the CRDS measurements in this section, the experimental conditions are: 750 eV Ar^+ beam striking an Fe-Mn target of 8 cm (in the beam direction) by 4 cm,

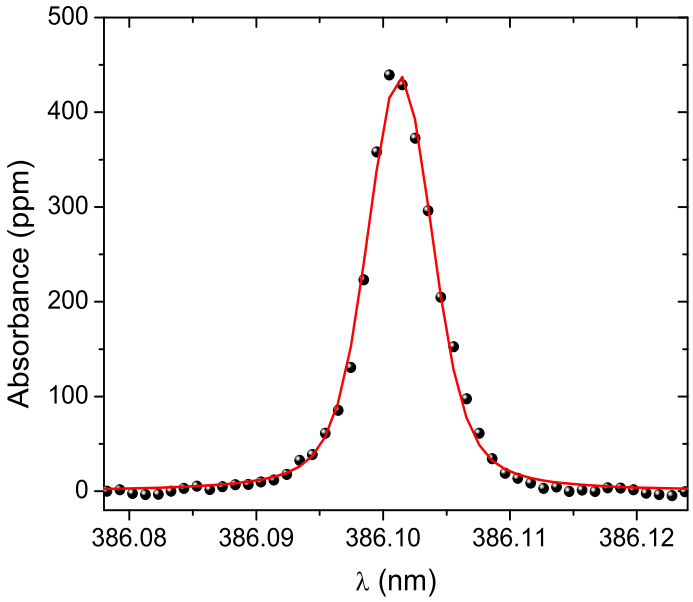

Figure 5.5: Iron absorbance spectrum from Fe-Mn target recorded by CRDS.

with the optical axis at a height Z=2 cm above the target. Prior to measurements, the target was sputter cleaned by Ar^+ ions of energy 750 eV for more than 30 minutes.

Figure 5.5 shows a representative absorbance spectrum of Fe from Fe-Mn target measured by CRDS.The path integrated concentration and velocity of sputtered Fe are obtained from the measured CRDS lineshape. At the optical axis centerline, the resulting path-integrated concentration of Fe is $1.94 \pm 0.2 \times 10^{10}$ cm^{-2}.

CRDS detection of Mn from Fe-Mn target is based on probing the absorption line of Mn in the electronic ground state $3d^5\ 4s^2$ at 403.42 nm. Manganese has no fine structure in the ground state. The next lowest energy level is at 17052.29 cm^{-1}, so that Boltzmann calculations reveal that to a good approximation all population is in the ground state. Therefore, one can use the area of the measured line to determine the ground state population, and set this equal to the overall Mn population. Figure

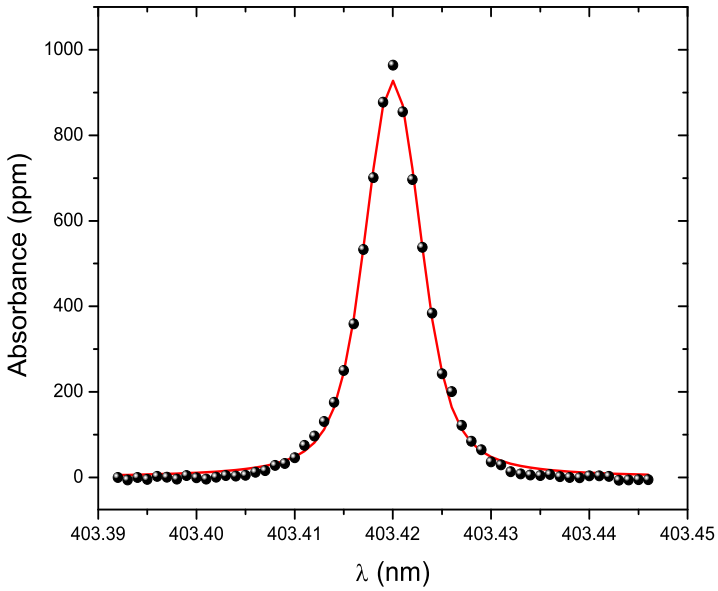

Figure 5.6: Manganese absorbance spectrum from Fe-Mn target recorded by CRDS.

5.6 shows a representative absorbance spectrum of Mn from Fe-Mn target measured by CRDS.

The path integrated concentration and velocity of sputtered Mn are obtained from the measured CRDS lineshape. At the optical axis centerline, the resulting path-integrated concentration of Mn is $1.42 \pm 0.1 \times 10^{10}$ cm^{-2}.

5.3.1 Summary of results for Fe-Mn

In summary, the detection schemes of Fe and Mn from Fe-Mn target are presented. The path-integrated concentrations of Fe and Mn are reported. The differential sputter yield measurements of Fe and Mn from Fe-Mn target have not yet been made. As a result, the discussion (comparisons with TRIM) is incomplete and considered as part of future work.

Chapter 6

Excited State Measurements

6.1 Introduction

The sputtering process is physically complex and it is known that the ejected particles contain not only ground state atoms but also atoms in excited states [60]. The formation of excited atoms ejected from sputtered surface, has been extensively investigated [61]. Over these years, several models have been developed to explain the experimental observations but recent experiments and publications [60], [61], [62], [63], [64],[65] show that the Resonant Electron Transfer (RET) model is gaining prominence. The key measurements that validate these models are the population distributions and state-specific kinetic energy distributions. The majority of published work in this field has used either resonance laser ionization spectroscopy or laser induced fluorescence spectroscopy.

In this work, as presented in Chapter 2, the total concentration of the sputtered target material is obtained by probing all the energy levels within the ground state multiplet. If there are several levels within the multiplet, it is not always convenient (possible) to probe all the levels and a characteristic temperature (from Boltzmann statistics) is often used to get the overall population. Also, based on Boltzmann statistics, an assumption was made that greater than 98 percent of the population

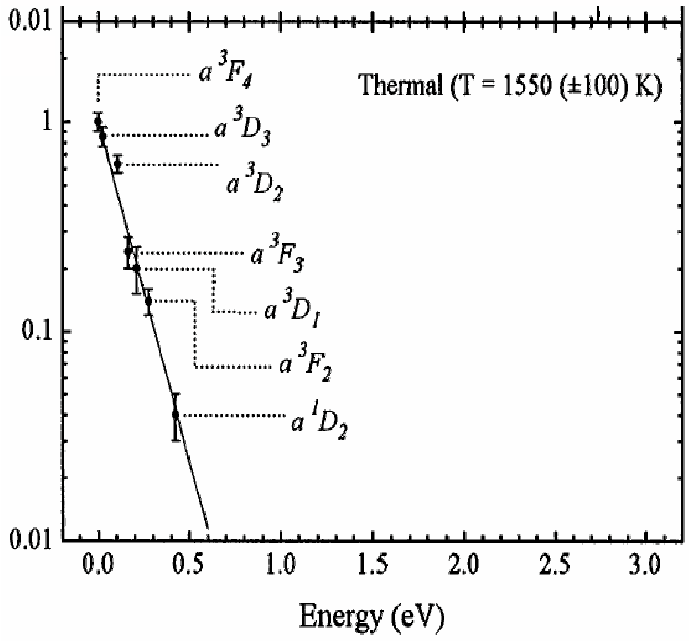

Figure 6.1: Typical plot of population distributions versus energy levels at Local thermodynamic Equilibrium (LTE).

resides in the ground state. It was mentioned that for titanium this assumption is appropriate. But, is it appropriate for all materials is the question of interest here.

Figure 6.1 shows a typical Boltzmann plot of population distributions versus energy levels for Nickel (Ni) at Local thermodynamic Equilibrium (LTE) [36]. (These particles are from a heated vapor, not sputtering.) One can see that at LTE, the plot is linear and that the characteristic temperature is 1550 $\pm$ 100 K. In this case, the energy levels do follow the Boltzmann relation. However,recent studies have shown that the populations in excited states are sometimes substantially populated and do not follow Boltzmann distributions [66] [36]. This is termed as anomalous excitation because of the significant population being present in the higher energy states. As an example, some of such results are presented in Figure 6.2. The left of Fig. 6.2 shows the sputtering of Iridium (Ir), while the right of figure shows sputtering of silver (Ag) atoms when bombarded with 13 keV Ar^+ ions. Figure 6.2 shows that

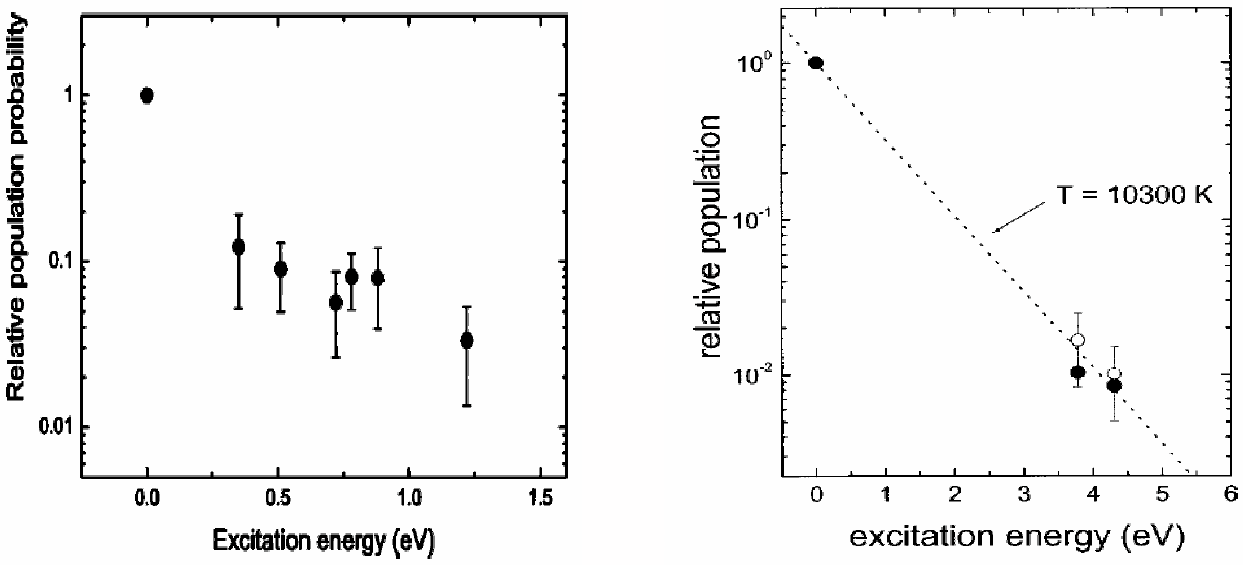

Figure 6.2: Anomalous sputtering behavior. Left: 13 keV Ar ion sputtering of Ir, Right: 13 keV Ar ion sputtering of Ag

the energy levels greater than 1 eV are significantly populated and correspond to a characteristic Boltzmann temperature as high as 10300 K, illustrating the problem of assuming Boltzmann distribution. Note that physical conditions for sputtering do not always satisfy those required for local thermal equilibrium, and therefore there is no reason to expect Boltzmann statistics and distributions.

This chapter presents CRDS-based investigation of population distributions which may shed light on the state-specific electronic processes that lead to sputtering of atoms in different excited states. Measurements are performed for Ar ions bombarding Dysprosium (Dy). The measurements are based on absorption from seven fine electronic structure levels that arise from two different electronic configurations: $4f^{10}6s^2$ ($^5I_{8,7}$) and $4f^9\ 5d\ 6s^2$ ($^7H_{8,7}$;$^7I_9$;$^7F_6$;$^5G_6$). Several other states has been measured, but fall below the experimental detection limit. In Section 6.2, results of population partitions and state-specific kinetic energy (velocity) distributions are

presented. In Section **??**, a comparison is then made between CRDS measurements and some earlier models available in the literature.

6.2 Excited State Particle Measurements

The experimental setup used in this chapter is same as presented before, except that the studied species is Dysprosium, Dy. Note that present study is limited only to sputtering by normally incident Ar ions. Several absorption lines (electronic transitions) are probed in the spectral region of 390-405 nm. CRDS is an absorption technique so that in order to have a measurable signal the lower state of the transition being probed must be sufficiently populated. Absorption lines originating from the ground state (fine-structure) sub-levels and subsequent excited states and their sublevels are probed and the corresponding absorption lineshapes are measured. Equation 2.1 is used to determine the (path-integrated) number densities of the corresponding states from which population partitions are obtained. The mathematical framework presented in Chapter 3 is used to infer velocity distributions of the corresponding states.

6.2.1 Population Partitions

The absorption spectra from seven fine electronic structure levels that arise from two different electronic configurations, $4f^{10}6s^{2}5I_{8,7}$ and $4f^{9}5d6s^{2}7H_{8,7}or^{7}I_{9}or^{7}F_{6}or^{5}G_{6}$ are collected (see Fig. 6.3). Some levels are probed using several lines to reproduce the data. For example, the ground state population is measured by probing four different lines (see Fig.6.4): 399.805 nm (0-3.101 eV), 400.007 nm (0-3.10 eV), 401.496 nm (0-3.088 eV) and 404.712 nm (0-3.064 eV); and the population found from each line yields the same result within experimental error. Figure 6.4 lists all the measured transitions. All the data in the table is taken from either NIST [46] or Harvard [67]

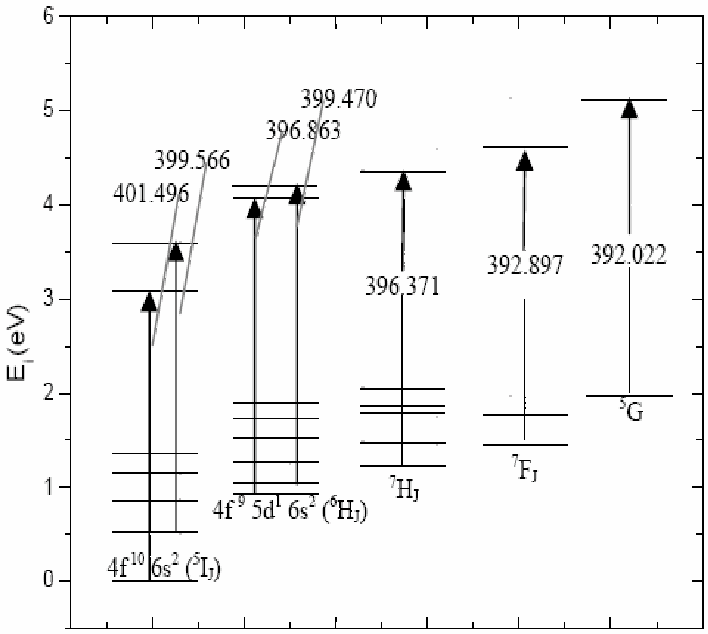

Figure 6.3: Partial energy level diagram of Dysprosium.

database. The partial energy level diagram of Dysprosium is shown in Figure 6.3 and the seven transitions, represented as arrows, can also be seen in figure 6.3. As an example, absorbance spectrum from the line at 397.499 nm due to the transition (lower state E_i=0.93 eV) is shown in Figure 6.5. The solid line is the best fit to the experimental data. Using Equation 2.1 and measuring the area under the absorbance spectrum, the absolute number density of the corresponding atomic state can be determined as presented in Chapter 2. Although absolute number density measurements are possible with CRDS, only the relative populations are of interest here.

The measured population partitions over the ground and excited states are shown in Figure 6.6. The populations (n_i) are normalized by the ground state and are plotted as a function of excitation energy above the ground state (and corrected for statistical weight). The ground state corresponds to $4f^{10}6s^2$ outer shell electronic configuration

Term	Configuration	λ_{vacuum} (nm)	A_{ji} (s^{-1})	E_i (eV)	J_i	E_j(eV)	J_k
$^5I_8$	$4f^{10}\ 6s^2$	399.8047	5.01E+05	0	8	3.101328	8
$^5I_8$	$4f^{10}\ 6s^2$	400.0068	2.95E+05	0	8	3.099762	8
$^5I_8$	$4f^{10}\ 6s^2$	401.4959	3.19E+06	0	8	3.088265	7
$^5I_8$	$4f^{10}\ 6s^2$	404.7115	1.66E+08	0	8	3.088265	7
$^5I_7$	$4f^{10}\ 6s^2$	399.5661	5.33E+06	0.512614	7	3.615794	7
$^7H_8$	$4f^9\ 5d^1\ 6s^2$	396.8631	4.35E+07	0.938078	8	4.062394	9
$^7H_8$	$4f^9\ 5d^1\ 6s^2$	397.4994	2.73E+07	0.938078	8	4.057392	7
$^7H_8$	$4f^9\ 5d^1\ 6s^2$	398.249	1.63E+07	0.938078	8	4.051521	8
$^7H_7$	$4f^9\ 5d^1\ 6s^2$	399.4696	3.68E+07	1.056317	7	4.160247	7
$^7H_7$	$4f^9\ 5d^1\ 6s^2$	400.6969	8.92E+07	1.056317	7	4.15074	7
$^7H_7$	$4f^9\ 5d^1\ 6s^2$	400.7197	7.84E+07	1.056317	7	4.150564	6
$^7H_5$	$4f^9\ 5d^1\ 6s^2$	397.2333	1.42E+08	1.52493	5	4.646334	5
$^7I_9$	$4f^9\ 5d^1\ 6s^2$	393.7809	1.07E+08	1.238803	9	4.387573	10
$^7I_9$	$4f^9\ 5d^1\ 6s^2$	396.3708	1.01E+08	1.238803	9	4.366999	9
$^7I_8$	$4f^9\ 5d^1\ 6s^2$	396.7473	6.64E+07	1.488791	8	4.614019	7
$^7F_6$	$4f^9\ 5d^1\ 6s^2$	392.897	2.83E+08	1.447426	6	4.60328	6
$^7F_5$	$4f^9\ 5d^1\ 6s^2$	396.4286	2.04E+08	1.754927	5	4.882667	4
$^7K_{10}$	$4f^9\ 5d^1\ 6s^2$	391.3651	7.95E+07	1.598606	10	4.766813	9
$^5G_6$	$4f^9\ 5d^1\ 6s^2$	392.0227	2.70E+08	1.966849	6	5.129742	7

Figure 6.4: List of all probed transitions to measure the population partitions.

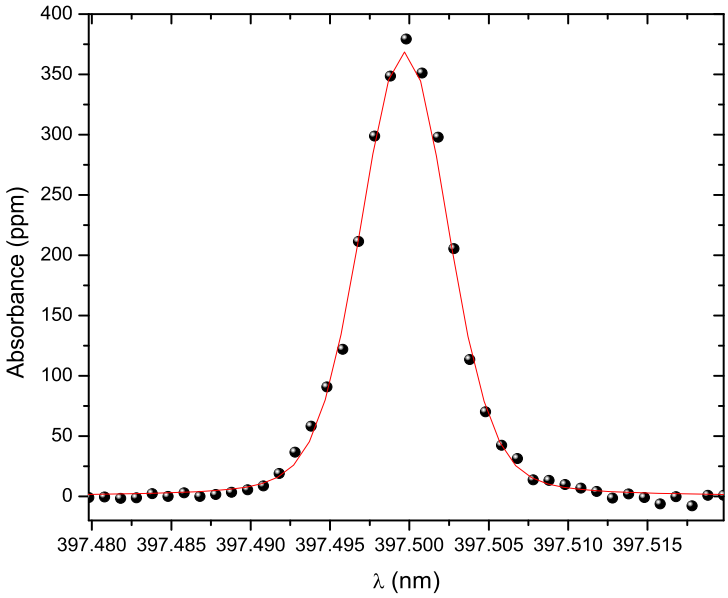

Figure 6.5: Sample absorbance spectrum collected with CRDS detection system at around 397.499 nm for probing the 0.938 eV level. Symbols: CRDS measurements. Solid line: fitted lienshape.

and the other excited states correspond to $4f^9 5d^1 6s^2$ outer shell electronic configuration. Note that when plotted in this way, a Boltzmann distribution would appear linear (e.g. as shown in Figure 6.1). Several observations may be made from Figure 6.6. First, one sees atomic states even with relatively high excitation energies are significantly populated. For example, E_i=0.938 eV has approximately 10 percent of the population of the ground state. Recent work has shown similar results for other species (see introduction to this chapter) [66] [36]. If one were to fit a characteristic Boltzmann temperature(T_B), a single T_B would not be sufficient to explain the measured population distribution. For example, the ground state ^5I_J populations, T_B is found to be 1425 $\pm$ 100 K; for the next excited state ^7H_J, T_B it is found to be 1000 $\pm$ 50 K. And,if one tries to fit T_B for the ground state and the excited state, it is found to be 4800 $\pm$ 150 K. As shown in Figure 6.6, higher excited states could not be measured because their populations are below the CRDS detection limit. Clearly, the observed population distributions do not follow Boltzmann statistics. However, within a single multiplet, the relative population decreases exponentially and can be governed by a characteristic Boltzmann temperature. Similar results based on LIF were reported where the population within the ground state sublevels is given by a Boltzmann distribution [24] [48] [27] [29] (see also discussion in Section 2.4. Also in Figure 6.6, one can see that the T_B for the sublevels is different for the ground state and the excited state.

The populations of the higher excited states may be explainable by the Resonant Electron Transfer (RET) model [60]. The RET model considers that when an energetic particle triggers a collision cascade, the sputtered particles set in motion from the surface as positive ions will neutralize by picking up an electron during ejection. Different neutralization schemes are possible but that with a single electron making an energy conserving transition from its valence band state in to a discrete atomic

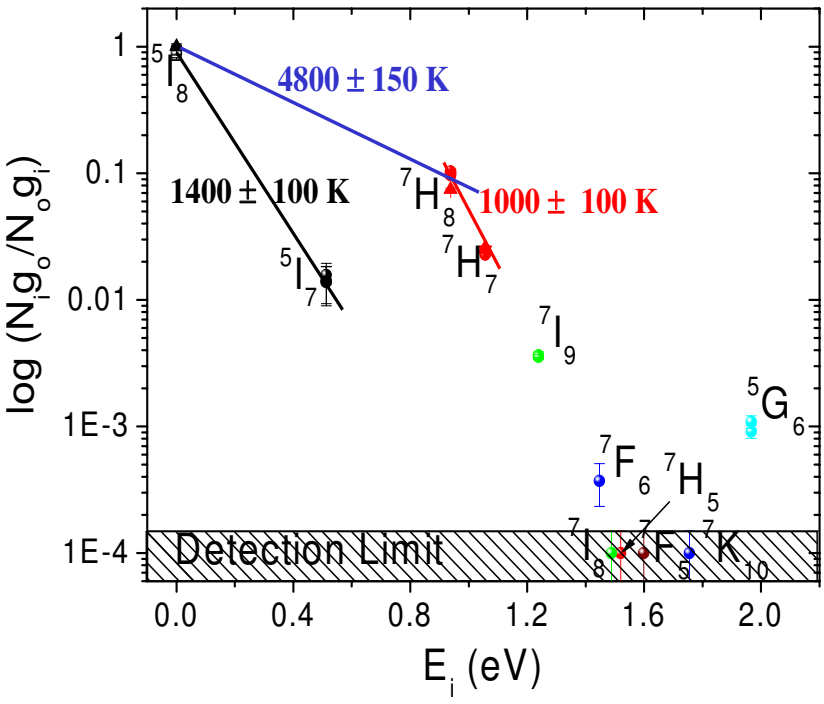

Figure 6.6: The relative population of different atomic states of Dy produced by 750 eV Ar^+ ion bombardment. The populations are given relative to the ground state population and corrected for statistical degeneracy of the states.

state, is by far the most probable process [62], [63], [64], [61],[65], [60]. The bulk work function of Dy is 2.89 eV and the ionization potential of Dy is 5.94 eV, so their excited states with excitation energies up to 3 eV lie below the Fermi level. Population partitions in Figure 6.6 agree with the energy window requirement of resonant electron transfer model. The population probability also depends on the position of the multiplets with respect to the Fermi energy level. The observed decrease in population with excitation energy for states within each low-lying multiplet indicates that the competition between the neutralization channels within one multiplet is governed by $E_F - E_a$ [68], where E_F is the Fermi energy and E_a is the activation energy. The population of 1.96 eV is higher than 1.44 eV and requires future investigation. The RET model explains the population partitions effectively as all the measured states meet the Fermi energy window requirement. According to the RET model, the neutralization probability is dependent on the coupling between atomic states and metal states, wave function overlap of both states and velocity of the escaping particle.

Also, a new line is measured that is not listed in any standard database. The transition is at 401.523 nm (0.938 eV - 4.026 eV) and an Einstein A coefficient value of 4.2×10^6 s^{-1} is obtained with an error of 10 %. The error is due to the uncertainty associated with the listing of Einstein A coefficient values of other associated transitions in the database and also due to experimental noise.

6.2.2 State Specific Velocity Distributions

Velocity measurements of Mo, Ti, Fe and Al were presented in Chapter 3. Here, the same approach is used to obtain velocity of sputtered Dy particles. Similar to Chapter 3, a unidirectional velocity distribution is first considered. Experimentally, a honeycomb-like structure (HCS) is used and the optical axis is oriented at 45° to the surface normal direction, so that the normally ejected particles have a non-zero

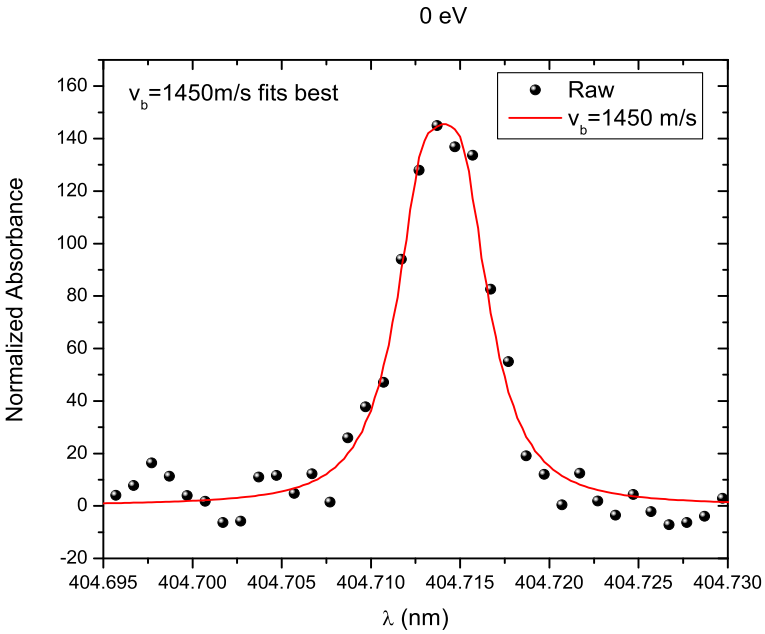

Figure 6.7: CRDS lineshape measured with honeycomb setup in which optical axis is at 45° to the unidirectional sputtered particles.

velocity component (Doppler shift) on the optical-axis (similar to Section 3.5). Figure 6.7 shows experimental data and the fit data. The data is fit using the formalism given in Chapter 3 and assuming a Thompson distribution (Eq.(6)) with V_b as a free (fit) parameter. The best fit is obtained for V_b=1450 $\pm$ 150 m/s.Uncertainty in the fit is primarily due to noise in the data. Notice that the splitting is not evident as the magnitude of the velocity is small and it smears the two peaks into one.

Owing to the reduction in signal level (factor of $\sim$ 20) due to the honeycomb setup, one can not use it to measure signals from the excited states. Therefore, most measurements were performed for the full velocity field. In this case, sputtered particles are ejected from the target in all directions, and the optical-axis is oriented perpendicular to the surface normal (parallel to the target). The Doppler lineshape is formed from a continuum of peaks associated with the different directions and

velocities of sputtered particles crossing the beam, and takes the form of a single broadened peak, similar but not the same as for a MB distribution (Chapter 3). Figure 6.8 shows CRDS spectra for several lines of sputtered Dy for a beam current of 30 mA and beam voltage of 750 eV. For $E_i = 0$ eV (top left of Fig. 6.8), the experimental data is again fit using V_b as a free parameter, and find the best fit for V_b=1450 $\pm$ 150 m/s . The agreement with the honeycomb measurement is further validation of the model.

Each of the lineshapes of Figure 6.8 can be reasonably fit assuming a Thompson distribution. Figure 6.9 shows that velocity distributions of atoms within the multiplet are consistent. [The velocity distributions of the ^5I_J multiplet (0 eV and 0.512 eV) are same and the velocity distributions of the ^7H_J multiplet (0.938 eV and 1.056 eV) are same (Figure 6.8)]. This finding is consistent with the past work [48] [27]. On the other hand, for different multiplets, the peak of the velocity distribution (and V_b) shifts to higher values as the energy increases. Past researchers have obtained similar results with different target materials [24].

According to the RET model, the neutralization probability is dependent on the coupling between atomic states and metal states, wave function overlap of both states and velocity of the escaping particle. If the velocity of the ejected particle is high then there is higher probability to end up in a $4f^9 5d^1$ state. The faster the ion moves away from the surface, the more dominant the electron transfer in to a $4f^9 5d^1$ state, due to much stronger coupling to the metal of these states with overlapping wavefunctions. For low velocities i.e. long interaction times, the influence of relative position of levels with respect to Fermi level become the dominant factor, reducing the influence of electronic configuration? The velocity distributions of atoms sputtered in states ^7H_J, $^7I_9$ and $^5G_6$, three of which are from the same electronic configuration, might be interpreted with RET process by comparing the characteristics of atomic levels with

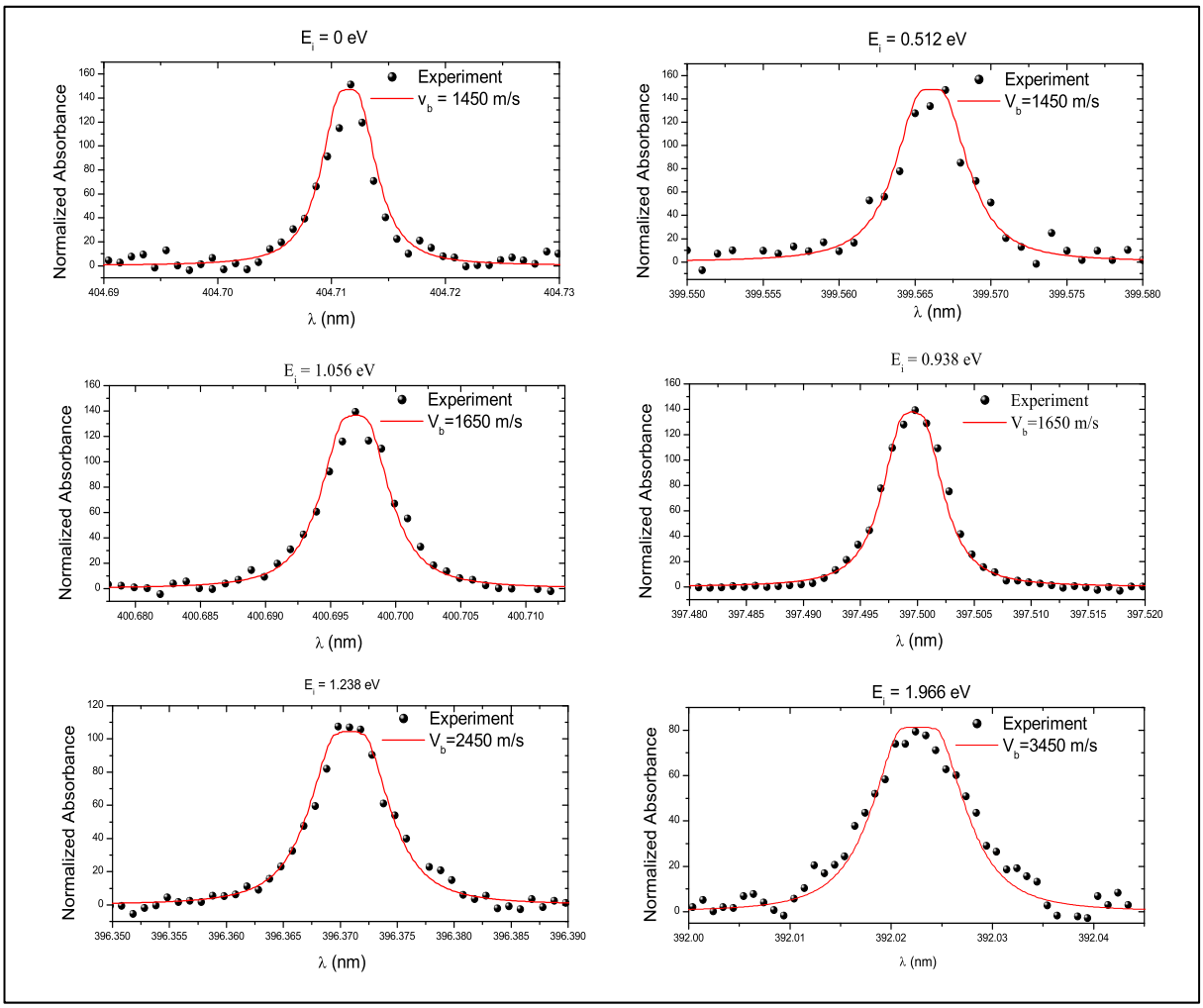

Figure 6.8: Velocity of atoms in different excited states inferred from analyzing their corresponding lineshapes obtained with out using honey comb filter.

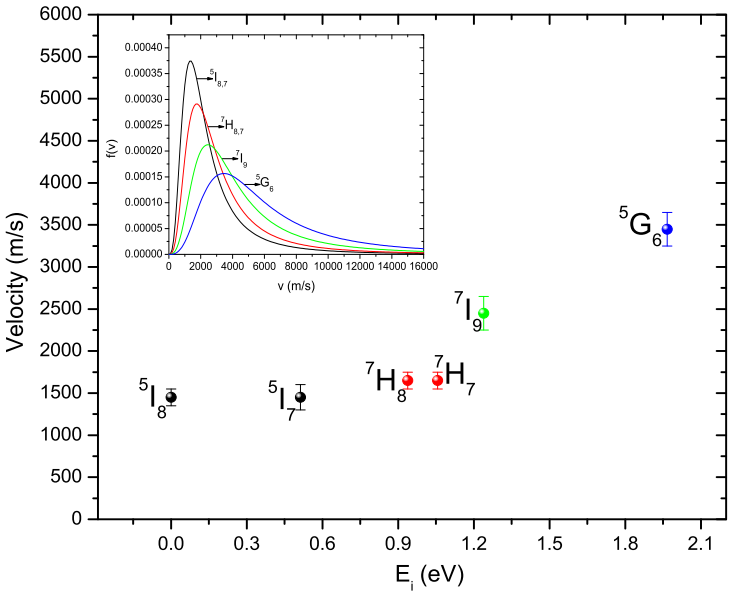

Figure 6.9: Velocity measurements of sputtered Dysprosium atoms in different atomic states. In the inset, one can clearly see that the peak of the velocity distribution is shifting to higher velocities.

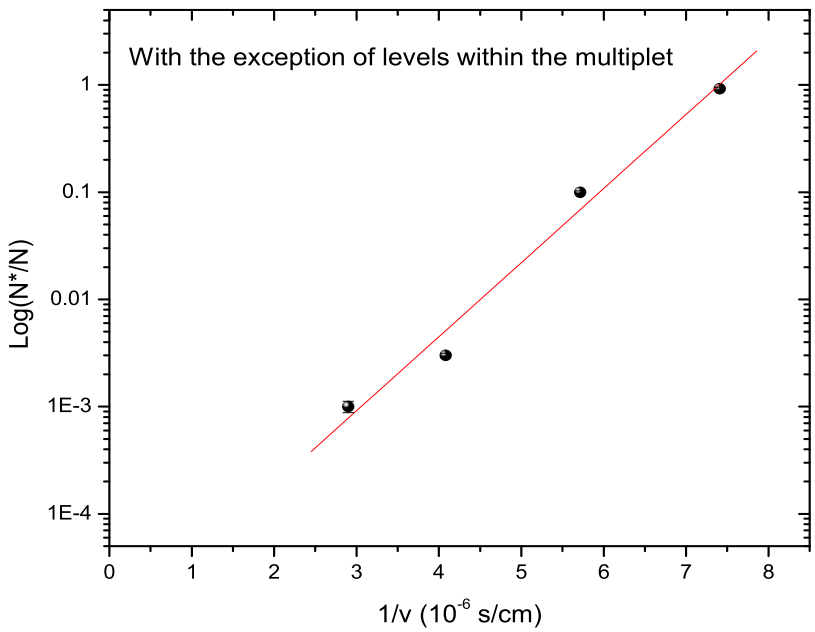

Figure 6.10: Hagstrum plot and linear dependence.

the bulk metal levels. Similar interpretation was done for Ir atoms that has complex electronic configuration by Bastiaansen et.al.[61].

State-specific variations in velocity distribution has been explained with a non-radiative deexcitation model which assumes that the rate of deexcitation depends exponentially on the inverse of the magnitude of velocity component perpendicular to the surface. Under the assumption, the velocity distributions should peak at higher values than those for the ground state distribution. Figure 6.10 shows the population fraction plot with $1/v$ dependence and it is linear if one excludes the states within the multiplet. Although this model does not explain behavior within a given multiplet it may explain the behavior of different multiplets.

6.3 Summary

In this chapter, the application of CRDS for quantitative measurement of population distributions of sputtered neutral atoms over excited states is reported. Population distributions of Dy were measured using CRDS. The Dy populations in the excited states are substantially populated and do not follow Boltzmann distribution. State selective velocity measurements were also obtained using CRDS. The velocity of the sputtered particles within the multiplet are same, yet one also finds that higher excited states are ejected with higher velocities. Although no dominant model was suggested for the observations, these results are first of its kind for Dysprosium. The sensitivity and state-specificity of CRDS will enable study of different elements and further understanding of excitation-deexcitation processes of sputtering particles, for example through the RET model.

Chapter 7

Conclusions and Future Work

7.1 Conclusions

CRDS has been demonstrated as a versatile tool for quantitative diagnostics of sputter erosion processes. Owing to its highly sensitive and highly quantifiable nature, CRDS has the potential to provide a powerful sputtering gauge that will strongly complement available diagnostic techniques. Its quantitative and linear nature (that does not require external calibration) provides a clear advantage over LIF for number density measurements. Further, the simple nature of CRDS (as compared to say surface layer activation) makes it very amenable to in situ applications, for example real time studies of device erosion rates, as a function of device operating conditions. Finally, the spectroscopic nature of CRDS makes it appropriate for species-specific studies of the sputtering of multi-component materials; for example, studying how the boron sputters from a boron nitride insulator and state-specific studies; for example, how the population partitions of the excited state particles are distributed.

7.1.1 Number Density Measurements

The quantitative detection of several sputtered metal species using CRDS has been presented in Chapter 2. CRDS, being an absorption based measurement tech-

nique, is well suited for absolute number density measurements. Briefly, number density is directly obtained from the area of the measured absorption spectrum. For each of the measured species, measurement validation was performed against a sputter model. Also, the excitation of sub-levels of the ground state multiplet for aluminum, iron, and titanium were studied. it was found that the overall species population can be found from the population of the ground state multiplet to within several percent. The detection limits of the CRDS measurement system were also presented that are found to be very adequate for electric propulsion studies.

7.1.2 Velocity Measurements

In Chapter 3, the CRDS velocity measurement approach was demonstrated for atoms of different species in a low-pressure (collisionless) environment. Velocity information was inferred from Doppler shift contributions to the measured absorption lineshape using a sputter model. Because, in CRDS, the laser beam propagates back-and-forth within the optical cavity, a measured absorption feature is split as it is both up- and down-shifted in frequency. The splitting of the absorption features allows direct velocity measurements without requiring an external frequency reference. Note that the hyperfine structure and isotopic splitting have not been incorporated into the existing model and should be considered in future work.

The CRDS technique was demonstrated for mono-directional particles as well as the more common condition where sputtered particles eject in all directions. Agreement with expected values was found in both the cases. Also, good agreement with LIF measurements was found which is considered as further validation of the CRDS measurement and the sputter model. With this ability added, CRDS can be used for computing the flux of sputtered particles, from which one can also determine sputter yields and erosion rates.

7.1.3 Differential Sputter Yield Measurements

In chapter 4, differential sputter yield measurements for normally incident ions using CRDS are presented. Differential sputter yield measurements are obtained from spatial profile (CRDS signal at a series of displacements relative to the target) and using an associated sputter model. The model was used to generate simulated spatial profiles each corresponding to a different differential sputtering profile (characterized with a single parameter, a). The best agreement between the simulated profiles and measured profile gives the differential sputter yield profile. The approach has been demonstrated for measurement of argon ions on molybdenum. Good agreement with QCM measurements was found, thereby validating the experimental measurement as well as the sputter model.

7.1.4 Sputtering Studies of Multi-Component Materials

The use of CRDS for species-specific measurements from multi-component materials was demonstrated in chapter 5. Sputter yields for many single-component materials are well known, however the sputter yields for multi-component materials are often not known. Also, owing to the relative complexity of these materials and the sputtering processes, it is generally difficult to numerically predict their sputtering properties. Target based techniques like weight loss or monitor-based techniques like the QCM are generally limited to single-component materials. Here, CRDS was used to obtain species specific total yields and differential sputter yields, with demonstrative measurements performed on Inconel by measuring individual sputtering of Fe, Cr and Mo. Also, the detection of Fe and Mn individually from a Fe-Mn target were presented.

7.1.5 Excited State Measurements

The application of cavity ring-down spectroscopy for the quantitative measurement of state-specific populations was presented in chapter 6. The spectroscopic nature of CRDS allows one to make state specific measurements. State specific populations and state-specific velocity measurements of Dysprosium were obtained and showed anomalous population distributions as well as elevated velocities for excited states. High sensitivity of CRDS and its general applicability may enable further understanding of excitation-deexcitation processes in the sputtering process.

7.2 Future Work

This dissertation lays the ground work for the use of CRDS as a diagnostic to measure sputter erosion. Further studies could include CRDS implementation on a real time thruster and CRDS with continuous-wave(CW) lasers for improved sensitivity. These areas are briefly described in the following sections.

7.2.1 Thruster Implementation

The lifetime of EP thrusters is largely governed by sputter erosion of guard-rings, grids, insulators, and other critical components. Lifetime determination generally requires deploying several complementary diagnostic techniques in concert with numerical modeling. The CRDS diagnostic may be used to directly measure (path-integrated) number densities of sputter products in the plume of the thruster. The CRDS measurements will provide direct information on the dependence of the erosion on sputter operating conditions, and will be used to validate computer erosion models. The approach is schematically illustrated in Fig. 7.1. Measurements will be performed as the thruster operating conditions (set points) are varied. These measurements will provide information on how thruster erosion (and lifetime) may vary with thruster operating conditions. The CRDS measurements will contribute to validation of the overall erosion modeling approach and thus will be beneficial towards

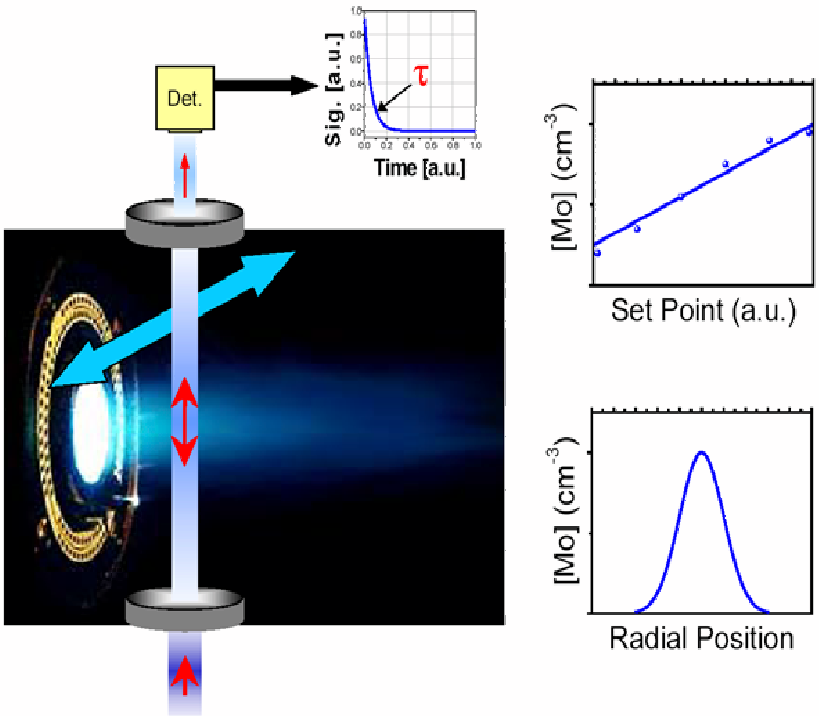

Figure 7.1: Approach to CRDS measurements in plume of a thruster. A CRDS cavity will surround the plume (actually with horizontal orientation), and measure Mo within the plume.

evaluation of all species of interest. The thruster will be moved on a translation stage in order to probe different chords and yield (via Abel inversion) radial profiles of Mo concentration within the plume.

7.2.2 Continuous-Wave CRDS

Another area of future work is to improve the sensitivity and detection limits of the CRDS technique. There are several applications where high sensitivity of the technique is required, for example to study sputtering by low energy ions at reduced sputter yields, or for rapid measurements for etch monitoring. A method to improve the sensitivity of the technique is to use continuous wave CRDS (cw-CRDS) instead of pulsed CRDS.

Details of the cw-CRDS can be obtained in reference [69] and references therein. Briefly, cw-CRDS uses a tunable diode laser and consists of the following features. The laser frequency is first slowly scanned across the absorption line of interest. One of the cavity mirrors is then moved back and forth to ensure periodic, occasional coincidences of the laser frequency with a cavity mode. Once such a resonance occurs and the cavity is filled, the laser beam entering the cavity if chopped or set off resonance, and the decay rate of the exiting is measured (similar to pulsed CRDS). Detection of species in parts per billion (ppb) can be easily achieved using cw-CRDS and its usage can therefore be extended to obtain sputtering measurements with high sensitivity.

Bibliography

[1] M. Tajmar, *Advanced Space Propulsion Systems.* New York: Springer-Wien, 2003.

[2] R. G. Jahn and E. Y. Choueiri, *Electric Propulsion in Encyclopedia of Physical Science and Technology*, 3rd ed. Academic Press, 2002, vol. 5.

[3] G. Saccoccia, J. Gonzalez, and D. Estublier, "Electric propulsion: A key technology for space missions in the new millennium." *Electric Propulsion Section, ESA Directorate for Technical and Operational Support*, 2000.

[4] I. Katz, J. R. Brophy, J. R. Anderson, J. E. Polk, and D. M. Goebel, "Technologies to improve ion propulsion system performance, life and efficiency for nep." *Advanced Space Propulsion Workshop*, 2003.

[5] O. B. Duchemin, *An Investigation of Ion Engine Erosion by Low Energy Sputtering.* California Institute of Technology: PhD thesis, 2001.

[6] V. S. Smentkowski, *Progress in Surface Science*, vol. 64, pp. 1–58, 2000.

[7] R. Behrisch, Ed., *Sputtering by Particle Bombardment I:Physical Sputtering of Single-Element Solids.* New York: Springer-Verlag, 1981.

[8] J.Mahan, *Physical Vapor Deposition of Thin Films.*

[9] M. R. Nakles, *Experimental and Modeling Studies of Low-Energy Ion Sputtering for Ion Thrusters.* Virginia Polytechnic Institute and State University: MS thesis, 2004.

[10] R. D. Kolasinski and J. Polk, "An overview of the results from an 8200 hour wear test of the nstar ion thruster." *39th AIAA Joint Propulsion Conference, Huntsville, AL*, pp. AIAA Paper 2003–5144, 2003.

[11] M. Pellin, R. Wright, and D. Gruen, "Laser fluorescence spectroscopy of sputtered zirconium atom." *Journal of Chemical Physics*, vol. 74, pp. 6448–6457, 1981.

[12] M. Pellin, C. Young, M. Mendelsohn, D. Gruen, R. Wright, and A. Dewald, "Oxygen and titanium sputtering yields as determined by laser fluorescence and auger electron spectroscopy for monolayer oxygen coverage of polycrstalline ti." *Journal of Nuclear materials*, vol. 111, pp. 738–743, 1982.

[13] H. Bay, J. Roth, and J. Bohdansky, "Light-ion sputtering yields for molybdenum and gold at low energies." *Journal of Applied Physics*, vol. 48, p. 47224728, 1977.

[14] J. Polk, W. von Jaskowsky, A. Kelly, and R. Jahn, "Measurement of mpd thruster erosion using surface layer activation," *Journal of Propulsion and Power*, vol. 3, pp. 33–38, 1987.

[15] M.S.Phillips, R.Loesing, G.M.Shedd, D.P.Griffis, and P.E.Russel, "Technologies to improve ion propulsion system performance, life and efficiency for nep." *Advanced Space Propulsion Workshop*, 2003.

[16] J. Blandino, D. Goodwin, and C. Garner, "Low energy sputter yields for diamond, carbon-carbon composite, and molybdenum subject to xenon ion bombardment." *Diamond and Related Materials*, vol. 9, p. 19922001, 2000.

[17] J. D. Williams, M. M. Gardner, M. Johnson, and P. J. Wilbur, "Xenon sputter yield measurements for ion thruster materials." *Twenty Eighth International Electric Propulsion Conference IEPC Paper*, 2003.

[18] A.P.Yalin, J.D.Williams, V.Surla, J.Wolf, and K. Zoerb, "Azimuthal differential sputter yields of molybdenum by low energy xe+ bombardment." *in 42nd AIAA Joint Propulsion Conference*, 2006.

[19] N. Andersen, B. Andresen, and E. Veje, "Atomic excitations in sputtering processes." *Radiation Effects*, vol. 60, pp. 119–127, 1982.

[20] R. P. Doerner, D. Whyte, and D. Goebel, "Sputtering yield measurements during low energy xenon plasma bombardment." *Journal of Applied Physics*, vol. 93, pp. 5816–5823, 2003.

[21] R. Stuart and G. Wehner, "Sputtering yields at very low bombarding ion energies." *Journal of Applied Physics*, vol. 33, pp. 2345–2352, 1962.

[22] P. Ray and V. Shutthanandan, "Low-energy sputtering research." *NASA/CR-1999-209161*, 1999.

[23] V.Shutthanandan, P.K.Ray, N.R.Shivaparan, R.J.Smith, and M.Mantenieks, "On the measurement of low-energy sputtering yield using rutherford backscattering spectrometry." *in 21st International Electric Propulsion Conference*, 1997.

[24] H. L. Bay, "Laser induced fluorescence as a technique for investigations of sputtering phenomena." *Nuclear Instruments and Methods B*, vol. 18, pp. 430–445, 1987.

[25] H. Bay, B. Schweer, P. Bogen, and E. Hintz, "Investigation of light-ion sputtering of titanium using laser-induced flourescence." *Journal of Nuclear Materials*, vol. 111, pp. 732–737, 1982.

[26] E. Hintz, D. Rusbldt, B. Schweer, J. Bohdansky, J. Roth, and A. Martinelli, "The determination of the flux density of sputtered atoms by means of pulsed dye laser excited fluorescence." *Journal of Nuclear Materials*, vol. 93, pp. 656–663, 1980.

[27] C. Young, W. Calaway, M. Pellin, and D.M.Gruen, "The determination of the flux density of sputtered atoms by means of pulsed dye laser excited fluorescence." *Journal of Vacuum Science and Technology A*, vol. 2, pp. 693–697, 1984.

[28] F. Orsitto, M. Borra, F. Coppotelli, G. Gatti, and E. Neri, "Moi density measurements by laser induced fluorescence spectroscopy." *Review of Scientific Instruments*, vol. 70, pp. 921–924, 1999.

[29] E. Dullni, "Laser fluorescence measurements of the flux density of titanium sputtered from an oxygen covered surface." *Applied Physics A*, vol. 38, pp. 131–138, 1985.

[30] R. Wright, M. Pellin, D. Gruen, and C. Young, "Laser fluorescence spectroscopy of sputtered uranium atoms." *Nuclear Instruments and Methods*, vol. 170, pp. 295–302, 1980.

[31] C. Gaeta, J. Matossian, R. Turely, J. Beattie, J. Williams, and W. Williamson, "Erosion rate diagnostics in ion thrusters using laser-induced fluorescence." *Journal of Propulsion and Power*, vol. 9, p. 369, 1993.

[32] A. Goehlich, N. Niemoller, and H. Dobele, "Anisotropy effects in physical sputtering investigated by laser-induced fluorescence spectroscopy." *Physical Review B*, vol. 62, p. 349, 2000.

[33] G. J. Williams and et al, "Laser induced fluorescence measurement of the ion velocity distributions in the plume of a hall thruster," *Thirty Fifth Joint Propulsion Conference, Huntsville Alabama*, 1999.

[34] G. Nicolussi, W. Husinsky, D. Gruber, and G. Betz, "Formation of metastable excited ti and ni atoms during sputtering." *Physical Review B*, vol. 51, pp. 8779–8788, 1995.

[35] A. Goehlich, "Investigation of time-of-flight and energy distributions of atoms and molecules sputtered from oxygen-covered metal surfaces by laser techniques." *Applied Physics A*, vol. 72, pp. 523–529, 2001.

[36] C. Staudt and A.Wucher, "Sputtering of ag atoms into metastable excited states." *Physical Review B*, vol. 66, pp. 1–12, 20002.

[37] V. Surla, *Sputter Erosion Measurements by Cavity Ring-Down Spectroscopy.* Colorado State University: MS thesis, 2004.

[38] K. Busch and M. Busch, *Cavity Ringdown Spectroscopy*, ser. ACS Symposium Series. U.K: Oxford University Press, 1999.

[39] G. Berden, R. Peeters, and G. Meijer, "Cavity ring-down spectroscopy: Experimental schemes and applications." *Int. Reviews in Physical Chemistry*, vol. 19, pp. 565–607, 2000.

[40] P. Zalicki and R. N. Zare, "Cavity ring-down spectroscopy for quantitative absorption measurements." *Journal of Chemical Physics*, vol. 102, pp. 2708–2717, 1995.

[41] A. P. Yalin and R. N. Zare, "Effect of laser lineshape on the quantitative analysis of cavity ring-down signals." *Laser Physics*, vol. 12, pp. 1065–1072, 2002.

[42] A. Schwabedissen, A. Brockhaus, A. Georg, and J. Engemann, "Determination of the gas-phase si atom density in radio frequency discharges by means of cavity ring-down spectroscopy." *Journal of Physics D: Applied Physics*, vol. 34, pp. 1116–1121, 2001.

[43] J. Booth, G. Cunge, L. Biennier, D. Romanini, and A. Kachanov, "Ultraviolet cavinty ring-down spectroscopy of free radicals in etching plasmas." *Chemical Physics Letters*, vol. 317, pp. 631–636, 2000.

[44] V. Surla, P. Wilbur, M. Johnson, J. Williams, and A. Yalin, "Sputter erosion measurements of titanium and molybdenum by cavity ring-down spectroscopy." *Review of Scientific Instruments*, vol. 75, pp. 3025–3030, 2004.

[45] W. R. Hudson and B. A. Banks, "An 8-cm electron bombardment thruster for auxiliary propulsion." *10th AIAA Electric Propulsion Conference.*

[46] "National institute of standards and techology atomic spectral database," 2003. [Online]. Available: http://physics.nist.gov/cgi-bin/AtData/main_asd

[47] Y. Yamamura and H. Tawara, "Energy dependence of ion-induced sputtering yields from monatomic solids at normal incidence." *Atomic Data and Nuclear Data Tables*, vol. 62, pp. 149–253, 1996.

[48] G. Betz and K. Wien, "Review: Energy and angular distributions of sputtered particle." *Intl. Jnl. of Mass Spectrometry and Ion Processes*, vol. 140, pp. 1–110, 1994.

[49] J. Ziegler and J. Biersack., "Srim 2003 (program and documentation)," 2003. [Online]. Available: http://www.srim.org/

[50] A.P.Yalin and V. Surla, "Velocity measurements by cavity ring-down spectroscopy." *Optics Letters*, vol. 30, pp. 3219–3221, 2005.

[51] G. J. Williams and et al, "Fmt-2 discharge cathode erosion rate measurements via laser induced fluorescence," *Thirty Sixth Joint Propulsion Conference, Huntsville Alabama*.

[52] A. Yalin, V. Surla, and a. J. W. M. Butweiller, "Detection of sputtered metals using cavity ring-down spectroscopy." *Applied Optics*, vol. 44, pp. 6496–6505, 2005.

[53] A. P. Yalin and V. Surla, "Determination of number density and velocity of sputtered particles by cavity ring-down spectroscopy." *in 29th International Electric Propulsion Conference*, 2005.

[54] E.Oyarzabal, J.H.Yu, J.Hanna, G.R.Tynan, R.P.Doerner, K.J.Taylor, and K.Schmid, "Molybdenum and carbon cluster angular sputtering distributions under low energy xenon ion bombardment." *in 41st AIAA Joint Propulsion Conference*, 2005.

[55] F. C. C and et al, "Next ion optics simulation via ffx," *Thirty Ninth Joint Propulsion Conference, Huntsville Alabama*, 2003.

[56] A.P.Yalin, J.D.Williams, V.Surla, and K. A. Zoerb, "Differential sputter yield profiles of molybdenum due to bombardment by low energy xenon ions at normal and oblique incidence." *Applied physics (to be published)*, 2007.

[57] Z.L.Zhang and L.Zhang, "Anisotropic angular distributions of sputtered atoms." *Radiation Effects and Defects in Solids*, vol. 159, pp. 301–307, 2004.

[58] R. Jr., "Theories of distribution of deposit from sputtered disk and rectangular electrodes." *I.B.M. Journal of Research and Development*, pp. 27–34, 1972.

[59] K.A.Zoerb, J.D.Williams, and a. A. D.D.Williams, "Differential sputtering yields of refractory metals by xenon, krypton, and ar ion bombardment at normal and oblique incidences." *in 29th International Electric Propulsion Conference*, 2005.

[60] E.Vandeweert, J.Bastiaansen, V.Philipsen, P.Lievens, and R.E.Silverans, "Resonant electron transfer during ion-beam sputtering of metals studied by double-resonant laser ionization." *Nucl. Inst. and Methods In Phys. Res. B*, vol. 164, pp. 795–802, 2000.

[61] J. Bastiaansen, V.Philipsen, P. Lievens, R. Silverans, and E. Vandeweert, "Influence of atomic structure on the quantum state of sputtered ir atoms." *Phys. Rev. A*, vol. 70, 2004.

[62] J.Bastiaansen, F.Vervaecke, E.Vandeweert, P.Lievens, and R.E.Silverans, "Electronic processes during the sputtering of atoms from metallic surfaces studied by resonance laser ionization spectroscopy." *Spectrochemica Acta Part B*, vol. 58, pp. 1147–1154, 2003.

[63] J. Bastiaansen, F. Vervaecke, E. Vandeweert, P.Lievens, and R.E.Silverans, "Modeling the multichannel electron transfer during the sputtering of co atoms." *Nucl. Inst. and Methods In Phys. Res. B*, vol. 203, pp. 158–163, 2003.

[64] J. Bastiaansen, V.Philipsen, F. Vervaecke, E.Vandeweert, P.Lievens, and R. Silverans, "Velocity depependent electron transfer during emission of ion-beam sputtered cu atoms." *Physical Review B*, vol. 68, 2003.

[65] E.Vandeweert, P.Lievens, V.Philipsen, J.Bastiaansen, and R.E.Silverans, "Measurements of population partitions and state-selected flight -time distributions of kev ion-beam-sputtered metastable atoms." *Physical Review B*, vol. 64, 2001.

[66] C.He, Z. Postawa, S.W.Rosencrance, R.Chattterjee, B.J.Garrison, and N.Winograd, "Band structure effects in ejection of ni atoms in fine structure states." *Physical Review Letters*, vol. 75, p. 3950, 1995.

[67] [Online]. Available: http://cfa-www.harvard.edu/amdata/ampdata/kurucz23/sekur.html

[68] P.Lievens, V.Philipsen, E. Vandeweert, and R.E.Silverans, "Emission of ground and metastable state ni and co atoms during ion-beam sputtering:quantitative measurements of population and kinetic energy distributions." *Nucl. Inst. and Methods In Phys. Res. B*, vol. 135, pp. 471–476, 1998.

[69] D. Romanini, A. A. Kachanov, N. Sadeghi, and F. Stoeckel, "Cw cavity ring down spectroscopy." *Chem. Phys. Lett.*, vol. 264, p. 316322, 1997.

[70] J. Biersack and W. Eckstein, "Sputtering studies with monte carlo program trim.sp." *Journal of Applied Physics A*, vol. 34, p. 7394, 1984.

[71] C. W. et al, "Sputtering of polycrystalline metals by inert gas ions of low-energy (100-1000 ev)." *Physica*, vol. 27, pp. 763–764, 1961.

Appendix A

Current Density Measurements of the Ar Ion Beam

Here details of the current density measurements are presented here. A Multi Axis Plasma Profiler System (MAPPS) [55] system was built at Colorado State University that is capable of positioning a Faraday probe throughout the three-dimensional volume of ion and plasma plumes for the purpose of making current density measurements. A photograph of the MAPPS apparatus is shown in Fig. A.1 along with an exploded solid model showing the main components of the system. Figure A.2 shows an image of how the system was mounted in a cylindrical vacuum chamber. Much of the mechanical design of the MAPPS was based upon the geometry of the cylindrical vacuum chamber. As shown in Fig. A.2, the ion source is mounted on the top flange of the vacuum tank and pointed down toward the bottom of the chamber. Because of the chamber geometry, the MAPPS system was designed to mount in the bottom of the chamber with the measurement probe pointed up toward the ion source. An orificed Faraday probe was used to make current density measurements because of its compact size and relative ease of use.

In order to position the Faraday probe within the three dimensional r-θ-z (or x-y-z) space, three high-resolution stepper motors are used. More details about the

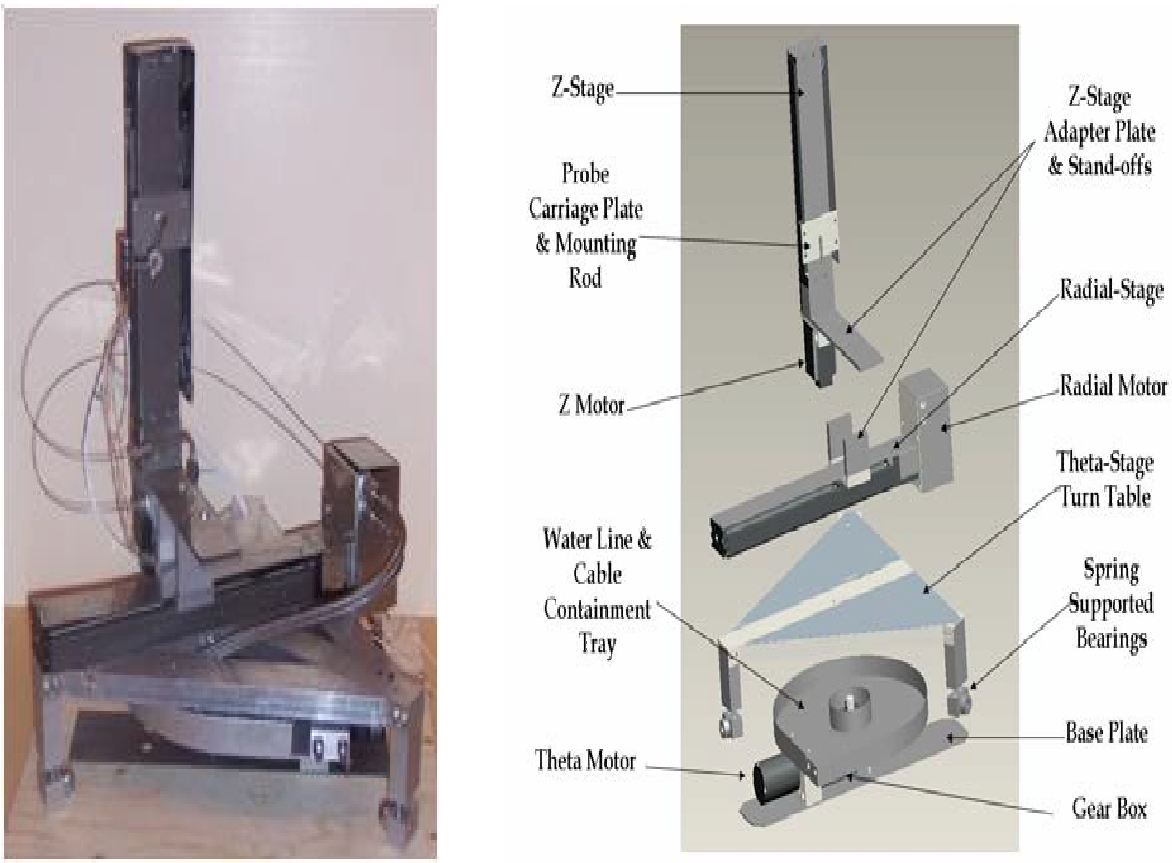

Figure A.1: Mechanical design of the system. Three stepper motors are used to position a Faraday probe in a three dimensional space.

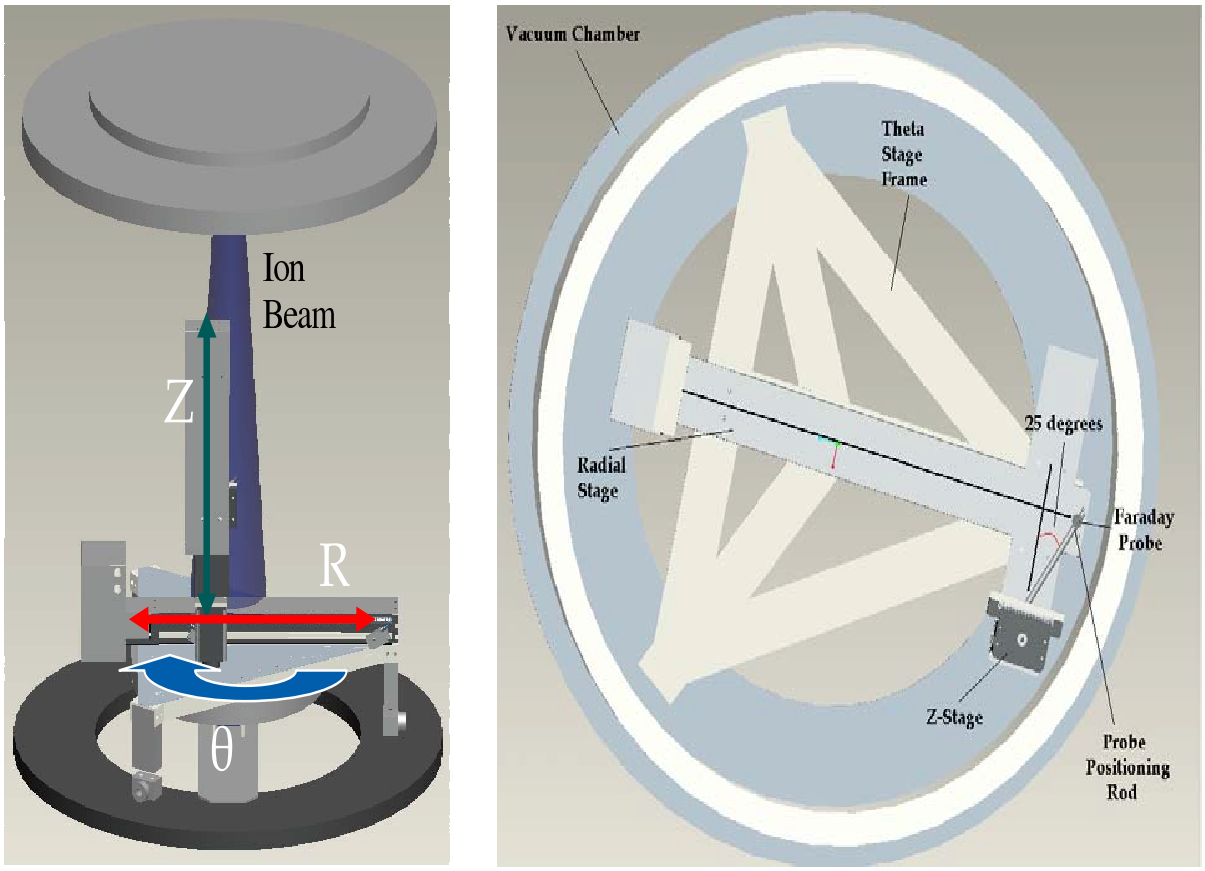

Figure A.2: Layout of the system within the vacuum tank. The ion source is mounted on the top flange and pointed down. Using a combination of radial, theta, and axial moves, a Faraday probe is used to map the current density of ion and plasma sources in three dimensions.

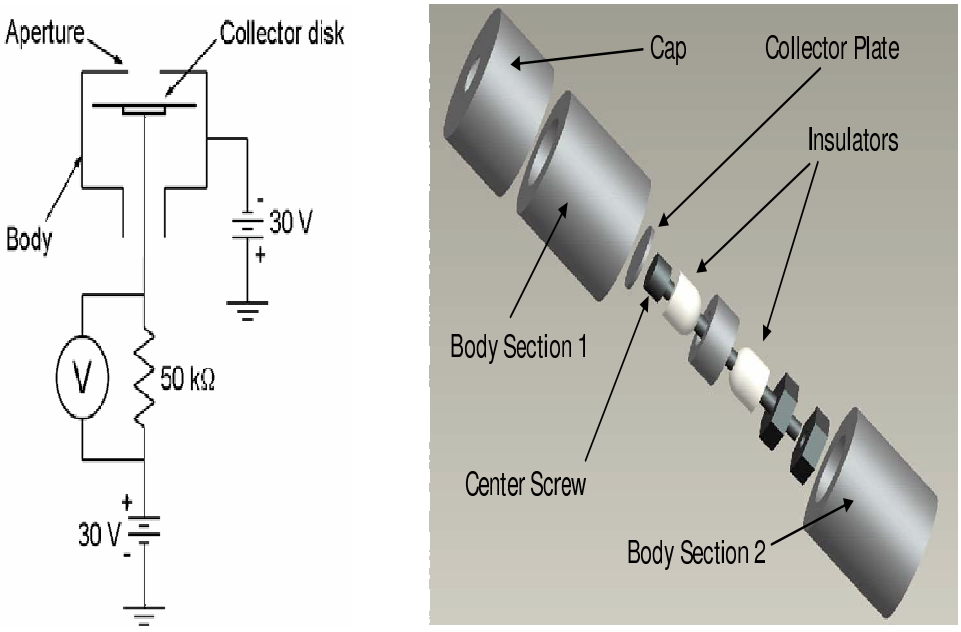

Figure A.3: Electrical schematic and model of the Faraday probe used to measure the ion current.

motors are given in [55]. Figure A.2 also shows an image of the system viewed from the top as seen by the ion source.

A Faraday probe, shown in Fig. A.3, is used to measure the ion beam current density at a given location within the ion beam. Ions from the beam enter the probe through the body aperture and strike the collector disk. The current is measured by reading the voltage across a resistor that is placed in the electrical lead between the collector disk and ground. The current density is then calculated using [55]:

$$j_B = \frac{V.1000}{R.A_{aperture}} (\mathtt{mA/cm^2}) \tag{A.1}$$

Where V is the voltage across the resistor (Volts), R is the value of the resistor (Ohms) and $A_{aperture}$ is the area of the opening (cm^2). The aperture sets a specific collection area since the collector disk is made to be larger than the aperture opening. The collector plate is biased positive (30 V) of ground in order to repel any low energy charge exchange ions that exist within the vacuum tank. The probe cap

and body are biased negative (-30V) to repel beam plasma electrons from reaching the collector plate. In addition, the combination of the negative bias on the body and the positive bias on the collector disk serves to eliminate secondary (or Auger) electron emission from the collector. In this bias scheme, all secondary electrons that are generated from ions striking the collector disk will return back to the collector due to the adverse potential gradient created between the body and the collector disk. The cooling, electrical, and user interface setup of MAPPS are presented in detail elsewhere [55]. The computer program communicates movement commands to the Trio motor controller and requests current density measurements from an HP multimeter. Figure A.4 shows screen shot of the experimentally measured J_{xyz} using data acquisition software(Labview).

The ion source was used in two configurations. One configuration is to use the full extent of 8 cm diameter grids to extract the ion beam. This configuration was used to make the differential sputter yield measurements. The other configuration is such that the grids are masked and the extent of the resulting ion beam is a rectangular section of 8 cm $\times$ 2.5 cm. This configuration was used initially to make number density measurements and velocity measurements. MAPPS was used to make current density measurements for both the configurations.

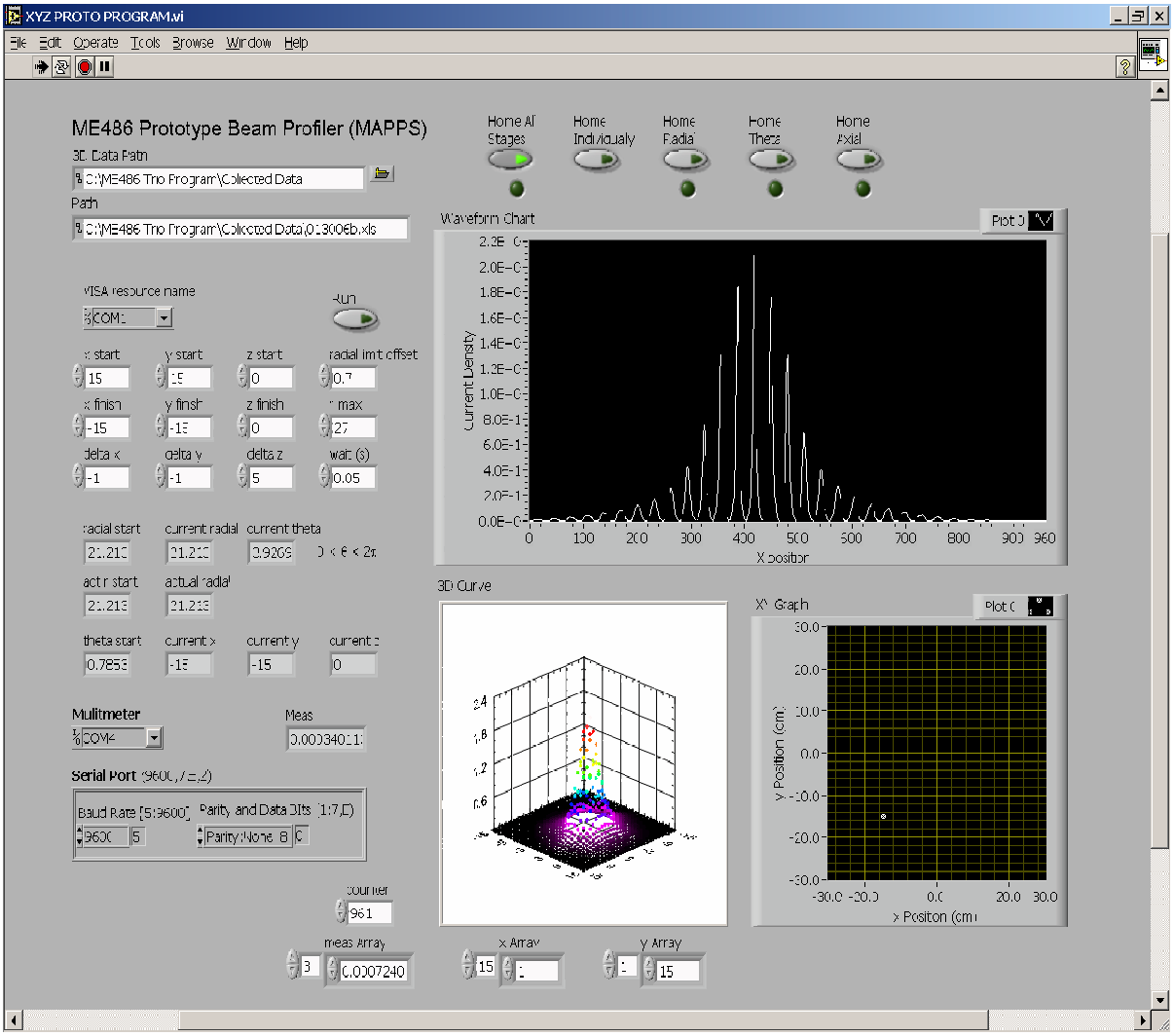

Figure A.4: Screen shot of the experimentally measured J_{xyz} using data acquisition software(Labview).

Appendix B

TRIM(the Transport of Ions in Matter)

TRIM (The TRansport of Ions in Matter) 2003 is part of the SRIM 2003 (Stopping and Range of Ions in Matter) software package created by J.F. Ziegler and J.P. Biersack [49]. SRIM 2003 is group of programs that calculate the stopping range of ions in matter through quantum mechanical treatment of ion-atom collisions [49]. TRIM simulates ion bombardment with user defined target and ion properties. The user sets the target and ion elements, incidence energy, incidence angle, and the number of incoming ions. TRIM uses Monte-Carlo calculations to make detailed calculations of the energy transferred to every target atom collision [49]. Incident ions and recoils are tracked through their slowing down process until their energy falls below a predetermined energy or they are so far from the surface that they are no longer candidates for sputtering [70]. Calculations are made efficient from the use of statistical algorithms that allow the ion to make jumps between calculated collisions and then averaging the collision results over the intervening gap [49].

TRIM also accepts complex targets made of compound materials with up to eight layers, each of different materials. It calculates both the final three dimensional distribution of the ions and also all kinetic phenomena associated with the ion's energy loss: target damage, sputtering, ionization, and phonon production. Thus, TRIM

simulations allow determination of sputtering data that would be difficult and time consuming to collect experimentally. More details on TRIM can be found in reference [49].A user can analyze many aspects of sputtering behavior with TRIM. In this study the main points of interest were the sputtering yield, and energy distribution of the sputtered atoms.

TRIM uses three key calculation parameters for the target material. These are the lattice displacement energy, surface binding energy, and lattice binding energy. The sputtering yield is most sensitive to the surface binding energy. Running TRIM with the default values resulted in significantly lower sputtering yields than reported in experimental tests [5]. In the literature TRIM was calibrated by adjusting the input parameters in such a way that the TRIM sputtering yields matched experimental results, e.g [5]. The procedure was to adjust the surface binding energy until the TRIM sputtering yield matched the mean of the experimental sputtering yields from references [5], [71], [16], [22], while the other two parameters were left as the default values. However, the angular distribution of the sputtered atoms from TRIM still showed large discrepancies with the experimental data from reference [23]. Attempts to match the input parameters to change the angular distribution of sputtered atoms were unsuccessful.

Similar to the reported references, the current work is also based on changing the default value of the surface binding energy. However, instead of matching the sputter yields, the current work uses the experimentally measured values of surface binding energies. In this way, good agreement is obtained between experimental sputter yields and TRIM predicted sputter yields as presented in Section 5.2.4.